MAURICIO FELIPE REVELO ARISTIZABAL

ANALYSIS OF ATMOSPHERE-PLANT-SOIL INTERACTIONS

Analysis of Atmosphere-Plant-Soil interactions

A thesis submitted as a partial requirement for the degree of Master in Earth Sciences

Advisor: Daniel Felipe Ruiz Restrepo

School of Applied Sciences and Engineering, Universidad EAFIT

Contents

List of Figures

List of Tables

Dedicated to my family

Acknowledgments

I am deeply grateful to my family and especially Alejandro and Aurora, for their unwavering support and love.

To my friends Lady, Mafe, May, and Cami, thank you for your encouragement, care, and steady presence.

I am truly grateful to my advisor, Daniel, for his steadfast guidance and wisdom, which have been invaluable throughout this journey.

I also appreciate the backing of the Applied Mechanics team, and the collaboration and advices of my Siatos, especially Juliana and Federico.

Finally, I thank Universidad EAFIT for the opportunity to pursue my passion for research.

Thesis layout

Understanding the interactions between the atmosphere, plants, and soil is crucial for addressing soil stability, water transfer, and temperature variations, especially under changing climatic conditions. These interactions influence hydrological and mechanical soil processes, with implications for geotechnical engineering, agriculture, and environmental sustainability.

Vegetation plays a crucial role in altering the soil water balance by influencing infiltration, reducing runoff, and providing mechanical reinforcement through root systems. This study examines coupled Soil-Atmosphere dynamics, focusing on the role of vegetation within this continuum, analyzing geotechnical time series from in-situ sensor monitoring, and visualizing root zones to enhance understanding and address gaps in soil-atmosphere interaction research.

The thesis is organized in three chapters and 3 appendices (see Figure 1). The contents for each one are described as follows:

Chapter 1 Reviews the Soil-Atmosphere system and the governing equations in a Thermo-Hydro-Mechanical framework, emphasizing the role of vegetation. It explores how root geometry influences soil stability and hydrological processes. Several studies are synthesized. Alongside, explores the role of geotechnical monitoring in all the studies reviewed, focusing on coupled processes.

Chapter 2 Presents a methodology for visualizing root system architecture using digital image processing, to calculate root geometric parameters for multiple purposes described in chapter 1. It contributes to nature-based solutions that enhance soil stability and sustainability under climate change.

Chapter 3 This chapter analyzes time-series data derived from geotechnical monitoring, useful to identify key coupled interactions within the Soil-Atmosphere system. Although the plant component is relevant in the two preceding chapters, it is not applicable here due to the lack of vegetation data. Instead, this section focuses on exploring complementary monitoring tools through a data-driven approach. Using spectral techniques such as Wavelet and Hilbert-Huang, the dominant frequencies influencing soil moisture, temperature, displacement and related variables were unwrapped. The analysis begins with data preprocessing to address typical issues like missing values and noise, followed by extracting time and frequency dependent information.

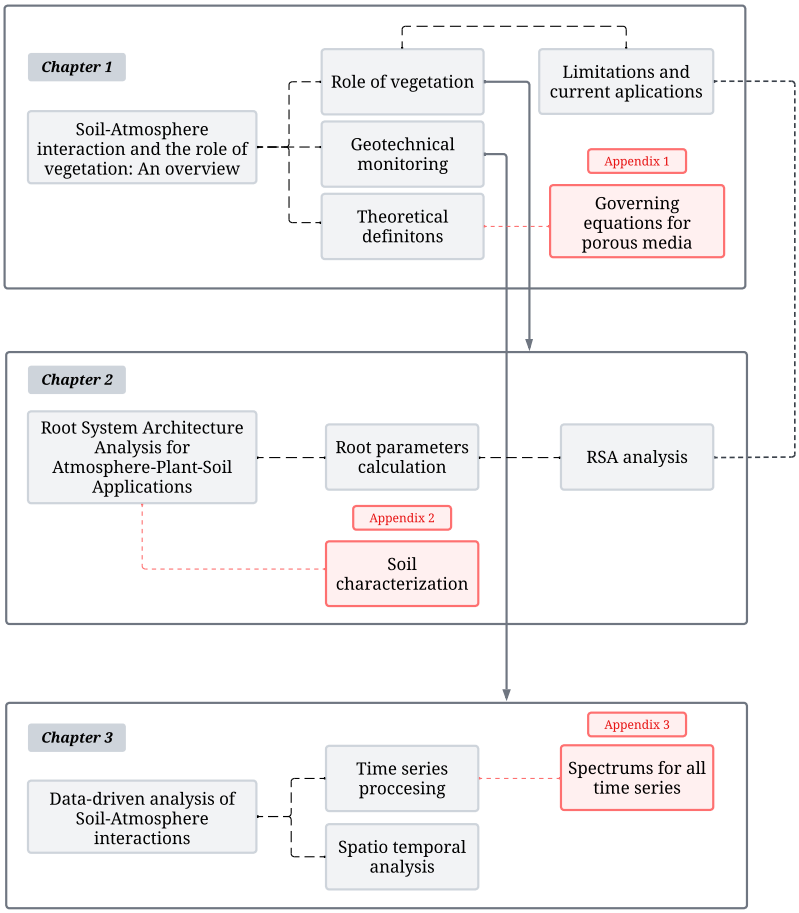

Figure 1: Thesis layout.

These tools were helpful to reveal seasonal cycles under varying conditions. Coherence and correlation analysis further explore coupled relationships (e.g., rainfall, soil moisture) across different spatio-temporal scales.

Appendix 1 contains all the theoretical information about thermo-hydro-mechanical governing equations and mathematical foundations for porous media. Appendix 2, contains soil characterization where some plant samples growth at a plot of land under meteorological conditions. Finally, Appendix 3 contains supplementary graphics for all the time series, including Global Wavelet and Hilbert Huang spectrums.

Objectives

General objective

Analyze the interactions between the Atmosphere-Plant-Soil continuum by assessing their spatiotemporal variability and developing tools to facilitate their study.

Specific objectives

- Summarize the role of vegetation in soil-atmosphere continuum.
- Examine Soil-Atmosphere time series data trough coupled study cases for better understanding of spatiotemporal behavior of flux-phenomena.
- Develop an easy-use workflow for root architecture visualization.

Soil-Atmosphere interaction and the role of vegetation: An overview

Abstract

Advances in Soil-Atmosphere interaction have revealed the complex dynamics driving slope stability, erosion, and water-heat distribution through coupled processes such as infiltration, heat transport, evapotranspiration and root water uptake. Research highlights the critical role of the unsaturated zone in controlling mass and energy fluxes under changing conditions, especially when accounting for the influence of vegetation as an additional dimension that increases system complexity. In this context, approaches have evolved to increasingly incorporate vegetation effects, together with improved modeling and monitoring strategies, to better understand geotechnical problems influenced by variables such as moisture content, suction, temperature, rainfall and shear strength,

Contemporary strategies now integrate theoretical, experimental, and numerical approaches to investigate even plant-soil hydraulic interactions within the root zone, addressing factors such as root system architecture, plant spacing, and climate variability. Despite the stabilizing role of roots, empirical models often struggle to accurately capture the dynamic interactions between roots and soil, as root architecture and hydraulic behavior vary under changing environmental conditions.

Accounting for spatial and temporal variations in root behavior and climatic factors within the Soil-Plant-Atmosphere Continuum provides valuable insights into the study of slope stability, wildfires, and other related processes. This underscores the need for adaptable tools that capture the influence of vegetation and seasonal patterns on unsaturated zone behavior. This research presents a state-of-the-art review of coupled frameworks in geotechnics, highlighting the role of vegetation across various studies, including analytical, numerical, and monitoring-modeling tools and case examples.

Introduction

The atmosphere is the mechanism that carries out most of the processes affecting the earth surface, involving flux exchange phenomena among the terrain and the surrounding environment. The behavior and properties of the unsaturated zone are largely dependent on these transfer processes (Blight, 2013). Soil-Atmosphere (SA) interactions may trigger rapid, catastrophic events classified as destructive or evolve slowly and subtly, still causing significant long-term damage and costs, categorized as conservative (Blight, 2013).

This exchange depends on several climatic mechanisms such as infiltration, evaporation or evapotranspiration and water uptake by plant roots (Hemmati et al., 2012; Samat, 2016; Guachizaca, 2018). The study of atmospheric and subsurface variables and their interaction, plays a key role in understatement of multiple phenomena such as wildfires, behavior of expansive soil, geothermal energy, effects of climate change on slope stability, landslides and soil erosion (An et al., 2018; Oorthuis et al., 2020).

There are several strategies for studying and understanding the effects of the SA interaction on a coupled frame: theoretical, experimental and numerical. These strategies vary in complexity with the most advanced considering vegetation influence (Elia et al., 2017), however, to incorporate this variable adds an extra layer of complexity (Tang et al., 2018).

Vegetation should be considered because it influences both the water balance and the mechanical properties of the soil, through evapotranspiration processes occurring in the shallow layers, leading to negative water fluxes. Leaves and canopy protect the slope by intercepting rainfall, reducing infiltration, and limiting surface erosion, while roots provide mechanical reinforcement to the soil (Elia et al., 2017; Wang et al., 2020), where the term Root System Architecture (RSA) defined as the shape and spatial arrangement of a root system within the soil, takes relevance (Rogers and Benfey, 2015).

Ng et al. (2019) and Fraccica et al. (2022) have made significant progress in quantifying the effect of roots in the hydrological balance and the tensile strength. However, the quantification of RSA and its effect on soil is an avenue to be explored, particularly in numerical modeling applications. Authors such as Tarantino and Roberts-Self (2023) discusses traditional models and proposes a more detailed approach that considers the interactions within the Soil-Plant-Atmosphere Continuum. This aims to improve predictions of plant water uptake in water-limited conditions where non physically-model based solution are available.

Initially, this chapter presents a brief section of the Thermo-Hydro-Mechanical framework, outlining the mathematical basis for the relationships that describe how materials behave and interact considering the multiphase nature of porous media.

Moreover, the chapter presents key formulations for Plant-Soil interactions. It highlights the dual role of plants in both hydrological and mechanical pro-

cesses and the importance of root geometry as a key factor in controlling water movement and stabilizing the soil. The final part consist of monitoring study cases and common strategies in geotechnical problems for coupled SA phenomena analysis.

Porous Media Formulations

Coupled processes in soils and rocks follow fundamental physical laws of mass and energy conservation and stress equilibrium (Ruiz, 2013). A porous medium generally comprises three phases: solid, liquid, and gas, and three species: mineral, water, and air (Gens and Olivella, 2001). The compositional approach is used to formulate mass balance equations, avoiding explicit phase change terms, which is particularly advantageous under equilibrium conditions (Sánchez, 2004).

To address this interplay, a multi-phase-species approach is adopted, expressing these phenomena through three key components: balance equations, which ensure conservation of mass, energy, and momentum; constitutive equations, which describe material behavior and transport processes; and equilibrium restrictions, which define thermodynamic relationships between phases. Table 1 summarizes these governing equations and also the main variables proposed originally by Olivella et al. (1994), and the Figure 2 presents a general scheme for Thermo-Hydro-Mechanical couplings in geological media.

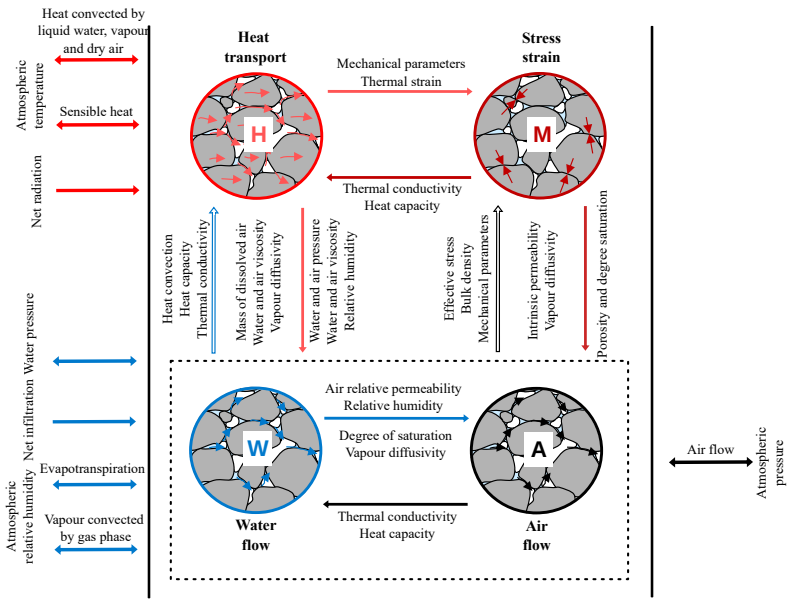

Figure 2: Overall THM couplings in soil and rock media. Adapted from Ruiz (2013).

Some representative numerical codes have been developed to simulate the flux exchange within the system, enable the modeling of coupled processes using the governing equations presented previously in Table 1. e.g., θ-STOCK, Vadose/W code, Plaxis 2D, and Code_Bright (Badakhshan et al., 2024). For more detailed and mathematical information, refer to Appendix 1.

Governing Equations*	**Variable**	**Notation**
Balance Equations		
Balance of solid mass	Porosity	ϕ
Balance of water mass	Liquid pressure	P_l
Balance of air mass	Gas pressure	P_g
Balance of energy	Temperature	T
Balance of momentum	Displacements	u
Constitutive Equations		
Law of Fick	Non-advective flow of vapor and air	i_w^g, i_a^l
Law of Darcy	Advective flow of liquid and gas	q_l, q_g
Law of Fourier	Conductive heat flow	i_c
Mechanical constitutive model	Stress tensor	σ
Liquid density	Density of liquid phase	ρ_l
Gas law	Density of gas phase	ρ_g
Retention curve	Degree of saturation in liquid and gas phases	S_l, S_g
Equilibrium Restrictions		
Law of Henry	Mass fraction of air in liquid	ω_a^l
Psychometric Law	Mass fraction of water vapor in gas	ω_w^g
Constraints		
Mass balance constraint	Sum of vapor and air mass fractions	$\omega_w^g + \omega_a^l = 1$
Saturation constraint	Sum of liquid and gas saturations	$S_l + S_g = 1$
Momentum balance constraint	Gradient of displacements	∇u

Table 1: Governing Equations and Associated Variables.

Hence, the behavior and properties of the unsaturated zone are largely dependent on the coupled transfer processes between the atmosphere and the terrain (Blight, 1997), closely linked, for example, to the water balance which determines things like water table depth, average and seasonal water content profile and seasonal swelling or shrinking (Blight, 2013). Some of these interactions can manifest suddenly and with devastating consequences, potentially leading to the collapse of critical infrastructure such as dams and bridges, resulting in loss of human life and extensive environmental damage (Blight, 2013). Other interactions may progress slowly and subtly, yet remain destructive and costly over time, such as the impact of swelling or shrinking clays on structures with shallow foundations (Blight, 2013).

Soil-Atmosphere Interaction

Atmospheric conditions are influenced by processes such as radiation and heat exchange, moisture dynamics (including clouds and precipitation), air mass movement, and interactions with surface components, such as water bodies, vegetation, and exposed soils and rocks (Badakhshan et al., 2024). The Figure 3 presents a schematic overview of these interactions.The following sections detail the formulation used for a porous medium in Code_Bright. The mathematical definitions provided for mass, energy, and vegetation are derived from Badakhshan et al. (2024) and Guachizaca (2018).

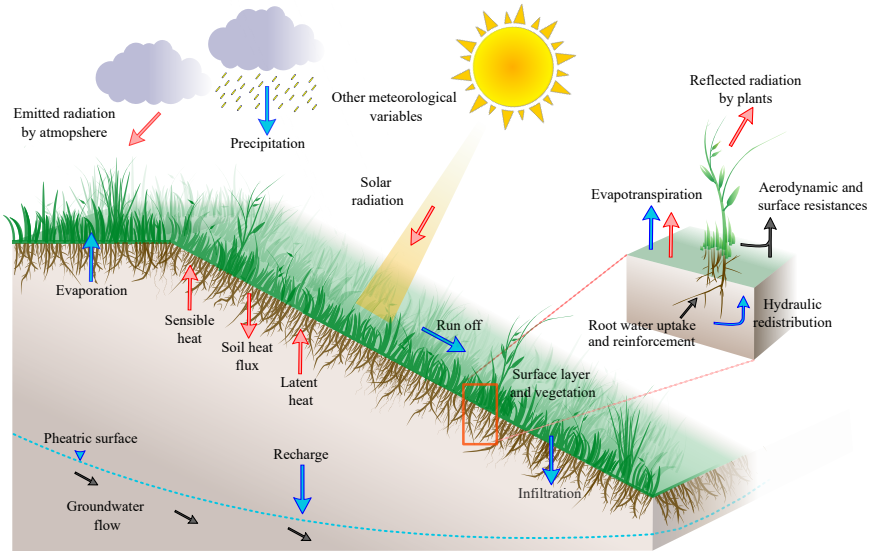

Figure 3: Schematic representation of energy and mass fluxes at the Atmosphere-Plant-Soil interface.

Mass Balance

The water flux infiltrating the soil is expressed as the sum of precipitation (P), evaporation (E), advective vapor flux through the gas phase (j_g^w), and surface runoff (j_{sr}) as,

$$j_a^w = k_{\text{rain}} P + E + j_g^w + j_{sr} \tag{1}$$

where k_{rain} denotes the rainfall interception coefficient, which generally varies from 10% to 30% for grass species, as stated by Hemmati et al. (2012). The evaporation flux (E) is modeled using an aerodynamic diffusion approach, as outlined by Sellers et al. (1986), and is given by,

$$E = \frac{k^2 v_a \phi}{\left(\ln \frac{z_a}{z_0}\right)^2} (\rho_{va} - \rho_v) \tag{2}$$

where ρ_{va} and ρ_v represent the absolute humidity in the atmosphere and at the boundary condition nodes, respectively. The equation also includes the von Karman constant (k), the stability factor (ϕ), the wind speed (v_a), the roughness length (z_0), and the screen height (z_a), where v_a and ρ_{va} are measured.

The j_{sr} flux, representing water flow over the surface that does not infiltrate the ground but instead drains, is defined as,

$$j_{sr} = \begin{cases} \gamma_l (P_l - P_{ga}) & \text{if } P_l > P_{ga} \\ 0 & \text{if } P_l \leq P_{ga} \end{cases} \tag{3}$$

where γ_l denotes the leakage coefficient, and P_{ga} represents atmospheric pressure. This method calculates runoff but does not include overland flow within the simulation.

The j_g^w flux is determined using the gas flux and the mass fraction of vapor, expressed as,

$$j_g^w = \begin{cases} \omega_g^w q_g & \text{if } P_g > P_{ga} \\ \frac{\rho_{va}}{\rho_{ga}} q_g & \text{if } P_g \leq P_{ga} \end{cases} \tag{4}$$

where ρ_{ga} represents the atmospheric gas density.

Energy Balance

The energy content in the atmosphere is primarily influenced by shortwave and long wave radiation. The latter is determined by the properties of the surface of earth and cloud coverage. The key interaction between radiative and turbulent energy occurs at surface, meaning that soil characteristics and vegetation play a critical role in this process (Vilà-Guerau De Arellano et al., 2015). Figure 4 shows the main mechanisms of energy exchange.

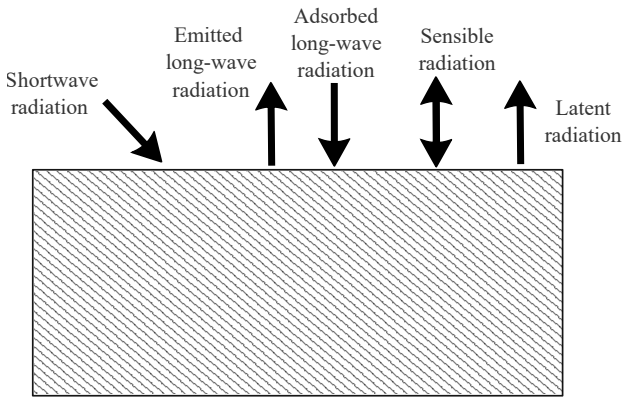

Figure 4: Major mechanisms of energy exchange at the soil–atmosphere interface. Taken from Sedighi et al. (2018).

The total flux of atmospheric energy (j_{atm}) reaching the surface can be calculated by summing the net radiation (R_n), convective heat flux (H_c), and sensible heat flux (H_s) as,

$$j_{atm} = R_n + H_c + H_s \tag{5}$$

where R_n serves as the primary driver of evapotranspiration and air-soil heat fluxes. The canopy intercepts net radiation, providing soil shading and regulating heat transfer to the soil. Furthermore, a portion of net radiation is utilized to heat the leaves and stems (Blight, 1997). To account for canopy effects, a radiation interception coefficient is applied, which typically ranges from 3% to 20% depending on the type of vegetation and its growth stage (Hemmati et al., 2012).

The net radiation (R_n) is determined as the difference between incoming and outgoing radiation and is formulated using the Stefan-Boltzmann law (Gens, 2010) as:

$$R_n = (1 - A_l)R_m + R_a - \epsilon\sigma_b T_0^4 \tag{6}$$

In this context, A_l represents the albedo, while R_a and R_m denote long-wave atmospheric radiation and measured solar radiation, respectively. The term $\epsilon\sigma_b T_0^4$ characterizes the long-wave radiation emitted by the vegetation, where T_0 is the soil temperature, ϵ is the surface emissivity, and σ_b is the Stefan-Boltzmann constant. Both A_l and ϵ are dependent on the degree of saturation (S_l), as outlined in the studies of Gascoin et al. (2009) and Sanchez et al. (2011), and can be expressed as,

$$A_l = A_d + (A_d - A_w)(S_l^2 - 2S_l) \tag{7}$$

$$\epsilon = 0.9 + 0.05S_l \tag{8}$$

Here, A_w and A_d represent the albedos for wet and dry conditions, respectively. The term R_a is related to absolute humidity and atmospheric temperature (T_a), as outlined by Allen et al. (1994), and is expressed as,

$$R_a = \sigma_b T_a^4 \left(0.605 + 0.048\sqrt{1370\rho_{va}}\right) \tag{9}$$

Since R_m is measured on horizontal surfaces, it needs adjustment for inclined surfaces. The modified solar radiation for an inclined surface ($R_{m,inc}$) is given by,

$$R_{m,\text{inc}} = R_{m,\text{hor}} \left[(1 - f_{\text{dif}}) \frac{\max(\mathbf{P}^T\mathbf{S}, 0)}{S_{\text{up}}} + f_{\text{dif}} \right] \tag{10}$$

Here, $R_{m,hor}$ is the solar radiation on a horizontal surface, and f_{dif} is the diffuse solar radiation fraction, calculated as,

$$f_{\text{dif}} = \frac{1}{1 + e^{(8.6\tau_a - 5)}} \tag{11}$$

In this case, τ_a represents the atmospheric transmissivity, while $\mathbf{P}$ and $\mathbf{S}$ are vectors that correspond to the positions of the sun and the zenith, respectively. These vectors are calculated as,

$$\begin{aligned} \mathbf{P} &= \begin{bmatrix} P_{\text{east}} \\ P_{\text{north}} \\ P_{\text{up}} \end{bmatrix} = \begin{bmatrix} \cos\alpha \sin\beta \\ -\sin\alpha \sin\beta \\ \cos\beta \end{bmatrix}, \\ \mathbf{S} &= \begin{bmatrix} S_{\text{east}} \\ S_{\text{north}} \\ S_{\text{up}} \end{bmatrix} = \begin{bmatrix} \cos\delta \sin\theta \\ \sin\delta \cos\lambda - \cos\theta \cos\delta \sin\lambda \\ \cos\delta \cos\lambda \cos\theta + \sin\delta \sin\lambda \end{bmatrix} \end{aligned} \tag{12}$$

In this context, α and β represent the surface strike and dip, while δ, θ, and λ correspond to the declination, solar angle, and latitude respectively.

H_c is computed by summing the internal energy of air, vapor, and water (Gens, 2010) as,

$$H_c = h_l \left(P + j_a^w\right) + h_v \left(E + j_g^w\right) + h_a j_a \tag{13}$$

where h_l, h_v, and h_a are the free energy of liquid water, vapor, and air, respectively. The air flux (j_a) is expressed by the mass fraction of atmospheric dry air and the gas flux as,

$$j_a = \omega_g^a q_g = \left(1 - \omega_g^w\right) q_g \tag{14}$$

where ω_g^w and ω_g^a are the water and the dissolved air fractions in the gas phase. The gas phase flux (q_g) is related to atmospheric pressure as follows,

$$q_g = \gamma_l \left(P_g - P_{ga}\right) \tag{15}$$

where P_g represents gas pressure at the soil surface. This flux carries two species, the dry air and the vapor. Furthermore, H_s is determined by the aerodynamic diffusion equation (Gens, 2010) as,

$$H_s = \rho_{ga} C_a \frac{k^2 v_a \phi}{\left(\ln \frac{z_a}{z_0}\right)^2} (T_a - T_0) \tag{16}$$

where C_a is the specific heat of air.

Vegetation role

Vegetation plays two important roles: hydrological and mechanical. Mechanically, plants enhance soil strength by transmitting tensile forces through their root systems. Evaluating the biomechanical properties of roots, including tensile strength and the modulus of elasticity, is essential for estimating their role in soil reinforcement (Ng et al., 2019). Numerous studies on root mechanical reinforcement have explored the relationship between root tensile strength (T_r) with root diameter (d_r) commonly described using the power decay law, expressed as,

$$T_r = k_1 d_r^{-k_2}, \quad \log(T_r) = \log(k_1) - k_2 \log(d_r) \tag{17}$$

where k_1 and k_2 are positive empirical fitting coefficients to be determined from the tests, and they are species dependent. Nevertheless, Ng et al. (2019) and Ng and Zhan (2007) pointed out that the relationships between root tensile strength and root diameter do not necessarily follow the commonly-quoted power decay law.

Ng et al. (2019) studied species such as *C. avellana* and *L. vulgare*, which exhibited an initial increase in tensile strength with diameter, peaking between 1.5–2.5 mm, followed by a decline for thicker roots. This deviation from the commonly assumed power decay law is attributed to anatomical differences between primary and secondary root structures.

Notably, tensile strength for roots smaller than 1 mm in diameter showed high variability, with measured values fluctuating by up to 50% in some cases. To account for this, the authors recommend restricting the application of the power decay law to roots with diameters greater than 2 mm, as applying it to finer roots, especially those <1 mm may lead to substantial overestimations of root reinforcement.

On the other hand, vegetation acts as an interface for transfering soil moisture to the air while absorbing atmospheric carbon dioxide for growth processes. The root system penetrates the soil, anchoring the plant and supplying water and mineral nutrients to the developing shoot (Moene and Dam, 2014). Water moves from the soil matrix to the root structure via mass flow, driven by the hydraulic head difference between the root surface and the surrounding soil particles, this hydraulic head gradient generates a convective flow of water, directing it towards the root surface (Moene and Dam, 2014). The soil-root

interface, characterized by radial flow toward individual roots, represents the most critical component of the system (Tarantino and Roberts-Self, 2023).

The impact of vegetation on slope dynamics requires the application of a flux model to simulate the evapotranspiration processes within the root zone. This model incorporates vegetation-specific data to estimate transpiration, evaporation, root zone drainage, and water interception by plants. The soil-water equilibrium is subsequently established for the root zone, which is defined by a depth corresponding to the root length and its associated water retention capacity (Badakhshan et al., 2024).

Sellers et al. (1986) propose that plant and soil resistances controlled evapotranspiration flux, which affect both sensible and latent heat transfer. At the soil surface, two parallel vegetation systems (grass cover and canopy) function alongside ground evaporation. The grass system includes a series of flow resistances: r_{sf} (soil-plant), r_{pf} (within plant), and r_{af} (plant-atmosphere).

These resistances control the transpiration flux between the groundwater potential at the root zone and the water potential at the leaf surface. Similarly, the canopy system incorporates resistances denoted as r_{sc} (soil-canopy), r_{pc} (within canopy), and r_{ac} (canopy-atmosphere). The Figure 5 illustrate the resistance model.

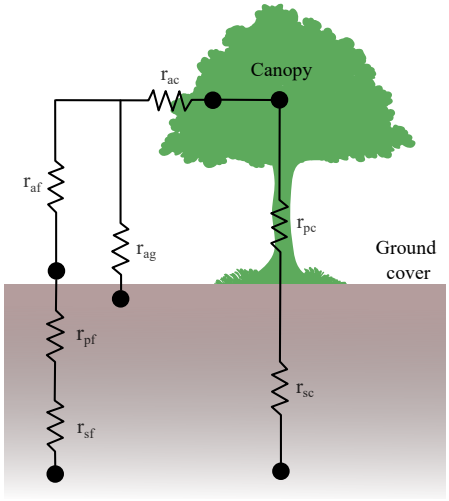

Figure 5: Resistances model for the Atmospheric-Plant-Soil upper layer. Modified from Samat (2016).

Building upon this framework, Noilhan and Mahfouf (1996) developed an equation to quantify the evaporation flux (E_v) based on the vapor concentration differential between the leaf surface and the surrounding air as,

$$E_v = (1 - veg)\frac{1}{r_a}(\rho_{va} - \rho_v) \tag{18}$$

In this context, r_a refers to aerodynamic resistance, which quantifies the resistance to both turbulent and molecular diffusion of water vapor from the leaf surfaces to the air above the canopy at a given reference height. The variables ρ_{va} and ρ_v represent the absolute humidity in the atmosphere and at

the boundary condition nodes, respectively.

The term veg indicates the proportion of the ground surface covered by vegetation (vegetation fraction), which is calculated as the vertical projection of the vegetation onto the ground.

An estimation of r_a is typically derived from the momentum flux, as proposed by Monteith (1965). This approach involves defining the wind profile, which is expressed as,

$$r_a = \frac{\left(\ln \frac{z_a}{z_0}\right)^2}{k^2 v_a \phi} \tag{19}$$

Likewise, transpiration flux (E_T) at the canopy is based on the work of Noilhan and Planton (1989). It is expressed as the difference between vapor density in the atmosphere and at the leaf level. Given that the relative humidity inside the leaf approaches 100%, it is considered to be at saturated vapor density conditions. This density is solely a function of leaf temperature, which is assumed to be equal to the atmospheric temperature. The relationship can be expressed as follows,

$$E_T = \text{veg} \frac{1}{r_a + r_s} (\rho_{vasat} - \rho_{va}) \tag{20}$$

In this equation, r_s represents the leaf surface resistance attributed to stomata, while ρ_{vasat} denotes the absolute humidity of the saturated atmosphere. It is important to note that r_s and r_a function in series within this context. r_s is characterized by four distinct functions, as described by Noilhan and Mahfouf (1996) and Jarvis (1976). These functions can be expressed as,

$$r_s = \frac{r_{s\,\min}}{LAI} \left[\frac{F_1}{F_2 F_3 F_4} \right] \tag{21}$$

where r_{smin} represents the minimum surface resistance. The LAI denotes the leaf area index, defined as the ratio of the total leaf area of a plant to the ground area it covers.

The F_1 function accounts for the effects of photosynthetically active radiation, following the formulation of Dickinson (1984), and is expressed as,

$$F_1 = \frac{1 + \left(\frac{1.1}{LAI} \frac{R_g}{R_{gl}}\right)}{\left(\frac{1.1}{LAI} \frac{R_g}{R_{gl}}\right) + \frac{r s_{\min}}{r s_{\max}}} \tag{22}$$

where R_g is the reference direct solar radiation and R_{gl} represents the upper limit of global radiation. The factor F_1 varies from 1 during overhead sun conditions to r_{smin}/r_{smax} at nighttime, where r_{smax} is the leaf cuticular resistance (maximum surface resistance).

The F_2 function, known as the stress factor, defines the ability of plants to extract water from the soil, which is influenced by the degree of saturation. It can be approximated using a modified version of the model proposed by Noilhan and Planton (1989), as,

$$F_2 = \begin{cases} 0 & S_l \leq S_{lwt} \\ \frac{S_l - S_{lwt}}{S_{lf} - S_{lwt}} & S_{lwt} < S_l \leq S_{lf} \\ 1 & S_{lf} < S_l \leq S_{la} \\ \frac{1 - S_l}{1 - S_{la}} & S_l > S_{la} \end{cases} \tag{23}$$

The wilting point (S_{lwt}) is the minimum soil moisture a plant needs to avoid wilting, typically at 1.5 MPa, though it varies by species. Field capacity (S_{lf}) is the moisture level where water stops moving downward, linked to suction values between 0.01 and 0.05 MPa. The anaerobiosis point (S_{la}) occurs when excess water and lack of oxygen impair plant metabolism, typically between 0.8 and 0.9, depending on soil texture.

The F_3 function accounts for the reduction in transpiration caused by stomatal closure under dry conditions, as described by Sellers et al. (1986), and is expressed as,

$$F_3 = 1 - \zeta(p_{vsat} - p_v) \tag{24}$$

where ζ is an empirical factor, typically ranging between 25 and 45 MPa^{-1}, and p_v and p_{vsat} represent the vapor pressure and saturated vapor pressure, respectively. The influence of the F_3 function on surface resistance emerges as a critical environmental constraint for transpiration in moist broadleaf forests, while its significance appears reduced for shorter canopies.

The F_4 function describes the dependency of stomatal resistance on T_a, following the model proposed by Dickinson (1984), and is expressed as,

$$F_4 = e^{-0.0016(298 - T_a)^2} \tag{25}$$

Higher temperatures increase the capacity of air to hold moisture, strengthening the driving force for water movement out of the plant and leading to higher transpiration rates.

Plant–atmosphere interaction models often face high complexity due to the wide variability in plant traits. For example, Badakhshan et al. (2024) reduce complexity by applying a generalizable parameterization strategy: vegetation is represented using fixed parameters, such as LAI = 1.95, vegetation fraction = 0.85, and standardized stomatal resistance functions (F_1–F_4) calibrated for Cynodon grass, thereby avoiding species-specific modeling while preserving key functional dynamics.

Evapotranspiration Dynamics

According to Tarantino and Roberts-Self (2023), evapotranspiration (ET) occurs under two distinct regimes: *energy-limited* and *water-limited*. The energy-limited regime, also referred to as potential evapotranspiration (PE), arises when the soil-plant system is capable of fully meeting atmospheric water demand. This process is primarily driven by two factors: R_n, which supplies the

latent heat required for water vaporization, and near-surface vapor pressure. The latter is influenced by both far-field water vapor pressure and local air turbulence.

As soil moisture decreases and hydraulic conductivity declines, the soil-plant ability to meet atmospheric water demand is diminished, leading to a transition from an energy-limited to a water-limited regime (Tarantino and Roberts-Self, 2023). In this state, actual evapotranspiration (AE) falls below the potential rate due to insufficient water availability. Scott et al. (2021) pointed out that in water-limited systems, such as grasslands, ET is primarily controlled by soil moisture from recent precipitation. The transpiration-to-evapotranspiration (T/ET) ratio fluctuates with seasonal changes, decreasing during dry periods due to reduced water availability.

In contrast, ecosystems with access to groundwater, maintain higher and more stable T/ET ratios. Water-limited ET regimes highlight the critical role of soil moisture, precipitation, and vegetation in controlling the balance between evaporation and transpiration.

Zooming in to the plant root scale reveals a complex interplay of atmospheric conditions, plant physiology, and soil properties governing water uptake; while microscopic models strive to integrate all these physical factors comprehensively, macroscopic approaches simplify the process by considering fewer variables. This simplification enhances their applicability but necessitates the calibration of semi-empirical parameters (Moene and Dam, 2014).

Consequently, the temporal variations in root depth and density induce alterations in the vadose zone properties (Samat, 2016). These dynamic interactions underscore the intricate relationship between vegetation and soil hydrology.

A widely used macroscopic method for modeling water uptake by vegetation defines AT as the product of potential transpiration (PT) under energy-limited conditions and a reduction factor (β) that varies with the suction in the root zone (s_{bulk}), as outlined by Tarantino and Roberts-Self (2023), and is given by,

$$AT = PT \cdot \beta(s_{bulk}) \tag{26}$$

When soil water conditions are optimal, the root water extraction rate reaches the maximum PT rate ($\beta = 1$). In contrast, when the soil is either excessively dry or wet, transpiration decreases, governed by the factor ($\beta < 1$). According to Feddes (1982), this reduction factor is determined by soil suction in the root zone, as shown in Figure 6.

ET is considered zero when suction falls below the anaerobiosis point (S_{la}) or exceeds the wilting point (S_{lwt}). Maximum transpiration ($\beta = 1$) occurs between s_2 and s_3, where s_3 represents the soil suction threshold beyond which plant transpiration starts to be constrained. This suction threshold, s_3, signifies the shift from energy-limited (potential) evapotranspiration ET_{lim} to water-limited evapotranspiration, as described by Nyambayo and Potts (2009).

Additionally, root architecture is crucial in regulating the water-limited regime. Figure 7 illustrates water-limited evapotranspiration for bare soil and

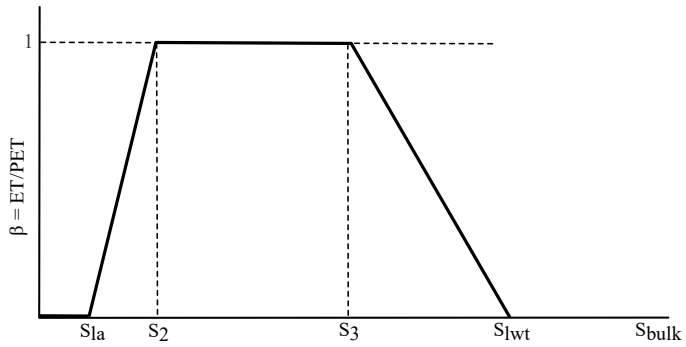

Figure 6: Feddes reduction function. Modified from Tarantino and Roberts-Self (2023) and Nyambayo and Potts (2009).

vegetated soil with two distinct root depths.

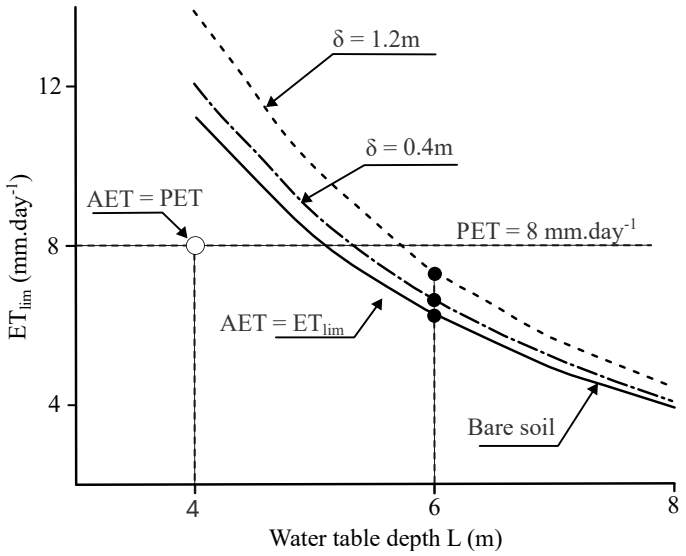

Figure 7: Effect of mode of extraction on water-limited evapotranspiration under steady state conditions (δ = depth of root zone). Taken from Tarantino and Roberts-Self (2023).

Roots enhance water flux to the atmosphere, particularly at root zone depths of 0.4 m and 1.2 m. In water-limited conditions (e.g., water table depth 6 m, $PET = 8\ mmday^{-1}$), ET varies between bare and vegetated soils, increasing with root depth in vegetated soil. However, during ET_{lim}, both soil types show identical flux regardless of root depth, assuming equal PET (Tarantino and Roberts-Self, 2023).

The Feddes approach to modeling the reduction function is widely applied in geotechnical and agricultural studies (Nyambayo and Potts, 2009; Peters et al., 2017). This method is advantageous as it only requires information about pore-water pressure in the root zone. Transpiration can be modeled using a suction-dependent sink term in the water flow equation (Tarantino and Roberts-Self, 2023).

The challenge of selecting appropriate Feddes parameters is evident in the wide range of values for s_3 found in the literature, being this one, the most critical parameter. The threshold suction s_3 can be derived analytically as,

$$s_3 = \frac{\gamma_w}{\alpha} \cdot \ln \left(\begin{array}{l} PT \dfrac{\alpha}{2 \cdot \pi K_s} \cdot \ln \left(\dfrac{1/\sqrt{\pi RLD}}{r_{\text{root}}} \right) \cdot \dfrac{1}{RLD \cdot \delta_{\text{root}}} \\ + \exp \left(- \dfrac{\alpha s_{\text{root,crit}}}{\gamma_w} \right) \end{array} \right)^{-1} \tag{27}$$

Here, γ_w represents the unit weight of water, and K_s denotes the saturated hydraulic conductivity, which quantifies the capacity of soil to transmit water under full saturation conditions.

The equation also incorporates the impact of root architecture, defined by RLD, the root length density (total root length per unit soil volume), r_{root}, the root radius, which influences water absorption at the soil-root interface, and δ_{root}, the layer thickness at the root surface that affects water uptake (Tarantino and Roberts-Self, 2023). For example, an accurate description of the RLD distribution is essential for studying crop growth, soil–root interactions, and root water/nutrient uptake from the soil–plant system (Ahmadi et al., 2014).

Figure 8 highlights the effectiveness of the s_3 parameter in representing the experimental data on transpiration reduction reported by Denmead and Shaw (1962). The study investigated the influence of potential transpiration rates on corn plants grown in silty clay loam. Field experiments were conducted using containers with a diameter of 450 mm and a height of 610 mm, where irrigation was periodically suspended to induce soil moisture depletion. Variations in PT rates throughout the experiment facilitated the derivation of T reduction curves under different PT conditions.

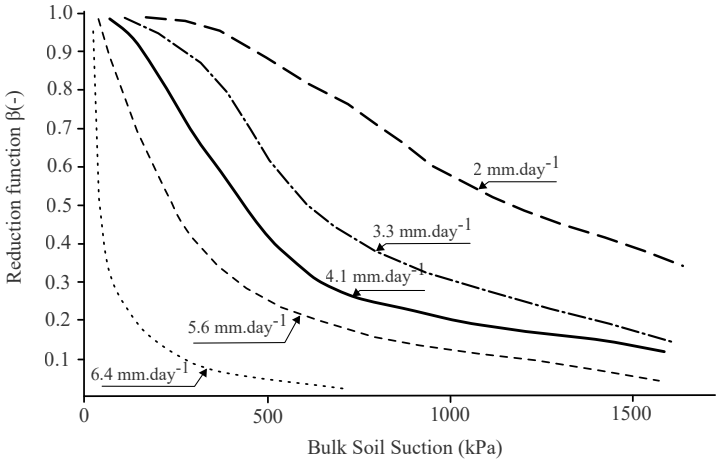

Figure 8: Effect of potential transpiration rate on threshold suction s_3 and overall transpiration reduction function for corn plants and silty clay loams. Taken from Tarantino and Roberts-Self (2023).

Ng et al. (2019) studied how plant morphology affects soil suction response in *Schefflera heptaphylla*. Using five plant height groups, they measured transpiration data as Water Uptake Length Ability (WULA). Tarantino and Roberts-Self (2023) converted WULA into transpiration rates by factoring in RLD and Depth (Figure 9). Results showed that threshold suction s_3 decreases with higher transpiration rates but increases with higher RLD, suggesting that root architecture influences the shift from energy-limited to water-limited regimes.

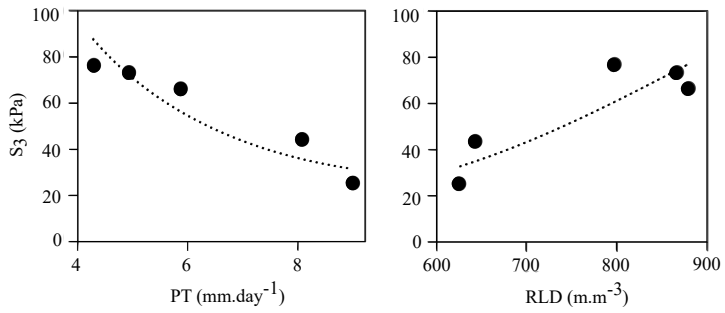

Figure 9: Effect of *PT* rate and *RLD* on threshold suction s_3 for *S. heptaphylla* tree in silty sand. Taken from Ng et al. (2019) as cited in Tarantino and Roberts-Self (2023).

However, Tarantino and Roberts-Self (2023) identifies key limitations in the use of empirical models, like the Feddes function, for modeling evapotranspiration in water-limited regimes. These models often fail to capture the complex physical interactions, particularly when soil moisture levels are low and hydraulic conductivity is reduced. This results in inaccurate predictions of transpiration and its effects on slope stability. To address this issue, the development of physically-based models is necessary.

The main bottlenecks are the reduced hydraulic conductivity of the soil as water content decreases, limitations at the soil-root interface where water uptake is hindered, the resistance in the xylem preventing efficient water transport from roots to leaves, and stomatal closure when leaf suction reaches a critical level (Tarantino and Roberts-Self, 2023).

Soil-Atmosphere: study cases

This section explores the influence of Root System Architecture on soil behavior, and, on the other hand, examines how coupled interactions are typically addressed in geotechnical monitoring, supported by data from in-situ observations and numerical models.

Root architecture

In recent years, advanced models have been developed to simulate root water uptake, describing the movement of water from the soil to the roots, through the root system, and into the plant. Root water uptake is primarily controlled by the total soil water potential. However, these mechanistic models often require extensive input data, such as spatial root distribution and architecture, which are not always available (Peters et al., 2017).

As mentioned previously, Ng et al. (2019) develop a series of experiments studying the effects of plant morphology and density of *Schefflera heptaphylla* and its influence on the induced suction under *ET* and *P* conditions. After a 2-hour rainfall, suction in bare soil decreased significantly in the top 150

mm, while vegetated soils with 120 mm and 180 mm root spacing showed less impact. However, 60 mm spacing exhibited deeper suction changes, likely due to root decay and increased permeability. Suction below 250 mm remained unchanged. The results indicate that higher planting densities enhance infiltration and reduce suction retention in the root zone, highlighting the importance of plant density and root architecture in influencing suction distribution.

Ng et al. (2015) also provides a closed-form analytical solutions for steady and transient-state conditions to examine the influence of four idealized root architectures (exponential, triangular, uniform, and parabolic) on soil suction distribution and slope stability in unsaturated vegetated soils. The Figure 10 show the main root geometries described by Lynch (1995), Ghestem et al. (2014) and Leung et al. (2015) as cited in Ng et al. (2015).

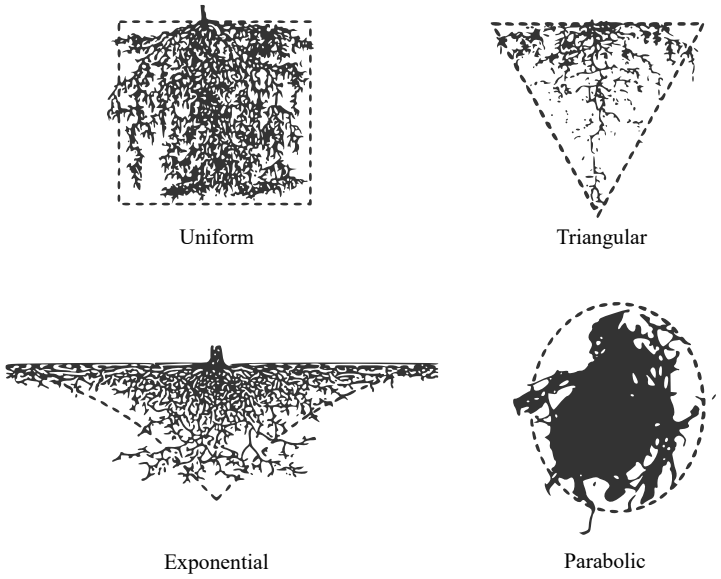

Figure 10: Four typical root architectures observed in the literature. Adapted from Ng et al. (2015).

The findings show that vegetated slopes retain more suction than bare slopes, especially below the root zone, due to plant transpiration reducing water permeability, effectively maintaining drier conditions and enhancing matric suction at depth. Of the root architectures studied, the exponential distribution produces the highest suction, making it most effective for shallow slope stabilization. Both exponential and triangular architectures induce the highest suction at the slope surface, with values up to 95 kPa for a 0.3 m root depth—nearly double that of deeper roots. Transpiration-induced suction extends to about six times the root depth, preserving suction even below the root zone, particularly at depths of 1–1.5 m, where 30% more suction was observed compared to bare slopes.

Transpiration during heavy rainfall has little effect on maintaining suction or slope stability, as suction at shallow depths drops to near zero, making the differences between bare and vegetated slopes negligible. However, below the root zone, vegetated slopes retain up to 30% more suction than bare slopes,

indicating lower water content at depth due to sustained transpiration, not reduced infiltration, leading to a 15% higher factor of safety at depths of 0.5 m. Pre-rainfall soil drying and root-induced changes in permeability, which reduce rainfall infiltration by altering soil water retention, are the main factors influencing suction distribution and slope stability.

Wang et al. (2020) thoroughly evaluated the influence of six different root tree architectures on slope stability, focusing on both hydraulic and mechanical soil properties. The Figure 11 show the geometries described by Yen (1987) and Li et al. (2017) as cited in Wang et al. (2020).

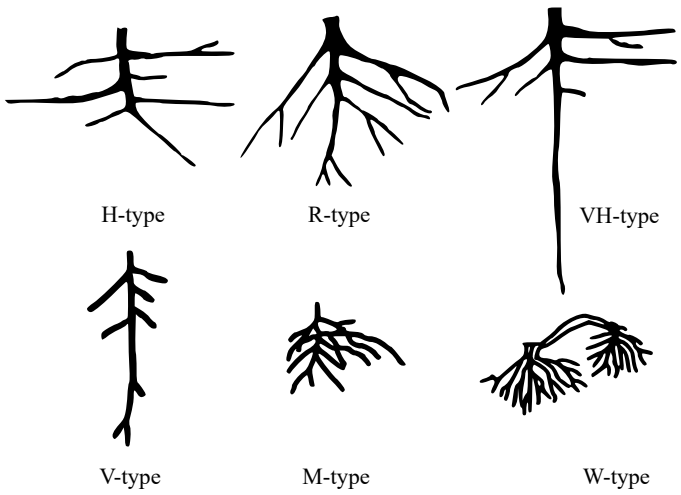

Figure 11: Six branching patterns of tree root architectures. Taken from Wang et al. (2020).

Roots increased the saturated hydraulic conductivity (K_{sat}) by 1 to 4.23 times compared to bare soil, with W-type roots demonstrating the highest K_{sat} values, ranging between 36.6–43.2 mmh^{-1}, while H-type roots showed the lowest (14.4–18 mmh^{-1}). In contrast, bare soil exhibited a K_{sat} between 7.2–9 mmh^{-1}.

Regarding mechanical stability, root-soil composites significantly improved soil cohesion by 35.19–81.79% and the internal friction angle by 12.92–42.36%. The improvement in soil cohesion is mainly due to the tensile resistance and bridging effect of roots, which mechanically reinforce the soil matrix and limit deformation under shear stress. Among the root architectures, R-type and V-type roots contributed the most to increasing peak shear stress, enhancing it by up to 47.73%. Additionally, these root types extended the rainfall intensity-duration threshold for slope failure, indicating their effectiveness in stabilizing steep terrains. The findings suggest that vertical and inclined root systems, particularly R-type and V-type, are most beneficial for improving slope stability under intense rainfall conditions (Wang et al., 2020).

Reubens et al. (2007) highlights the important contribution of both fine and coarse roots to slope stability and erosion control. Fine roots, with diameters less than 3 mm, are particularly effective in stabilizing surface soils by reducing erosion through increased soil cohesion. Coarse roots, often greater than 20

mm in diameter, penetrate deeper soil layers, providing critical anchorage and helping prevent slope failure by increasing shear strength at failure planes.

Research indicates that fine roots can reduce interrill and rill erosion by up to 90%, while coarse roots contribute more to slope reinforcement, particularly when the shear plane is located at depths of 0.5–1 m. The *root area ratio* and RLD are key parameters, with studies showing that higher values of these parameters correspond to greater erosion control and slope reinforcement. For example, an increase in RLD to 1–2 $cmcm^{-3}$ can reduce erosion intensity exponentially, highlighting the strong relationship between root architecture and soil stabilization.

Geotechincal monitoring

These study cases of AS monitoring and numerical cases were documented in Elia et al. (2017). The authors analyzed both real and hypothetical scenarios, applying various numerical strategies to investigate the effects of climate-induced perturbations on the stability of natural and artificial slopes.

Their work emphasizes the impact of coupled interactions on the stability of engineered slopes. The studies also included the use of field instrumentation, allowing validation of the numerical models and better understanding of the mechanisms driving slope failures.

The *Middelburgse Kade Peat Dyke* study involved monitoring groundwater head data over a two-year period using four observation wells. Hydraulic head differences were modeled using a finite-volume Dupuit approach and compared to finite-element simulations based on Richards equation. Both methods produced consistent results for pore pressure and critical slip surfaces. An analysis showed that doubling the evapotranspiration rate could have caused dyke failure, highlighting the significant role of evapotranspiration in dyke stability, which was calculated using the Penman–Monteith equation. The vegetation on the dyke helped modulate evapotranspiration, providing crucial input for accurate stability predictions.

The *Volturino Slope* study used piezometric data from depths of up to 50 meters to observe seasonal fluctuations in pore water pressure, which contributed to landslide reactivation. Hydro-Mechanical models developed with PLAXIS 2D simulated stress strain behavior under varying seasonal conditions. A pre-existing deformable zone overlying the shear band at 50 m depth had long exhibited progressive strain accumulation driven by seasonal pore pressure variations. Instrumentation and back-analysis confirmed that creep-induced displacements and microstructural weakening in silty-clayey soils within this 50 m thick layer played a key role in conditioning the delayed activation of the deep-seated failure surface. Seasonal pore pressure fluctuations within the pre-shear zone, influenced by rainfall and vegetation (grass and scattered shrubs), played a critical role in triggering progressive deformations and conditioning delayed slope failure.

Authors like Oorthuis et al. (2020) performed a detailed study on an embankment divided into four partitions (North Vegetated, North Non-Vegetated, South Vegetated, South Non-Vegetated), with vegetation composed of *Cynodon dactylon* (80%) and *Festuca arundinacea* (20%), selected for their drought tolerance and ability to enhance soil strength. The study monitored volumetric water content, matric suction, soil temperature and heat flux over 2.5 years. Results showed that vegetated slopes experienced faster and higher increases in soil moisture during rainfall events, 15–20% more compared to bare slopes, and exhibited faster drying rates, up to 1.5% per day.

Suction values in vegetated slopes were higher and more variable, ranging from 10 kPa to 100 MPa, while non-vegetated slopes had lower suctions (10 kPa to 1 MPa). Additionally, vegetation reduced soil heat inflow by 75% in South-facing slopes, decreasing maximum daily temperatures by 15 °C, compared to a reduction of less than 5 °C in North-facing vegetated slopes. Vegetation enhanced infiltration and accelerated drying, while slope orientation had a secondary impact on thermal and hydraulic behavior. The study concluded that vegetation plays a dominant role in modulating infiltration, enhancing soil drying through transpiration, and buffering thermal fluctuations. These effects collectively reduce pore water pressures and surface runoff, thereby improving slope stability under both hydrological and thermal stresses.

In the research developed by An et al. (2018), a coupled Thermo-Hydraulic model was applied to an experimental embankment in Héricourt, France, to assess the water and heat transfer dynamics. Using numerical modeling, the water fluxes (rainfall, infiltration, runoff, and evaporation) and heat fluxes (solar radiation, latent heat, and sensible heat) were analyzed. The results showed that rainfall and infiltration had similar magnitudes ($\sim 10^{-6}$ m/s), significantly larger than evaporation and runoff ($\sim 10^{-8}$ m/s), indicating the dominant role of rainfall in soil water movement. In terms of heat flux, solar radiation drove the soil heat flux, with positive values during the day and negative at night, while latent heat flux remained negative due to continuous evaporation.

Sensible heat flux varied with the temperature differences between soil and air. Climatic conditions influenced soil moisture and temperature differently, with soil moisture depth reaching 2-3 meters, while temperature effects extended up to 4 meters. This variation occurs because water moves vertically under gravity, whereas heat transfer is more uniform in all directions. These findings emphasize the importance of Thermo-Hydraulic processes and how seasonal Soil-Atmosphere interactions drives the embankment stability, as climate changes can significantly alter moisture and temperature, impacting slope stability.

Badakhshan et al. (2024) developed numerical modelling to analyze the effects of meteorological forces and vegetation on the thermal and hydraulic behavior of slopes, using the Code_Bright finite element model, validated with three years of field data from a slope in Barcelona, Spain. The model, incorporating hydraulic hysteresis and canopy resistance, revealed that vege-

tation reduces daily temperature fluctuations by 10-15°C in the root zone (up to 30 cm depth), while at greater depths (36-56 cm), fluctuations were reduced to 3-5°C. South-facing slopes exhibited temperatures 15°C higher than north-facing slopes, with maximum temperatures reaching 45°C in summer. Vegetated slopes had drying rates up to 50% higher than non-vegetated slopes under high-temperature, low-rainfall conditions, with soil moisture decreasing by 0.5-1% per day in the top 16 cm. Vegetation also increased soil suction by 10-20%.

Aditionally, Masi et al. (2021) highlight the critical role of root reinforcement in slope stability, with roots increasing soil tensile strength 4 to 20 MPa for grass roots and 5 to 70 MPa for tree roots. Fine roots enhance cohesion, while large roots anchor soil layers, significantly improving shear resistance. Hydrologically, vegetation reduces soil moisture through suction and interception, delaying saturation and preventing landslides.

Models such as those developed by Wu et al.(1979), as cited in Masi et al. (2021), are commonly employed to estimate root reinforcement in slope stability analyses. However, these models operate on the assumption that all roots intersecting the shear plane simultaneously reach their maximum tensile strength and fail at the same instant. This simplification can lead to significant overestimations of the safety factor - by up to 10% or more, particularly in cases of small-scale landslides.

To address these limitations, Pollen and Simon (2005) and Pollen (2007), as cited in Masi et al. (2021), proposed the Fiber-Bundle Model (FBM), which provides a more realistic simulation of root reinforcement through its ability to model progressive root failure. The FBM incorporates actual measurements of root tensile strengths and diameters, offering improved accuracy in slope stability assessments.

Nevertheless, Masi et al. (2021) report, even the FBM faces challenges due to the extreme spatial variability of root properties, which complicates their reliable inclusion in large-scale slope models. Field studies show that root biomass, architecture, and mechanical traits vary significantly even among individuals of the same species, age, and site, making species-specific calibration essential for accurate modeling.

Conclusions

The coupled framework is a well-established approach for modeling the complex interactions within porous media, such as soils and rocks, and is supported by a range of advanced numerical platforms. These platforms enable precise simulations of coupled thermal, hydraulic, and mechanical processes, providing a robust foundation for analyzing soil behavior under various environmental and mechanical conditions.

In SA, vegetation plays a vital role in slope stability by influencing hydrological processes, such as evapotranspiration and root water uptake, and providing mechanical reinforcement through root systems. However, most models oversimplify these effects by treating root-soil interactions as static boundary conditions. Parameters like root water uptake and suction are often adjusted via trial and error, without fully capturing real dynamics, thus limiting model accuracy.

A key area for improvement is the representation of root architecture, including its geometry, depth, and density, which significantly impacts soil moisture and suction—both critical for slope stability. Current models frequently overlook how root systems evolve, decay, and redistribute over time, leading to potential overestimation of the vegetation stabilizing effects. Additionally, mechanical reinforcement from roots, which varies by species and soil type, is often generalized, reducing the accuracy of long-term slope stability predictions, especially under changing climatic conditions.

Monitoring is crucial for addressing these limitations. Field data of pore pressure, soil suction, temperature, piezometric levels and moisture content help refine models and better capture the real-time effects of vegetation on soil stability. Monitoring also enhances understanding of how root geometry and density affect soil hydrology and stability, leading to more accurate numerical simulations.

Integrating dynamic vegetation processes, especially root architecture and densit remains a challenge. Current models often rely on static assumptions and parameter tuning, limiting their ability to fully capture plants role. Incorporating detailed geotechnical monitoring and improving the representation of root systems will lead to more accurate predictions of slope stability and soil behavior in vegetated areas.

Recent research has expanded our understanding of influence of vegetation on slope stability, yet challenges remain in modeling the spatial and temporal variability of root zones across large areas.

Finally, monitoring is often used solely for model calibration or time-dependent analysis; however, data-driven techniques could enhance the analysis of coupled interactions, especially in scenarios where instrumentation provides mid- to long-term historical records and multiple monitored variables.

Root System Architecture Analysis for Atmosphere-Plant-Soil Applications

Abstract

It is widely known that vegetation characteristics influence slope stability through root geometry, depth, and density, exerting hydrological effects by reducing pore-water pressure via evapotranspiration and mechanical effects by enhancing soil suction, shear strength and cohesion.

Despite their critical role in soil behavior and stability, detailed root zone characteristics remain largely inaccessible. A methodology for Root System Architecture analysis was developed using digital image processing to enhance understanding of root zone display in the Atmosphere-Plant-Soil system. Root architecture analysis demonstrated significant potential for bioengineering applications, offering improved accuracy in assigning root-dependent parameters for hydrological and mechanical models and reducing associated uncertainties.

High-resolution images of roots from *Chrysopogon spp.* and *Arachis pintoi* were analyzed to calculate geometrical parameters such as volume, area, diameter, root area ratio and fractal dimension under varying dry soil densities (1.0 and 1.3 kgm^{-3}). These species were selected due to their different root systems and their current relevance in geotechnical and other environmental applications. The method effectively represented RSA in both species, revealing that soil density and particle size significantly influence root branching, volume, and how roots explore soil matrix.

In more compacted soils, *Chrysopogon spp.* showed reductions of 12.2% in fractal dimension, 61.9% in volume, 71.2% in surface area, and 55.9% in RAR, while diameter increased by 27.8%. For *Arachis pintoi*, reductions were 5.5% in fractal dimension, 37.5% in volume, 33.1% in surface area, and 23.9% in RAR, with a 11.5% increase in diameter. Compaction and silty-clay soils result in wider, less branched roots, limiting depth, water uptake and soil exploration.

Introduction

The type, quantity, and condition of vegetation cover significantly affect the flux exchanges between the surface of Earth and the nearby atmosphere (Taylor and Lebel, 1998, as cited in McPherson 2007). Plants intercept water during rainfall and also drips water into the ground and evaporates moisture directly into the atmosphere, impacting incoming radiation through albedo differences, absorption of short- and long-wave radiation and emission of long-wave radiation (Segal et al., 1988; Lakhtakia and Warner, 1994, as cited in McPherson 2007). Moreover, both evapotranspiration rates and root water and nutrient uptake are influenced by the qualitative and quantitative properties of vegetation canopy and root system (e.g. root density, roots surface, Leaf Area Index), however due to limited and fragmented data on root distribution and quality under natural conditions, current models often rely on assumptions and empirical estimations (Sachan et al., 2023).

In geotechnical scenarios, the influence of trees and grasses on slope stability is significant, as their root networks enhance soil shear strength, reducing erosion and preventing shallow landslides through water uptake and transpiration (Yin et al., 2024). Ng et al. (2020) demonstrated in slope stability simulations using 3D-printed root structures, that root networks push the shear plane deeper into the soil profile. The effectiveness of root reinforcement is influenced by species-specific root mechanical properties, confining stress, initial shear plane depth, and root system architecture (RSA).

In this context, Noilhan and Mahfouf (1996) established essential parameters based on plant morphology for evapotranspiration estimation. These parameters have been integrated, for example, into numerical models (e.g. Olivella et al. 2023, Badakhshan et al. 2024), where their accurate definition is essential for simulating hydrological and thermal balance. This approach also enables a detailed representation of its temporal evolution, serving as a dynamic boundary condition (BC) (Badakhshan et al., 2024). Typically, this BC remains static, with parameter assignment often relying on a trial-and-error approach to achieve the best fit, and RSA derived parameters are not always explicit and easy to obtain. This highlights the unrepresented role of vegetation and root systems within the Soil-Atmosphere system, particularly in numerical implementations, which demands more understanding of geometric parameters and a transient perspective of root zone.

Analytical approximations have been developed for standardized root geometries (Ng et al., 2015). However, the influence and quantification of the root zone geometrical parameters remains an open area of research, especially considering an environmental change context (Sachan et al., 2023). Hence, visualization techniques can offer useful tools for better analysis. Reconstruction techniques can be very sophisticated, especially in 3D. Recent advances in non-invasive techniques, such as X-ray computed tomography, provide a precise method for examining root architecture in detail (Tracy et al., 2010;

Hou et al., 2022). Generally, these methodologies rely on expensive and sophisticated instrumentation. In contrast, 2D image processing emerges as a promising and cost-effective alternative. However, as previously mentioned, obtaining accurate RSA parameters particularly for metrics such as root length density (RLD), root radius, rooting depth, diameter among others remains a challenge.

The main objective of this research is to develop a simplified workflow for visualizing roots through digital image processing of 2D root images for two species with differing RSA: *Chrysopogon spp.* and *Arachis pintoi cv. Belmonte*, and calculate root parameters such as volume, diameter, root area ratio, fractal dimension as a proxy parameter for RLD, among others, across different locations and growth conditions, minimizing reliance on trial-and-error methods. Ultimately, it seeks to enhance and support applications in bioengineering and agriculture.

Methodology

Plant species and image adquisiton

In Figure 12 is the flow chart for analyzing the root images datasets. The methodology was divided into three major steps: 1) preprocessing of scanned root images (Figure 12 “step 1”), 2) root architecture parameters calculation (Figure 12 “step 2”) and 3) image post-analysis (Figure 12 “step 3”).

The visualization and geometrical parameter calculation methodology was performed with two herbaceous plant species. The selection was based on their different root system morphologies. The first species is *Chrysopogon spp.*, a perennial grass with a dense fibrous root system that can grow rapidly and reach depths of up to 3 meters (Liu et al., 2021). The second species is *Arachis pintoi*, a perennial stoloniferous legume with a dense taproot system that is much shallower than *Chrysopogon* (Shamim et al., 2021). To monitor their growth and the evolution of root system, fifteen samples were planted; eleven in regular pots at EAFIT University with soil dry density close to 1.0 $kgm^{-}3$, while the other four were planted in a natural soil parcel with coordinates 5°46’4.15"N and 75°52’43.70"W located in Hispania (Antioquia) with a dry density close to 1.3 kgm^{-3}. Appendix 2 contains the soil laboratory tests of the soil were the plants growth. The greenhouse conditions indicated that the soil was organic, and the growth period was less than 8 days.

The scanner used was HP ScanJet G4050 with a black background to enhance the contrast of the roots. The image resolution was set to 300 dpi. Individual image saturation and color were adjusted according to the histogram of each photo using ImageJ, to better highlight the roots. Root samples were manually separated from the soil, with careful washing to remove all dirt particles, ensuring minimal damage to the samples.

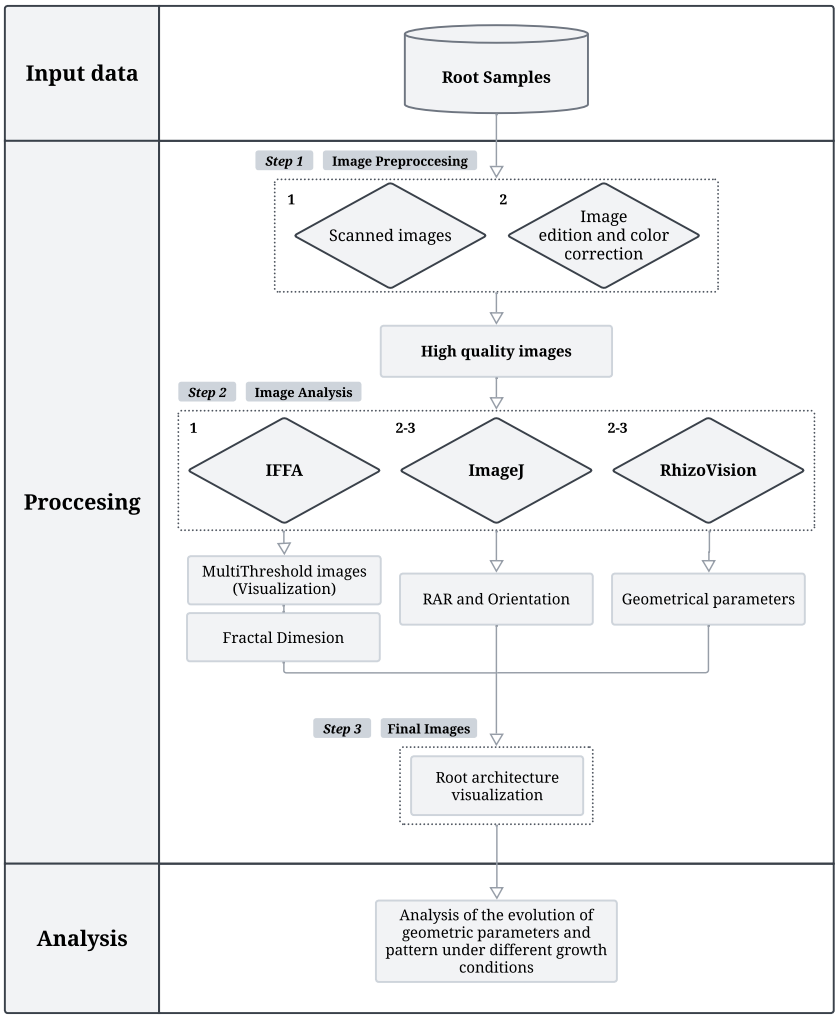

Figure 12: Methodology for image root processing.

Root visualization

The IFFA algorithm is an automatic 2D root image processing tool based on Frangi filter, developed by Gong et al. (2021). It offers a pixel accuracy of 97.48%, an Intersection Over Union Index (IOU) of 63.8%, and a Dice Similarity Coefficient (DSC) of 77.9%. The code is implemented in MATLAB.

The visualization of plant roots in this methodology involves several key steps. The process begins with a Gaussian filter applied to the image to reduce noise (Gong et al., 2021). The smoothing function is given by,

$$G(x, y) = \frac{1}{2\pi\sigma^2} \exp\left(-\frac{x^2 + y^2}{2\sigma^2}\right) \tag{28}$$

where σ controls the extent of smoothing, and x and y represent the spatial coordinates of the image.

Next, the Hessian matrix is computed at each pixel of the smoothed image

to detect root-like tubular structures (Gong et al., 2021). The Hessian matrix is defined as,

$$H = \begin{pmatrix} \frac{\partial^2 I}{\partial x^2} & \frac{\partial^2 I}{\partial x \partial y} \\ \frac{\partial^2 I}{\partial x \partial y} & \frac{\partial^2 I}{\partial y^2} \end{pmatrix} \tag{29}$$

where $I(x, y)$ represents the image intensity.

The Hessian matrix is then decomposed to obtain its eigenvalues, λ_1 and λ_2, which provide information about the curvature of the structures in the image. If $|\lambda_1| \gg |\lambda_2|$, this indicates the presence of a tubular structure such as a root (Gong et al., 2021).

The Frangi filter is subsequently applied to enhance root-like structures by analyzing the eigenvalues of the Hessian matrix (Gong et al., 2021). The vesselness function V for each pixel is computed as,

$$V = \begin{cases} 0 & \lambda_2 > 0 \\ \exp\left(-\frac{R_A^2}{2\alpha^2}\right)\left(1 - \exp\left(-\frac{S^2}{2\beta^2}\right)\right) & \lambda_2 \leq 0 \end{cases} \tag{30}$$

where $R_A = \frac{|\lambda_2|}{|\lambda_1|}$ is the "blobness" measure, $S = \sqrt{\lambda_1^2 + \lambda_2^2}$ is the second-order structureness, and α and β are parameters that control sensitivity to noise and the thickness of the structures.

After applying the Frangi filter, the image undergoes thresholding to segment the roots from the background (Gong et al., 2021). Some adaptations to the original code were made due to the root systems analyzed.

The updated script was able to work with an unlimited number of images and enabling better visualization of thicker roots (higher biomass) modifying the multithresh threshold. Also filling methods were included for images with thicker roots and small holes remaining after the main multithresh result, adding an octagonal structuring element, finally, all images had a pixel/cm-based scale. These changes have been made while maintaining the original functionality of the script.

A skeletonization and fractal dimension processing was also added to the script. A skeletonization process reduced segmented root structures to one-pixel-wide centerlines. The resulting 2D skeletonized binary images were used to calculate the fractal dimension using the box-counting method, quantifying branching levels (Wu et al., 2020), described as,

$$D = \lim_{\epsilon \to \infty} \left[\frac{\ln N_\epsilon}{\ln \epsilon^{-1}} \right] \tag{31}$$

where N_ϵ is the number of boxes containing any foreground pixel at each caliber, and ϵ is the box size.

Moreover, Phan and Likitlersuang (2024) proposed a user-friendly methodology for calculating key root parameters such as Root Area Ratio (RAR) and root orientation. Specifically, the RAR is computed by dividing the total root area by the area of the segmented image, while root orientation is determined by analyzing the angular distribution of root segments. The methodology was

replicated using ImageJ. The processed images using the IFFA algorithm were subsequently migrated to this processing methodology for further analysis.

Aditionally, RhizoVision+ Explorer, an open-source software designed for root image analysis, was used for measurements of root characteristics such as length, diameter, area, volume and root depth (Seethepalli et al., 2021). The software uses broken root mode for root image analysis, and it enables the options of filling and filtering non-root objects. Geometric parameters were calculated in physical units using the original image resolution. Additionally, the non-root objects from the background were filtered by entering a 0.3 maximum pixel size value. The technical details for each parameter calculated can be found in Seethepalli et al. (2021).

Results

Root image visualization

In Figure 13 are displayed some examples of binary representations of the analyzed roots systems trough digital image processing. In Figure 14 are displayed the bar diagrams of diameter distribution of some samples as an example of one of the parameters. The geometric parameters are in Table 2 for *Chrysopogon spp.* and Table 3 for *Arachis pintoi cv. Belmonte* samples, respectively.

Variable	**Samp. 12**	**Samp. 13**	**Samp. 14**	**Samp. 2***	**Samp. 3***	**Samp. 4***	**Samp. 1***
Species				*Chrysopogon spp.*			
Dry Soil Dens. (kgm^{-3})	Greenhouse	1.0	1.0	1.3	1.3	1.3	1.3
Growth St. (days)	< 8	30.40	30.40	37.00	37.00	37.00	37.00
Fractal Dim.	1.54	1.60	1.61	1.41	1.52	1.56	1.41
Root Lgth. (mm)	18026.8	62251.9	66637.1	14738.3	32676.6	37275.6	14118.6
Net. Area (mm^2)	27986.5	69075.2	75497.8	21101.1	41234.4	49177.4	21063.1
Avg Dia. (mm)	2.29	1.50	1.56	1.90	1.65	1.78	2.01
Med Dia. (mm)	1.83	1.33	1.33	1.60	1.33	1.41	1.78
Max Dia. (mm)	9.94	9.76	10.46	14.77	6.61	11.36	12.73
Perim. (mm)	25463.9	102366	106889	24054	54131	59548	22725.3
Vol. (mm^3)	98453	138948	161633	55264	86409	116646	59268.4
Surf. Area (mm^2)	127522	288034	320597	87012	167058	205239	87939.6
Avg RAR (%)	10.96	34.21	32.46	15.96	22.41	22.37	13.43
Avg Orient. (°)	83.96 (±13.14)	86.13 (±8.97)	79.83 (±11.2)	72.24 (±14.24)	81.62 (±12.91)	69.62 (±11.66)	78.45 (±19.45)

Table 2: Root system parameters for different samples of *Chrysopogon spp.* * symbol indicates that is a root fragment.

Variable	**Samp. 10***	**Samp. 9***	**Samp. 11***	**Samp. 5***	**Samp. 6***	**Samp. 7***	**Samp. 8***
Species				*Arachis pintoi*			
Soil Dens. (kgm^{-3})	Greenhouse	Greenhouse	Greenhouse	1.0	1.0	1.30	1.0
Growth St. (days)	< 8	< 8	< 8	70	70	70	70
Fractal Dim.	1.29	1.39	1.45	1.36	1.36	1.35	1.38
Root Lgth. (mm)	3125.63	10966.21	10665.79	10473.10	10220.66	10331.63	8110.60
Net. Area (mm^2)	5709.14	15885.53	12421.53	14959.65	14171.75	14754.62	11959.16
Avg Dia. (mm)	2.52	2.02	1.53	1.91	1.88	1.88	2.00
Med Dia. (mm)	1.99	1.41	1.33	1.60	1.41	1.41	1.41
Max Dia. (mm)	11.15	9.54	7.17	7.86	7.91	7.60	9.79
Perim. (mm)	4905.65	17546.01	17969.68	16988.57	16484.74	17061.09	13197.22
Vol. (mm^3)	21671.43	51160.18	24888.82	38725.64	38072.38	37186.97	36446.10
Surf. Area (mm^2)	24563.56	68684.81	50684.66	62021.64	59463.76	60241.86	50510.98
Avg RAR (%)	8.73	8.44	4.00	13.10	9.00	13.32	7.00
Avg Orient. (°)	88 (±16.14)	55.64 (±14.26)	58.62 (±23.85)	78.16 (±11)	83.21 (±11.2)	74.75 (±11.77)	76.06 (±13.82)

Table 3: Root system parameters for different samples of *Arachis pintoi.* * symbol indicates that is a root fragment.

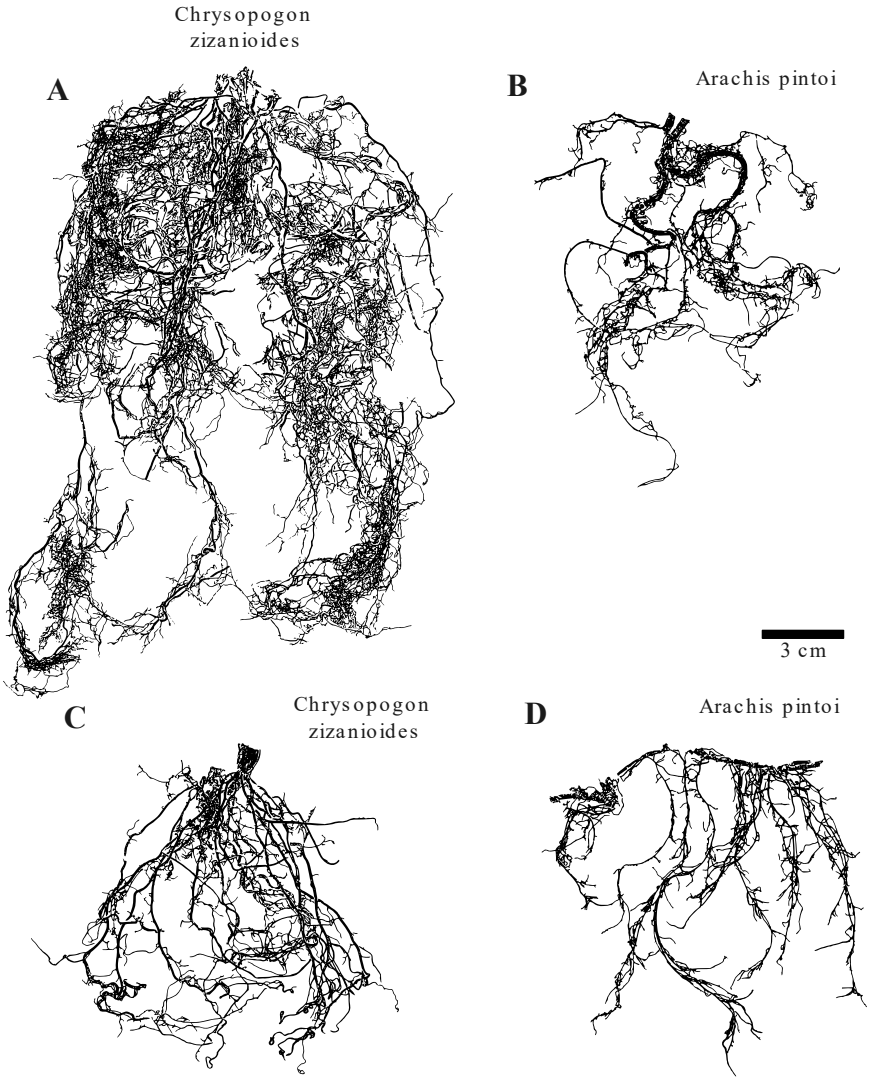

Figure 13: Visualization for root samples. A *Chrysopogon spp.* at 30.4 days growth at EAFIT, B *Arachis pintoi* received from greenhouse, C *Chrysopogon spp.* at 39 days growth at Hispania and D *Arachis pintoi* at 71 days growth.

Discussion

This investigation explores the utility of semi-automated image processing for RSA visualization and the calculation of geometric parameters. The main objective is to develop a practical workflow for visualizing the RSA of two different species under different soil density and growth stage conditions. This serves as a tool to enhance the understanding of roots while reducing the gap in vegetation parameter calculations for geotechnical and modeling applications that require specific data.

With the 2D image processing methodology, the root systems of both species were successfully mapped using the improved Frangi method, resulting in more accurate estimation of geometrical parameters. The algorithm was capable of

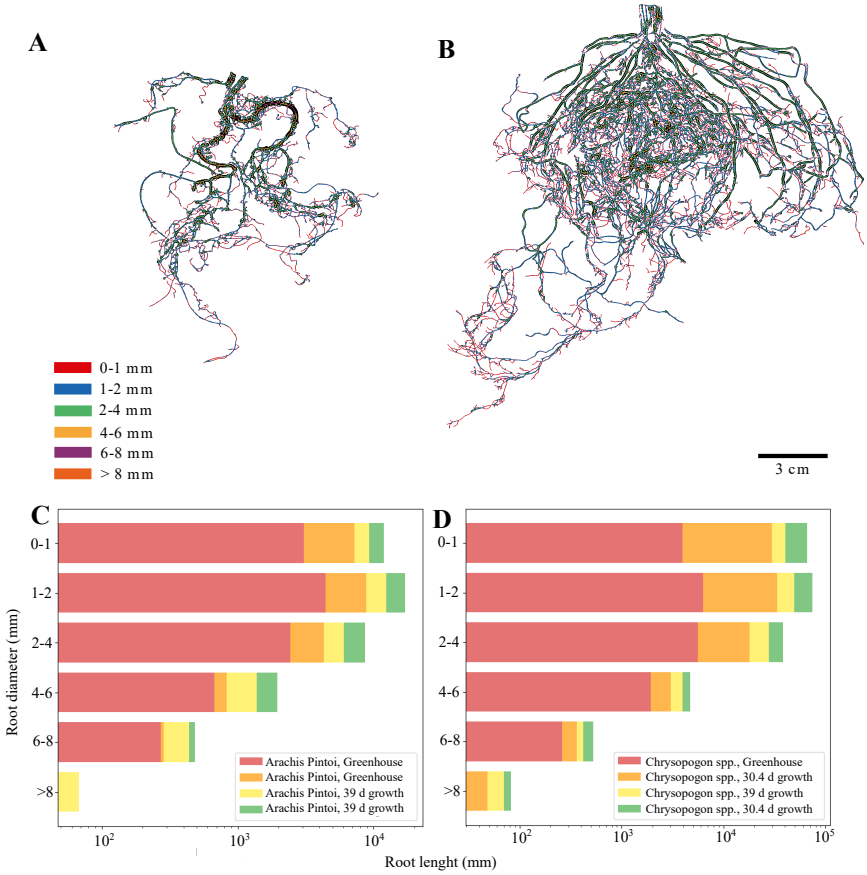

Figure 14: Average root diameter for samples. A is an example of a sample of *Arachis pintoi* visualization with the diameters classes identified by RhizoVision and B for *Chrysopogon spp.*, C is the distribution based on length for each category for 4 samples and D is the same for *Chrysopogon spp.*

mapping even the tiniest roots (below 2mm), which is a particular challenge in dense and fibrous root systems like the *Chrysopogon spp.* ones.

For this particular case, the results for root perimeter, area, average diameter, volume, fractal dimension, and RAR underscore the substantial impact of soil density and granulometric properties on RSA. In less compacted, regularly irrigated soils at EAFIT, *Chrysopogon spp.* roots exhibited notable growth, with root lengths of 62251.9 mm and 66637.1 mm, average diameters of 1.50 mm and 1.56 mm, volumes of 138948 mm^3 and 161633 mm^3, fractal dimensions of 1.60 and 1.61, and RAR values of 34.21% and 32.46%, supporting the development of a more fibrous and branched structure. Also fractal dimension and RAR were markedly higher than in denser, naturally watered soils. Fractal dimension, for example, decreased by approximately 12.2%, volume by 61.9%, surface area by 71.2%, and RAR by 55.9% in compacted soil. Conversely, the average root diameter increased by 27.8% in denser soils, likely indicating an adaptive response to compaction.

Similarly, *Arachis pintoi* grown in less compacted, regularly irrigated soils

showed enhanced RSA characteristics, with root lengths of 10473.1 mm and 8110.6 mm, average diameters of 1.91 mm and 2.00 mm, volumes of 38725.64 mm^3 and 36446.10 mm^3, fractal dimensions of 1.36 and 1.38, and RAR values of 13.10% and 7.00%, reflecting increased complexity. In contrast, the denser, rain-fed soils of Hispania restricted root development, resulting in shorter root lengths, lower volumes, and reduced RAR. Specifically, fractal dimension, volume, surface area, and RAR were reduced by 5.5%, 37.5%, 33.1%, and 23.9%, respectively, in compacted soil. Similar to *Chrysopogon spp.*, average diameter increased by 11.5% in denser soils, indicating an adaptive response.

Some investigations in wheat and tomato cultivation Rogers and Benfey (2015) reveal that heightened soil compaction results in shorter and wider roots. This leads to a shallower and narrower RSA, which restricts soil exploration by the roots. These findings are consistent with the results of this study, which demonstrate that principally soil compaction and possibly silt-clay particle size of the study area, produces roots with larger diameters and decreases branching. This can potentially affect root water uptake and other hydrological processes, especially in the superficial soil layers where root tips assist in root penetration and anchorage within the soil matrix. These preliminary results suggest that greater compaction increases soil strength but reduces root growth, potentially decreasing reinforcement efficiency; however, this needs to be confirmed through further experiments.

The analysis of RSA provides a valuable tool for more accurate parameter assignment based on root characteristics. Results suggest higher RLD typically corresponds to a more branched root architecture, which could lead to a higher fractal dimension. In compact or resource-limited soils, roots may become more intricate, increasing fractal dimension but potentially reducing RLD. In contrast, more favorable conditions may result in both higher RLD and fractal dimension. Therefore, fractal dimension could serve as a useful proxy for estimating RLD, simplifying root system analysis without the need for extensive instrumentation. In the context of climate change, relying solely on vegetation type to assess terrain stability is often insufficient for bioengineering applications. Instead, species-specific traits, ecological aspects of plant communities, and growth conditions are essential considerations. Enhanced RSA analysis provide insights not only into APS interactions but also support a range of bioengineering and agronomy applications, establishing RSA analysis as a valuable tool in environmental management.

Conclusions

Digital image processing facilitated the visualization and analysis of RSA, providing essential insights into the geometrical parameters.

In this section, soil compaction and granulometric properties significantly

influence RSA. Preliminary results suggest that greater compaction improves soil strength but limits root growth, which may reduce reinforcement efficiency and requires further validation. In less compacted soils, both Chrysopogon spp. and Arachis pintoi exhibited more extensive and branched root structures. However, in denser soils, RSA parameters showed notable reductions: fractal dimension decreased by 12.2% to 5.5%, volume by 61.9% to 37.5%, surface area by 71.2% to 33.1%, and RAR by 55.9% to 23.9%. Root diameter, however, increased by 27.8% to 11.5%, indicating an adaptive response to compaction. The relationship between RLD and fractal dimension suggests that both parameters reflect the complexity of root systems.

Vegetation, including trees and grasses, plays a vital role in slope stability through root reinforcement and hydrological effects, with applications extending to wildfire management, crop stability, and urban heat mitigation areas that require precise vegetation data.

Data-driven analysis of Soil-Atmosphere interactions

Abstract

Seasonal patterns in hydrological, mechanical, and atmospheric time series involved in geotechnical monitoring, reveal crucial spatio-temporal dynamics at the Soil-Atmosphere interface. These dynamics show how environmental variables interact under different climatic conditions, influencing soil and rock behavior. We used Continuous Wavelet and Hilbert-Huang techniques to analyze temporal and spatial information at different scales. The research analyzes atmospheric and soil-rock data across three geotechnical monitoring locations with multi location and sensor arrays: Le Fauga, La Roque-Gageac and Aburrá Valley. Coupled analyses for hydraulic, thermal, and mechanical interactions were examined.

At Le Fauga, deeper layers (50+ cm) act as moisture and heat reservoirs. Moisture response to rainfall delays of up to 70 days at annual scale and less than 2 hours in daily scale. Soil temperature is mainly influenced by yearly cycle, with only the first 20 cm layers reacting to day-night variations. Evaporation shows delays up to 121 days, reflecting seasonal temperature effect on soil moisture.

For La Roque-Gageac, heat conduction shows distinct cycles, being the annual one the most important, where between 2 and 6m a 40 days lag was detected due to heat storage, revealing heat conduction dynamics. Displacement behavior differs by depth, with strong correlations at D1 2m and 4m (Spearman 0.99) indicating block movement, while weaker coupling at 4m and 6m suggests localized deformation and fracture development. Temperature influenced displacement for at least 2m, with coherence and correlations above 0.5. A segmented-block behavior was detected, more clearly at 4-6m interface.

Finally, in the Aburrá Valley, soil moisture responds rapidly to rainfall, with recharge and discharge cycles under 4 hours. A six-month cycle linked to rainfall and climatic drivers is observed, with variability across stations due to local conditions. Bimodal behavior is driven by rainfall, but limited data restricts capturing long-term patterns, especially at larger scales.

Introduction

In the past decade, soil-atmosphere interactions has gained significant importance in geotechnical engineering and geosciences, where multiple studies have emphasized the impact of these interactions on slope stability and behavior (Bicalho et al., 2018; Elia et al., 2017). Some of the most substantial and seasonal changes take place at the soil-atmosphere (SA) interface, in the unsaturated region Blight (2013). These phenomena exchange remark the importance of understanding and modeling these interactions for geotechnical applications, however, often remains a challenge, particularly in long-term and large-scale scenarios (Bicalho et al., 2018).

Usually, two strategies are commonly used for monitoring the SA interface: experimental-field measurements through multi-sensor arrays and numerical modeling (An et al., 2018; Badakhshan et al., 2024; Oorthuis Gómez, 2022; Ruiz, 2013), with the last one defined in Appendix 1. Nevertheless, field instrumentation has emerged as a cornerstone in this field, becoming a useful tool for detecting remarkable insights with the inherent and complex spatiotemporal variability of recorded environmental variables (Carri et al., 2017). However, implementing accurate instrumentation, remains challenging, particularly for media where subtle changes in thermo-hydro-mechanical behavior require highly sensitive monitoring systems and more knowledge about the phenomena involved (Bicalho et al., 2018).

Following the data trail, data-driven techniques often provide methods for analyzing non-linear signals and decomposing them into oscillatory components of different frequencies to gain valuable insights from the series generated by field instruments (Biswas and Si, 2011; Song et al., 2019; Addou et al., 2023; Lee and Kim, 2019; Le, 2017; Xiang et al., 2016; Carmona and Poveda, 2014; Rao and Hsu, 2008). Furthermore, tools such as Continuous Wavelet Transform (CWT) and Hilbert-Huang Transform (HHT) offer capabilities to analyze spatio-temporal and frequency dynamics in soil-atmosphere interaction interface.

In this research, a data-driven analysis of historical time series at the soil–atmosphere interface was conducted at three monitoring sites in France and Colombia, selected for their contrasting climatic conditions and porous media characteristics. The main objective is to understand the main patterns, correlations and overall spatio-temporal dynamics of several environmental variables, as well as to highlight certain tools to take advantage of the data generated, strengthening the data trail that could complement the numerical ones.

Field data, combined with data analysis, represents a significant step forward in unraveling the complexity of SA interactions and dependencies and ultimately enhancing design and management of geotechnical scenarios. Although the Atmosphere-Plant–Soil system has been previously addressed, this study did not include relevant vegetation data and instead focused on atmo-

spheric and geological media. The analysis was conducted to explore complementary tools for interpreting geotechnical instrumentation in the context of APS monitoring. However, the bivariate analyses presented here represent a simplification of the inherently multivariate phenomenon.

Study cases and materials

Le Fauga

Le Fauga is located in Occitania/Midi-Pyrénées region of France, at an experimental fallow field of the French National Service of Meteorology (Figure 15 A,B). Le Fauga region has an oceanic climate. The region experiences a 3.1-month hot season with average highs above 24°C, peaking at 27°C in July. A 3.7-month cool season follows, with average highs below 13°C and a January low of 10°C. Rainfall is moderate, ranging from 61 mm in May to 35 mm in July.

This study case addresses thermo-hydraulic time series. The experimental set-up includes soil moisture and temperature probes temperature. The arrangement is displayed in Figure 15C. Moisture sensors employed were ML2 Theta-probes and thermistor probes for temperature. Atmospheric variables were monitored by a local meteorological station, including rainfall, atmospheric pressure, incoming solar and atmospheric radiation, air temperature, air relative humidity at 2 m, and wind speed and direction at 10 m. Solar radiation (R_n), air temperature (T_a), and rainfall (R) were selected for the analysis (Figure 16). The data were collected at 30 minute intervals over the years 2005 and 2007. Figure 16 shows some examples of the time-series data in the soil column.

La Roque-Gageac

La Roque-Gageac is located in the north-eastern region of the Aquitaine Basin, within the administrative boundaries of the Dordogne department (Figure 17A). The area is situated at the foot of a calcareous rock cliff along the left bank of the Dordogne River. The cliff ends at 100 m above the village (Figure 17C). Oceanic dynamics significantly influence the climate. Regionally, annual maximum temperatures vary between 27°C and 32°C, while minimum temperatures range from −10°C to −15°C, with an average annual rainfall of 855 mm (Gasc-Barbier et al., 2021).

The area is known by rockfalls due to the effects of climatic actions over several years, causing discontinuities that divide the rock massif into blocks (Gasc-Barbier et al., 2021; Virely et al., 2021). The rock cliff is equipped with joint meters (LVDT strain gauges) and extensometers (with thermal sensors) by RockTest/Télémac, which evaluate the displacement across the roof and beam

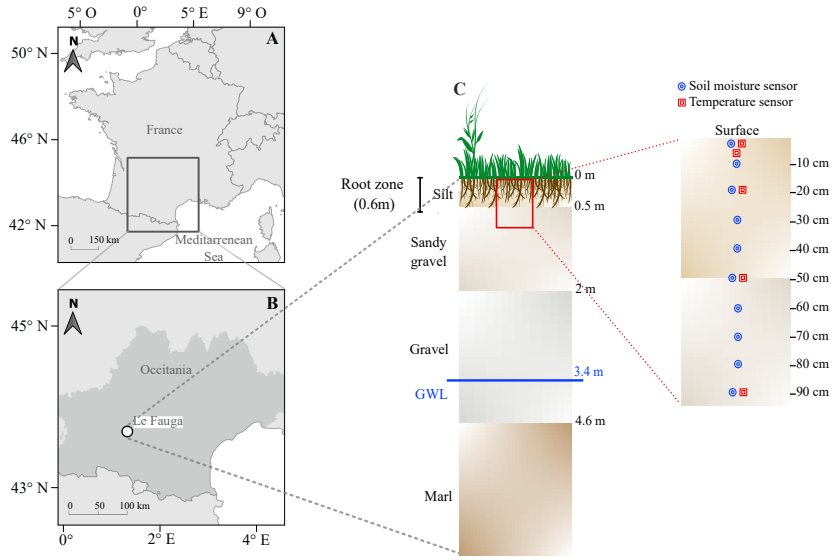

Figure 15: Localization map. A regional France map, B Occitania and Le Fauga localization and C instrumented soil column arrangement.

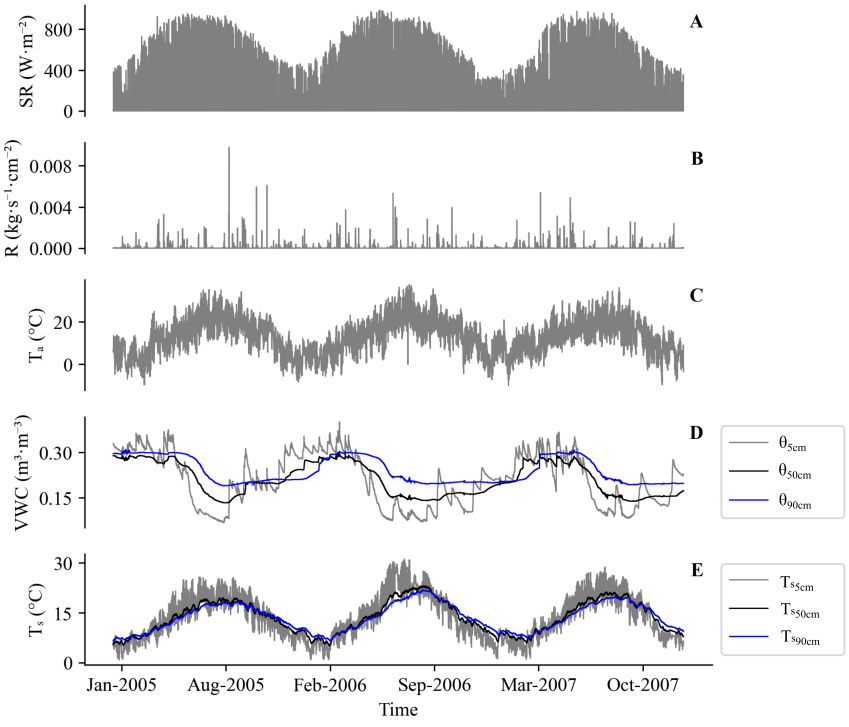

Figure 16: Le Fauga time-series. A R_n, B R, C T_a, D θ at 10, 50 and 90 cm and E T_s at 5, 50 and 90 cm.

within. The sensors, were installed in boreholes drilled horizontally from the cliff face above the cavern ($D1$ and $D2$), monitoring these displacements over time (see Figure 17C).

This study case addressed thermo-mechanical time series for the rock-cliff, including displacement data (δ) at 2, 4, and 6 m and rock temperature data (T_r) at 2 and 6 m depth. The measuring frequency had a rate of 1 hour over the years 2010 and 2017. T_a was also taken with 1-hour interval from the Sarlat-La-Canéda station, located at 10 km. Figure 18 shows the time-series for $D1$, $D2$ and T_a.

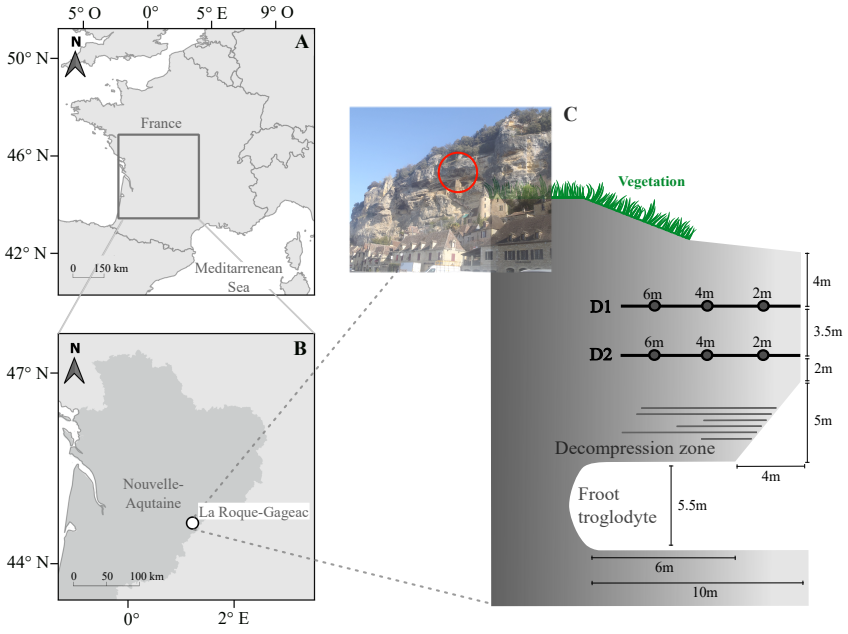

Figure 17: Localization map. A map showing France territory. Map B shows La Roque localization inside Nouvelle-Aquitaine region, and C illustrates the instrumented rock cliff, where $D1$ and $D2$ are the boreholes with extensometers at 6, 4 and 2 m and temperature sensor at 6 and 2m.

Aburrá Valley

The Aburrá Valley is located at the northern end of the Central Cordillera of the Colombian Andes (Figure 19A). It is approximately 60 km in length and is framed by irregular topography and elevation ranging between 1300 and 2800 m above sea level (Henao Casas and Monsalve, 2018). The rainfall is characterized by a bi-modal distribution, with an average annual value of 1687 mm, while the average high and low annual temperatures are 28 °C and 17 °C, respectively (Reynolds et al., 2017).

This study case addressed hydraulic time series data provided by SIATA project. The sensors Stevens Hydraprobe measured soil moisture (VWC) around some points of the metropolitan area (Figure 19B). The moisture data was complemented with local rainfall (R) data from a nearby rain gauge, also installed by SIATA (Figure 19C). Both variables were recorded with a high

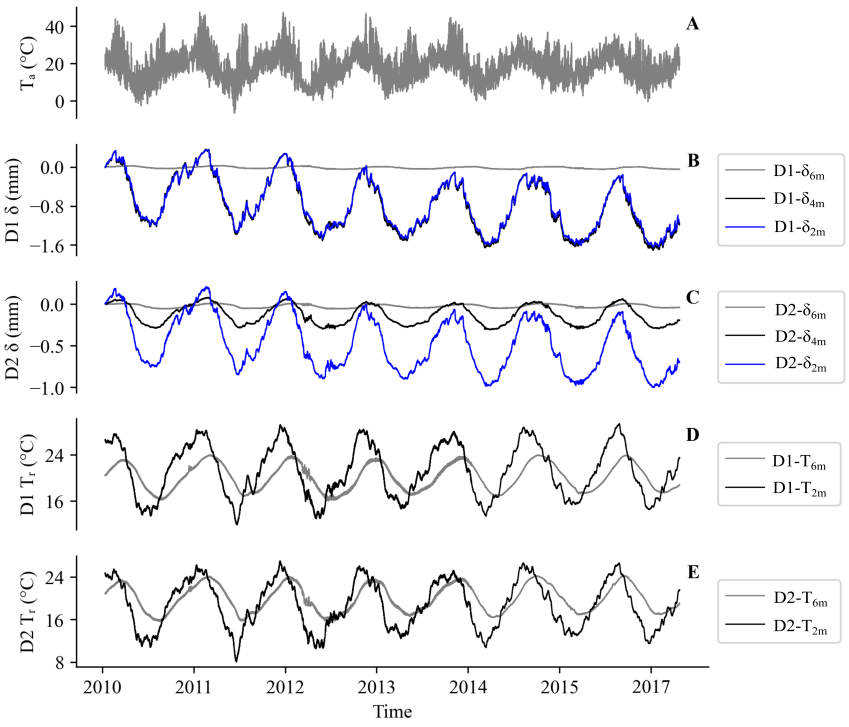

Figure 18: La Roque-Gageac time series. A is T_a, B δ in $D1$ at 6, 4 and 2 m, C δ in $D2$ at 6, 4 and 2 m, D T_r in $D1$ at 6 and 2m and E is T_r in $D2$ at 6 and 2m.

frequency rate of 1-minute for all stations and an average depth of 50 cm for all soil moisture sensors.

The time-series were resampled to 5-minute interval, reducing the computational cost and significant loss of signal information. The purpose of these sensor networks is to provide data for hydrological and geotechnical applications related to soil moisture. For 532, 613, 608 and 541 the data was selected over the years 2023 and 2024, and for 396 over 2021 and 2022. As an example, Figure 20 shows the data available in sensor 532. The information is identical for all other locations. In this study, laboratory data such as the Soil Water Characteristic Curve (SWCC) were not available, so direct validation of the volumetric water content (VWC) measurements was not possible.

Methodology

The flow chart for data-driven analysi can be divided into three major steps: 1) data preprocessing of atmospheric, soil and rock data (Figure 21 “step 1”), 2) spectral analysis of time-series using CWT and HHT (Figure 21 “step 2”) and 3) analysis of time-frequency relations for coupled and direct relations (Figure 21 “step 3”) using Wavelet Coherence and Spearman correlation.

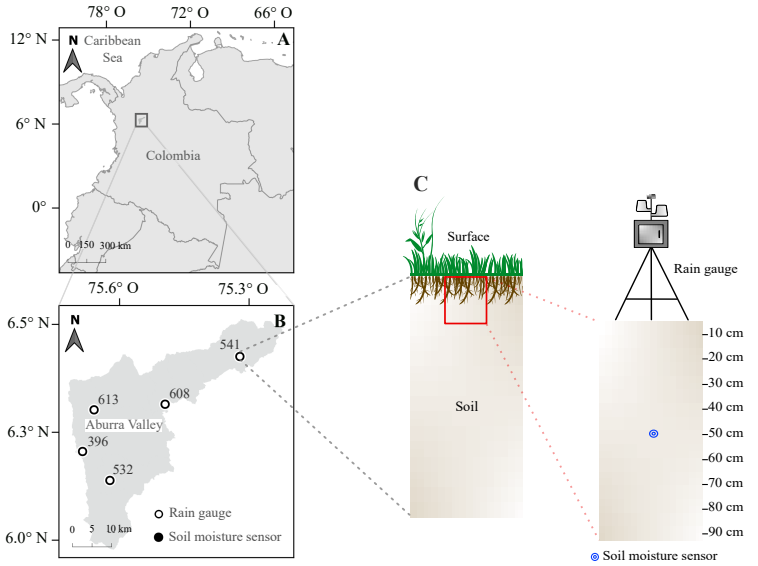

Figure 19: Localization map of Aburrá Valley. A is a map showing Colombian territory. The rectangle B zooms into Aburrá Valley and the soil moisture and rain gauge stations spatial distribution. C is the instrumented soil column arrangement.

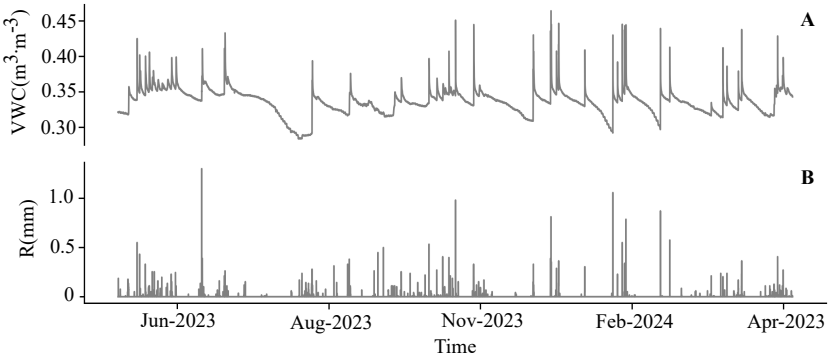

Figure 20: Aburrá Valley set of time-series. A graph of θ at 50 cm depth, and B graph is R, the gauge is located over the sensor.

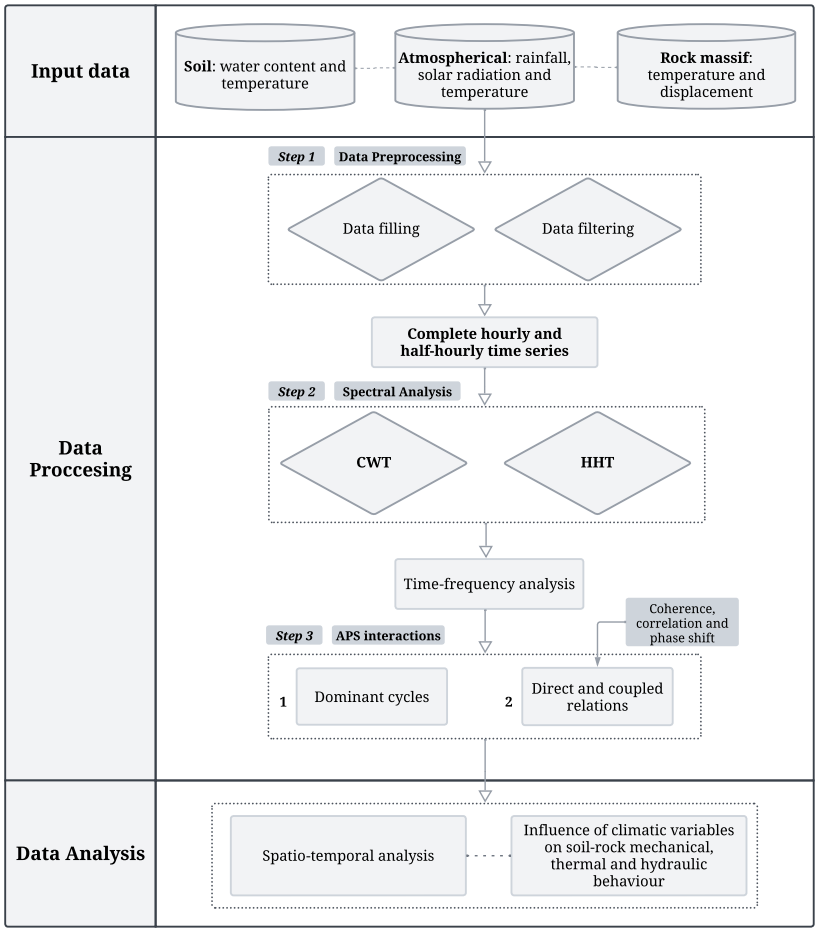

Figure 21: Flow chart of data processing and time-series analysis in Atmosphere-Soil relations.

Data prepocessing

Long-term measurements of environmental time-series datasets commonly face challenges such as missing data, noise and outliers (Corona et al., 2022). These issues arise from various factors, including power failures, sensor malfunctions, abnormal operating conditions, sensor positioning, instrument calibration, and data logger/communication problems (Corona et al., 2022; Garces and Sbarbaro, 2009; Pastorello et al., 2014). Hence, preprocessing data is essential to ensure high-quality input, which leads to reliable and accurate output analysis.

Data filling

Gaps in soil moisture, soil-air-rock temperature and displacement datasets were filled using imputeFin R-package (https://github.com/dppalomar/imputeFin) developed by Liu et al. (2019). This tool employs autoregressive models within a stochastic approximation expectation-maximization framework, coupled with Markov chain Monte Carlo procedure for data filling. The algorithm proved to be computationally efficient and easy to implement, particularly for half-hourly frequency sampled time-series with continuous missing data blocks spanning several days. ImputeFin proved effectiveness in handling missing values. For example, with a maximum squared error of 2.5, the model accurately reconstructed temperature data, aligning closely with the overall trend.

Data filtering

The Hampel identifier is a robust outlier correction method that replaces a central value with the median if its deviation exceeds a predefined threshold, as detailed in Liu et al. (2004) and Pearson (2002). Outliers are identified as data points x_j satisfying the following condition,

$$\left|x_j - x^*\right| > tS, \quad j = 1 \text{ to } N \tag{32}$$

where x^* is the median of N rank-ordered samples, S is the Median Absolute Deviation (MAD) based scale estimate calculated as shown below, and t is a scalar threshold (Allen, 2009),

$$S = 1.4286 \times \text{median}\left\{\left|x_j - x^*\right|\right\} \tag{33}$$

Factor 1.4286 in S ensures equivalence with the standard deviation for normally distributed data (Pearson, 2002). For robust location and scatter estimation, the MAD computes standard deviation, while the median estimates data location. Outliers are detected using the following criterion, where g depends on sample size and type I error (Liu et al., 2004),

$$|x - \text{median}(X_N)| \geq g(N, \alpha_N) \cdot \text{MAD}(X_N) \tag{34}$$

Additionally, a low-pass Fourier filter was employed to reduce the influence of high-frequency contributions (Blackledget, 2006), caused by instrumental noise, preserving variation with local maxima and minima. A Gaussian low-pass filter is defined as follows,

$$P(\omega) = \exp\left(-\frac{\omega^2}{2\sigma^2}\right) \tag{35}$$

defines the filter, where ω is the angular frequency, and σ is the standard deviation of the filter (its half-width when $P = \exp(-1)$) (Blackledget, 2006).

Spectral Analysis

Once the time series were corrected and completed, we carried out a spectral analysis. This analysis provided insights into the evolution and interaction of environmental time-series. Direct and coupled comparisons were carried out. This approach allowed a deeper understatement of most important seasonal frequencies and correlation involved in hydrological, thermal and mechanical processes of the media.

Continuous Wavelet Transform - CWT

A wavelet is a mathematical function used to analyze and identify over a finite spatio-temporal domain the modes of variability in stationary and non-stationary processes (Graps, 1995; Torrence and Compo, 1998). According to Biswas and Si (2011), wavelet analysis employs two fundamental tools: the integral wavelet transform and wavelet series. Wavelet series, constructed from a single function, are generated via binary dilations and integral transformations. For instance, when measuring a spatial series y_i at location x_i ($i = 1, 2, \ldots, m$) along a transect, the integral wavelet transform is defined as,

$$W(s,\tau) = \int_{-\infty}^{\infty} y(x)\psi_{s,\tau}(x)\,dx \tag{36}$$

where,

$$\psi_{s,\tau}(x) = \frac{1}{\sqrt{s}}\psi\left(\frac{x-\tau}{s}\right) \tag{37}$$

Here $\psi(x)$ is the basic wavelet and $\bar{\psi}_{s,\tau}$ is the complex conjugate. The parameter s represents the dilation-contraction factor, while τ denotes the temporal or spatial translation of the wavelet function (Biswas and Si, 2011). The CWT obtains the wavelet power spectrum of a time series, which divides the data into continuous scales and locations by interpolation, preserving all information in the original series (Biswas and Si, 2011; Wu et al., 2021). This allows insights into the temporal localization of the frequency variability of a given signal. The selected wavelet for this study, the Morlet, is presented as follows,

$$\psi_0(\eta) = \pi^{-1/4} e^{i\omega_0\eta} e^{-\frac{1}{2}\eta^2} \tag{38}$$

where ω_0 is the dimensionless frequency and η is the dimensionless time. For feature extraction purposes, Morlet (with $\omega_0 = 6$) was selected because of its balanced time and frequency localization and its robustness for environmental time series, due to the wide range of possible dominant frequencies (Addou et al., 2023; Grinsted et al., 2004; Le, 2017).

Wavelet Coherence Analysis

The relationships between the environmental data were explored through the Wavelet Coherence analysis (WCT), which provides a measure of how is the similarity across time-frequency domain (Biswas and Si, 2011; Liu et al., 2017). Based on Torrence and Webster (1999), the coherence for any two time series X and Y can be defined as,

$$R_n^2(s) = \frac{\left|S\left(s^{-1}W_{XY}(s)\right)\right|^2}{S\left(s^{-1}\left|W_X(s)\right|^2\right) \cdot S\left(s^{-1}\left|W_Y(s)\right|^2\right)} \tag{39}$$

where $W_{XY}(s)$ is the cross-wavelet spectrum, which is defined as the convolution of the wavelet transform of X ($W_X(s)$) and the complex conjugate of the wavelet transform of Y ($W_Y(s)$) (Schulte et al., 2017). S is a smoothing operator in the time-scale space. When $R_n^2(s)$ approaches 0, X and Y are unrelated; otherwise, X and Y are linearly related at the given frequency and time when $R_n^2(s)$ approaches 1 (Schulte et al., 2017).

This analysis also provides the phase shift across the time domain by defining an angle in an interval $[-\pi, \pi]$, where the angle can be expressed as a phase difference, Lee and Kim (2019) proposed the relative phase difference between the two time series can be calculated as follows,

$$\phi(s) = \tan^{-1}\left(\frac{\mathrm{Im}(S_n(s)W_{XY}(s))}{\mathrm{Re}(S_n(s)W_{XY}(s))}\right) \tag{40}$$

Here, the imaginary $\mathrm{Im}(S(f))$ and real $\mathrm{Re}(S(f))$ parts of $S(f)$ represent phase differences, indicating correlation and lag relationships. A phase difference of zero means two time series are perfectly correlated, while a difference of π indicates perfect anti-correlation (Lee and Kim, 2019).

In this study, the CWT and the WTC analysis were carried out using the Waipy toolkit implemented by Mabel Calim (https://github.com/mabelcalim/waipy).

Ensemble Empirical Mode Decomposition

Ensemble Empirical Mode Decomposition (EEMD) is an extension of a signal processing technique based on the original EMD method. This technique decomposes the signal into IMFs, where each one is associated with different oscillatory modes embedded in the original series (Carmona and Poveda, 2014). Wu and Huang (2009) proposed noise-assisted EMD algorithm, utilizing the

continuous frequency characteristics of Gaussian white noise. This method ensures continuity in the frequency domain, effectively mitigating modal aliasing. Based on Gaci (2016), the workflow of EEMD is described in Table 4.

Table 4: Steps of the EEMD Algorithm.

Step	Description
i	In the nth trial, a new time series is generated by adding a white noise series $u_n(t)$ to a given signal $x(t)$, forming $Y_n(t) = x(t) + u_n(t)$, for $n = 1, 2, \ldots, N$, with N being the ensemble number.
ii	Based on the original EMD, the noise-contaminated signal $Y_n(t)$ is decomposed into a set of IMFs and a residual as follows, $$Y_n(t) = \sum_{m=1}^{M-1} \mathrm{IMF}_m^{(n)}(t) + r_M^{(n)}(t) \quad (41)$$ where $M-1$ is the total number of IMFs resulting from each decomposition of $Y_n(t)$, $\mathrm{IMF}_m^{(n)}$ is the m-th IMF, and $r_M^{(n)}$ is the residual obtained in the nth trial. A fixed sifting number of 10 is considered to ensure an equal number of IMFs in each decomposition.
iii	Steps (i) and (ii) are repeated for N trials. In each trial, a different white noise series $u_n(t)$ is added to the original signal.
iv	The final IMF of the EEMD ($\mathrm{IMF}_{m_{\mathrm{ave}}}$) is obtained by averaging the total m IMFs related to N trials as follows, $$\mathrm{IMF}_{m_{\mathrm{ave}}} = \frac{1}{N} \sum_{n=1}^{N} \mathrm{IMF}_m^{(n)}(t) \quad (42)$$ The results achieved by the EEMD depend on the choice of the ensemble number (N) and the amplitude of added noise (A). It is shown that the following relation should be satisfied: $$\frac{A}{\sqrt{N}} \leq H$$ where H is the final standard deviation of error calculated as the difference between the original signal and the sum of the IMFs resulting from the EEMD.

For correlation analysis, Spearman Correlation Index was used to compare IMFs in all scales (Gauthier, 2001). The Spearman rank correlation coefficient ρ is defined as,

$$\rho = 1 - \frac{6 \sum d_i^2}{n(n^2 - 1)} \quad (43)$$

Where d_i is the difference between the ranks of each pair of observations and n is the number of observations. In this study the EEMD de-

composition was implemented using PyEMD developed by Laszuk (2017) (https://github.com/laszukdawid/PyEMD). Additionally, the power distribution among the IMFs was calculated, indicating the contribution of each component to the total signal power and compare the results with wavelet.

Hilbert-Huang Transform

Once the intrinsic mode function components are obtained, the Hilbert-Huang Transform (HHT) can be applied to each component to get instantaneous amplitude and frequency (Xiang et al., 2016). For an arbitrary time series $x(t)$, Rao and Hsu (2008) defined the Hilbert transform $y(t)$ as,

$$y(t) = \frac{1}{\pi} \int_{-\infty}^{\infty} \frac{x(\tau)}{t-\tau} d\tau \tag{44}$$

Where the integral is the Cauchy principal value. It is the convolution of $x(t)$ with $1/t$; hence, the transform emphasizes the local properties of $x(t)$ (Rao and Hsu, 2008). $x(t)$ and $y(t)$ form the complex conjugate pair by definition, so we can have an analytical signal, $z(t)$, as,

$$z(t) = x(t) + iy(t) = a(t)e^{i\theta(t)} \tag{45}$$

where $a(t) = \sqrt{x^2(t) + y^2(t)}$ and $\theta(t) = \arctan\left(\frac{y(t)}{x(t)}\right)$. The polar coordinate expression is the local fit of an amplitude and phase varying trigonometric function to $x(t)$ (Rao and Hsu, 2008). Based on Hilbert transform, the instantaneous frequency is defined as,

$$\omega(t) = \frac{d\phi(t)}{dt} \tag{46}$$

The Hilbert analysis was developed using SciPy library developed by Virtanen et al. (2020).

Overall Results

The CWT and the HHT and complementary tools such as WTC and Spearman were employed to identify spatio-temporal dynamics. To illustrate the methods employed, the results obtained for some atmospheric and soil variables are presented. Given the large number of data points, representative sites were selected from each location at different depths to demonstrate the variations in the frequencies of the signals embedded. It should be noted that each location was analyzed in the same way. In Appendix 3 all other spectrums for CWT and HHT, and Aburrá Valley time series are available.

Le Fauga

As an example, Figure 22 shows the CWT spectrum for some variables such as T_a, R, T_s and θ. For atmospheric variables, CWT identified 4 and 5 dominant frequencies. R_n showed frequencies at 1 year, 1 day and 12 hours. T_a had a similar behavior with 340 days, a range between 176 and 44 days and 1 day. R showed results of 195, 101, 28, 14 days and localized events of hour scale.

θ revealed two frequencies clusters: θ_{0-50cm} and $\theta_{>50cm}$. Similarly, Ts frequencies also clustered in two ranges: Ts_{0-5cm} and $Ts_{20-90cm}$. Across all series, the annual cycle demonstrated the highest power.

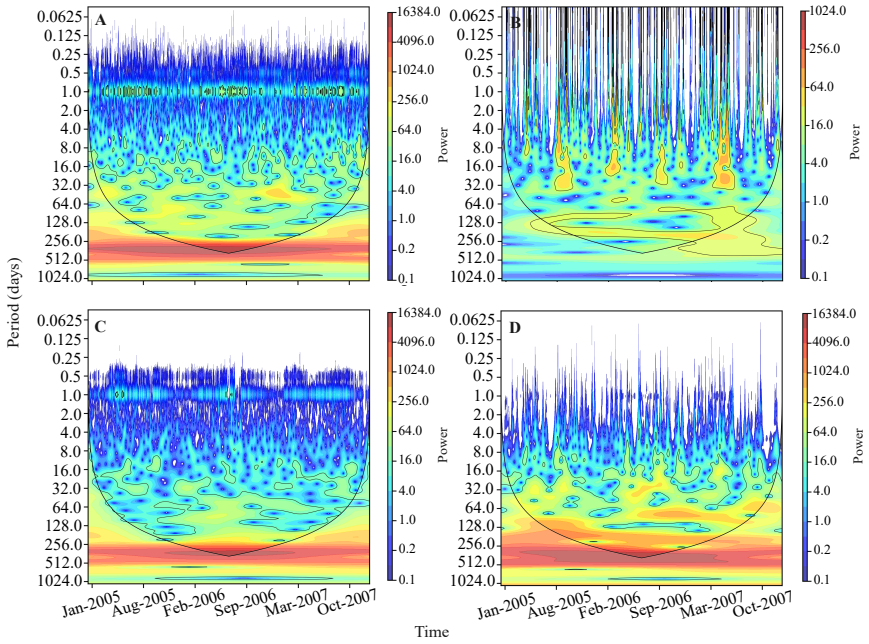

Figure 22: Continuous Wavelet Transform for Le Fauga data. A is T_a, B is R_n, C is T_s at surface and D θ at surface ($\theta_{surface}$).

Figures 23 and 24 shows the results of HHT for T_a and $\theta_{surface}$. The figures show the two IMFs with the highest power for each series. For atmospheric variables HHT identified the following frequencies: S_r showed 369 days, 1 day, 19 hours, and 10 hours; T_a had 561 days, 368 days, 13 days, and 1 day; R exhibited 1 day and 11, 4, 2.5-2 hours.

For θ, HHT revealed similar clustered frequencies as wavelet: θ_{0-50cm} and $\theta_{>50cm}$. T_s, also showed two groups: Ts_{0-5cm} and $Ts_{20-90cm}$. In Table 5 are all the frequencies identified by both methods.

The WTC and Spearman correlation were used to identify spatio-temporal dynamics for 3 couplings: Thermal (T) (comparing T_a and Ts), Hydraulic (H) (comparing R and θ) and Thermo-Hydraulic (TH) (comparing T_s and θ). In Figures 25, 26, and 27 are shown the average phase difference and coherence for each coupling.

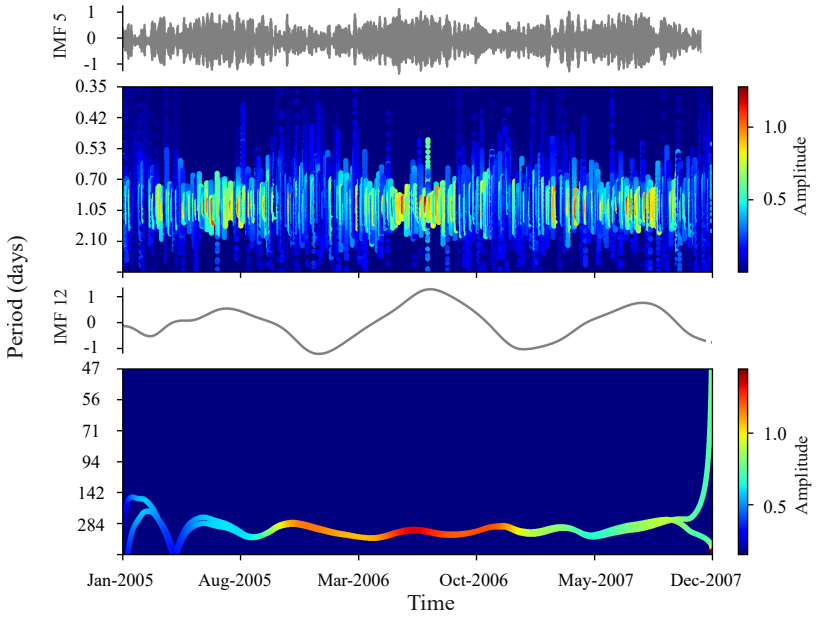

Figure 23: Hilbert-Huang Spectrum for T_a. IMFs 5 and 12 are displayed, being the two with the most power.

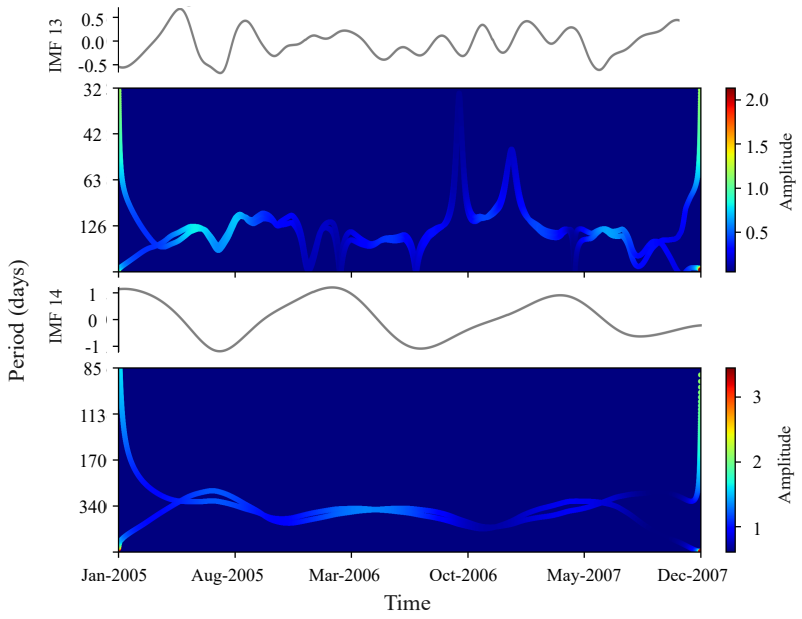

Figure 24: Hilbert-Huang Spectrum for $\theta_{surface}$. IMFs 13 and 14 are displayed, being the two with the most power.

Depth (cm)	**CWT T_s**	**CWT θ**	**HHT T_s**	**HHT θ**
$Surface$	352, 681, 202, 97, 32, 22, 14	352, 434, 195, 681, 88, 39, 9	0.88, 12, 27, 73, 369, 558, 1136	23, 52, 157, 369, 1147
5	352, 202, 681, 97, 32, 21, 14	-	0.82, 4, 10, 25, 57, 364, 1147	-
10	-	449, 365, 195, 681, 108, 38	-	19, 40, 99, 369
20	352, 681, 202	449, 365, 195, 112, 681, 32	99, 369, 1147	27, 60, 219, 369, 555, 1124
30	-	449, 365, 195, 112, 681, 32	-	49, 99, 369, 1147
40	-	449, 681, 195, 116, 38	-	25, 64, 156, 369, 1147
50	352, 681, 202	449, 681, 116, 37	364, 558	99, 369, 559, 1147
60	-	449, 365, 681, 116	-	84, 276, 369, 1147
70	-	449, 377, 681, 209	-	275, 369, 1147
80	-	449, 681, 116	-	220, 369, 1147
90	352, 681, 202	449, 681, 202	157, 369, 1147	157, 369, 558, 1147

Table 5: Le Fauga main frequencies for soil moisture and temperature.

For H coupling Figure25A, shows the phase difference. At daily scale, the first 50 cm showed similar behavior, with less than 1 hour to response to rainfall inputs. 90 cm showed values of almost 3 hours. At monthly scale, the first 10 cm showed similar synchrony, lagged less than 10 hours. 10 cm onwards the phase was similar with values of almost 3.7 days. At the six-month scale, the deepest part showed very high synchrony, while the shallowest showed a shift of almost 25 days. Reaching yearly scale, all scales dropped tho negative phase, showing values of 50 for 10 cm to 100 days for 90 cm, which quickly turn positive and lagged again.

Figure 25B, coherence varied around 0.5 on daily to monthly timescales. At 90 cm depth, it was slightly higher at 6-month scale (0.8), at this same scale, shallow depths showed low coherence (0.1). Annually, coherence started at lower values (0.38) for 50 cm downwards, but quickly increased to 0.7, while 10 cm started high (0.75) and then decreased (0.2).

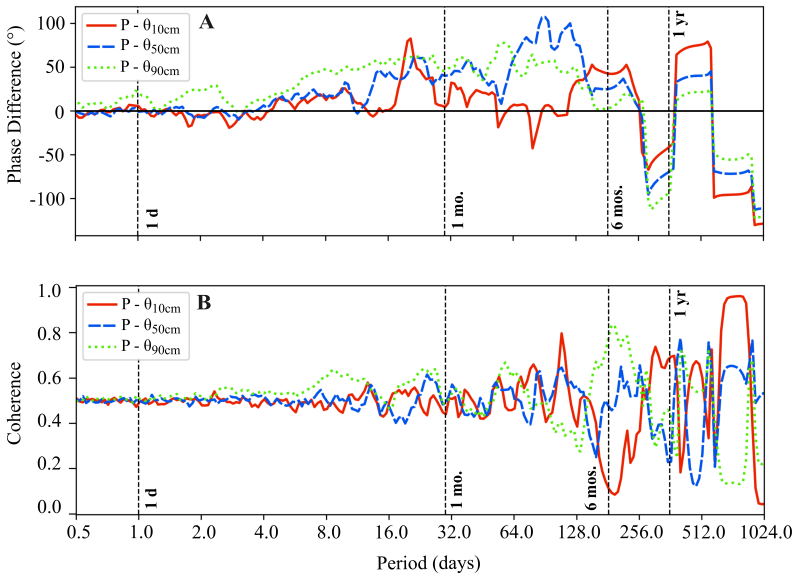

Figure 25: Average phase difference (A) and coherence (B) for Le Fauga hydraulic coupling.

T coupling phase difference is shown in Figure 26A. At daily scale, the first 10 cm showed positive phase, with less than 1.4 hours to response. 50 cm downwards, the phase was negative, lagging almost 8 hours for 50 cm and 1.5 hours for 90 cm. At monthly scale, all depths showed similar synchrony, lagged less than 2 days. At the six-month scale, similar synchrony remains but negative, where 5 cm showed the largest value with 15 days. At yearly scale, all scales showed values less than 30 days for 90 cm and very similar synchrony for 10 cm,

In Figure 26B, coherence varied around 0.5 on daily to monthly timescales. Reaching six month scale, a positive trend was clear, peaking values of 0.7. Annually, coherence showed the highest values for the first 50 cm (0.7 and 0.97), downward the coherence was about 0.42.

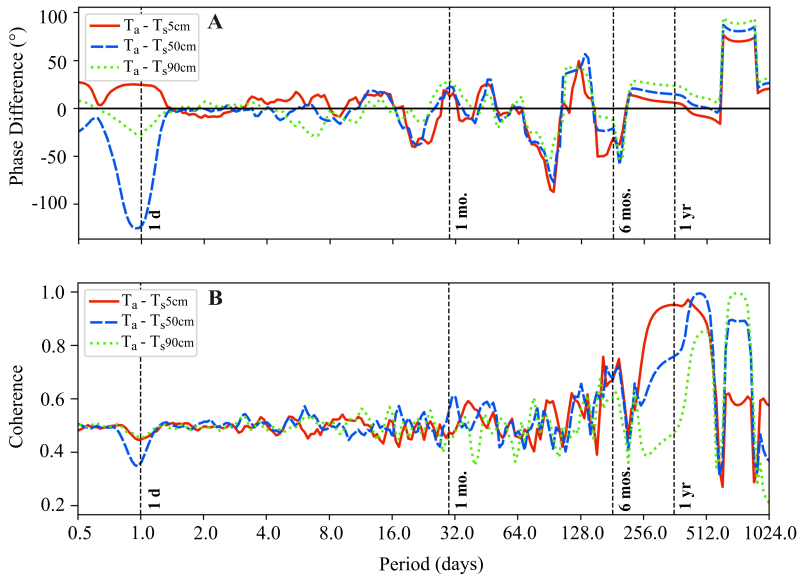

Figure 26: Average phase difference (A) and coherence (B) for Le Fauga thermal coupling.

TH coupling phase difference is shown in Figure 27A. At daily scale, the first 50 cm showed positive phase, with less than 30 minutes to response, except for 20 cm, where the lag was about 3 hours. For 90 cm, the phase was negative, lagging almost 1.3 hours. At monthly scale, 50 cm upwards lagged less than 2 days. Since the six-month scale, all depths showed synchronized negative phase less than 25 days. At yearly scale, all scales showed values around 100 and 130 days of lagging, with the smallest value at shallow.

In Figure 27B, coherence varied around 0.5 on daily to monthly timescales for all depths. At six month scale, the coherence similar to phase, start depleting to negative values, reaching a minimum of 0.22 at 50 cm. Annually, coherence showed the lowest values with only 20 cm has a value of 0.6, while all others were below 0.4.

Figure 28 presents the Spearman correlation of IMFs for each depth, aligning with the coherence analysis for T coupling. At the surface, the positive correlations (>0.45) occur at the 1-day scale (IMF 5) and between IMFs 11 and 14, corresponding to periods longer than six months, with particularly strong correlations at the annual scale (IMF 12). At 50 cm depth, the daily scale shows a negative correlation, mirroring the shifted peak seen in the coherence analysis, while the strongest correlations occur around IMF 11-12 (annual scale). At 90 cm depth, significant correlations are primarily observed also at IMF 11-12.

For H coupling, the surface displayed positives correlations (>0.35) between IMFs 7, 11, and 14, corresponding to periods longer than six months. At 50 cm depth, negative correlations were observed at the 12-month scale. At 90 cm, correlations were mainly negative, less distinct and dispersed.

For TH coupling, all depths exhibited moderate to high negative correlations (>0.35) beginning at IMF 10, with the strongest negative correlations observed

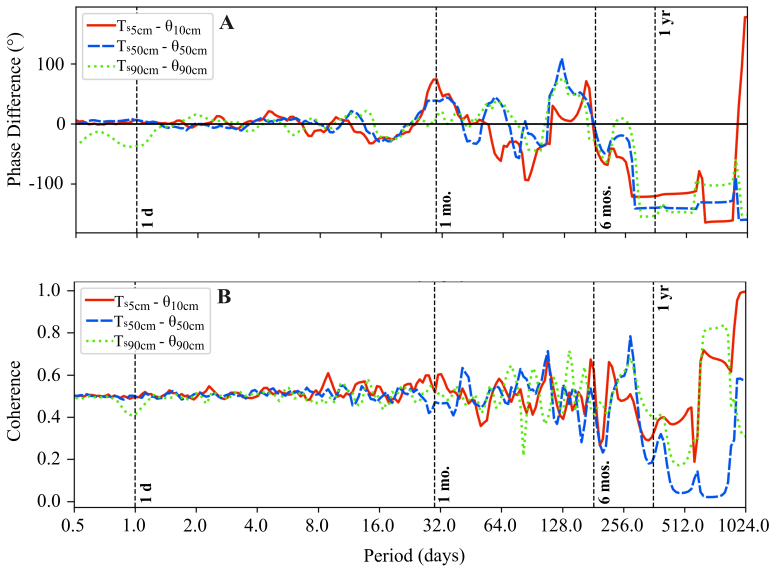

Figure 27: Average phase difference (A) and coherence (B) for Le Fauga thermo-hydraulic coupling.

at 50 cm depth. This contrasts with the low coherence noted beyond six months.

Discussion

Soil moisture at Le Fauga varies with depth and seasonal patterns. In shallow layers (0-50 cm), moisture follows three cycles: annual (1-year), seasonal (195 days), and short-term (9 days) in response to rainfall. Deeper soils (>50 cm) show only longer cycles (1-year and 209-day periods), functioning as moisture reservoirs that buffer against short-term weather changes. While surface layers react quickly to environmental conditions, deeper layers maintain more stable moisture levels.

The phase analysis revealed different moisture movement patterns across time scales. At shorter periods (up to 6 months), positive phase values indicated delayed downward water movement. At the annual scale, however, all soil depths showed a negative phase shift, meaning all layers responded 50–90 days before rainfall events. This suggests that deep soil moisture changes are driven by seasonal water storage and redistribution rather than direct rainfall infiltration.

Coherence analysis showed varying relationships between soil depths and moisture patterns. At monthly scales, moderate coherence values (~0.5) were observed, with 90 cm depth showing stronger coherence (0.8) at the 6-month scale, while surface layers (10 cm) showed weak coherence (0.1) due to atmospheric effects. Annual coherence was generally low (~0.3). IMF correlations were strongest at the surface (>0.3 at 10 cm) and became more diffuse with

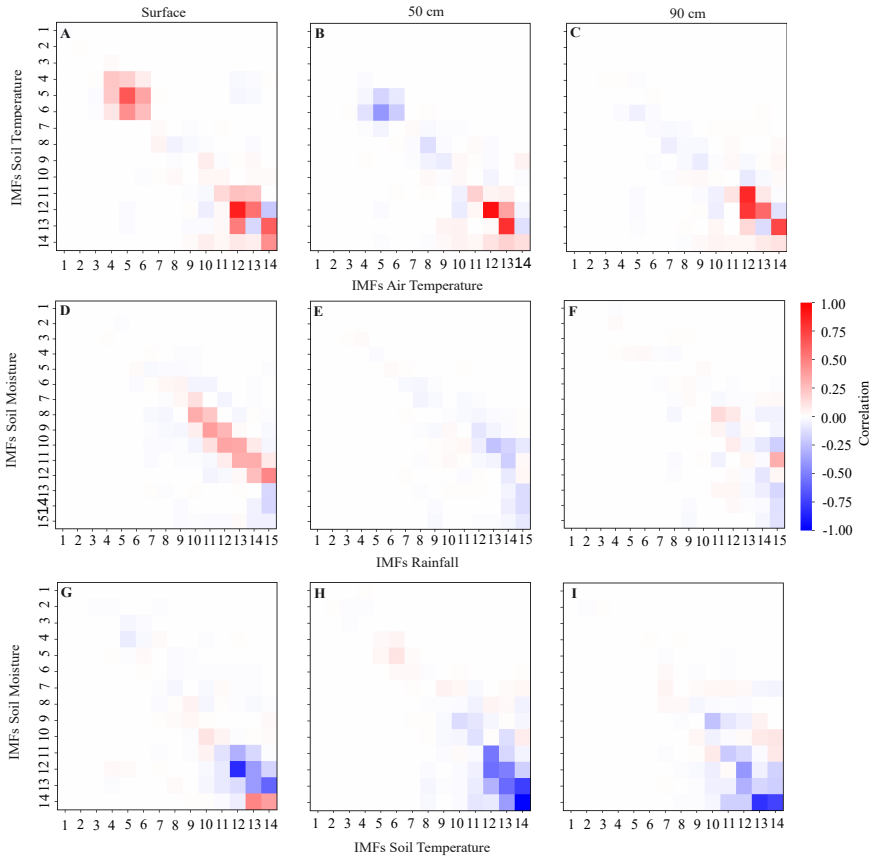

Figure 28: Spearman correlation matrix for H, T and TH couplings. A is a comparison between T_a and $Ts_{surface}$, B T_a and Ts_{50cm}, C T_a and Ts_{90cm}, D R and $\theta_{surface}$, E R and θ_{50cm}, F R and θ_{90cm}, G $Ts_{surface}$ and $\theta_{surface}$, H Ts_{50cm} and θ_{50cm} and I Ts_{90cm} and θ_{90cm}.

depth, indicating complex interactions between atmospheric drivers and soil moisture movement.

Soil temperature revealed depth-dependent patterns. Surface layers (0-5 cm) exhibited multiple cycles: annual (1-year), seasonal (352 and 202 days), and bi-weekly (14 days). In contrast, deeper soil layers (20-90 cm) showed only an annual cycle, demonstrating a more stable thermal regime with slower heat redistribution. Phase analysis showed depth-dependent time delays. At 50 cm depth, daily variations lagged by 7 hours, while at the 6-month scale, a phase shift of 8.3 days was observed. Annual variations showed near-zero phase shift, indicating synchronization with seasonal temperature changes.

Deeper soil (90 cm) exhibited slower responses, with a -30° phase shift (approximately 5 days) at the 6-month scale. Coherence analysis demonstrated strong annual coupling that decreased with depth: 0.95 at 5 cm, 0.7 at 20 cm, and 0.5 at 90 cm. IMF correlations were strongest (>0.4) for annual cycles (above IMF 10), while daily temperature fluctuations were only significant in surface layers due to diurnal variations.

The relationship between soil moisture and temperature at the same depths shows how transpiration behaves. Daily phase analysis shows inverse peaks at 20 cm (~3 hours) and 90 cm (~ 1.5 hours) depths, while monthly scales exhibit positive lags across all depths. The annual negative phase suggests seasonal temperature influences soil moisture retention, with delays up to 121 days.

Coupling between temperature and soil moisture shows low coherence (<0.5) with lags exceeding 70 days at all depths. Negative IMF correlations indicate an inverse relationship between temperature and soil moisture, reflecting in fact how transpiration behaves. Decreasing coherence over longer periods suggests weaker temperature-moisture coupling at seasonal scales.

While CWT analysis indicated that annual cycles were not statistically significant at the 95% confidence level for all variables, HHT analysis suggested these annual patterns are likely important drivers of all soil processes. This discrepancy is likely due to the dataset length limitations affecting CWT's ability to reliably detect longer periodicities, whereas HHT was better suited to identify these fundamental annual cycles.

La Roque-Gageac

Figure 29 shows the CWT spectrum for some variables such as T_a, T_r and δ. For T_a, CWT identified 7 dominant frequencies at 1362 days, 898 days, 1 year and 188, 88, 30 and 1 day. Figures 30 and 31 shows two examples of the HHT for some variables, such as $D1\delta_{6m}$ and $D1T_{6m}$. The figures show the two IMFs with the highest power for each series. HHT identified the following frequencies for T_a: 361 days, 119 days, 20 days and 1.12/1 day. For T_r and δ, the main frequencies are shown in the Table 6 for both methods.

Depth (m)	CWT $D1$	CWT $D2$	HHT $D1$	HHT $D2$
		Displacement		
6	377, 1362, 681, 129	377, 681, 1362, 124	360, 252, 2630	148, 420, 851
4	365, 1362, 91	365, 1362, 88	229, 361, 838, 1286	360, 507, 1286
2	365, 1362, 705,91	365, 1362, 705,91	360, 361, 1286	315, 360, 1271
		Temperature		
6	365, 1362, 681	365, 1362, 681	360, 507	360, 507
2	365, 1362, 88	365, 1362, 85	44, 280, 422	280, 422

Table 6: La Roque-Gageac main frequencies for rock displacement and temperature.

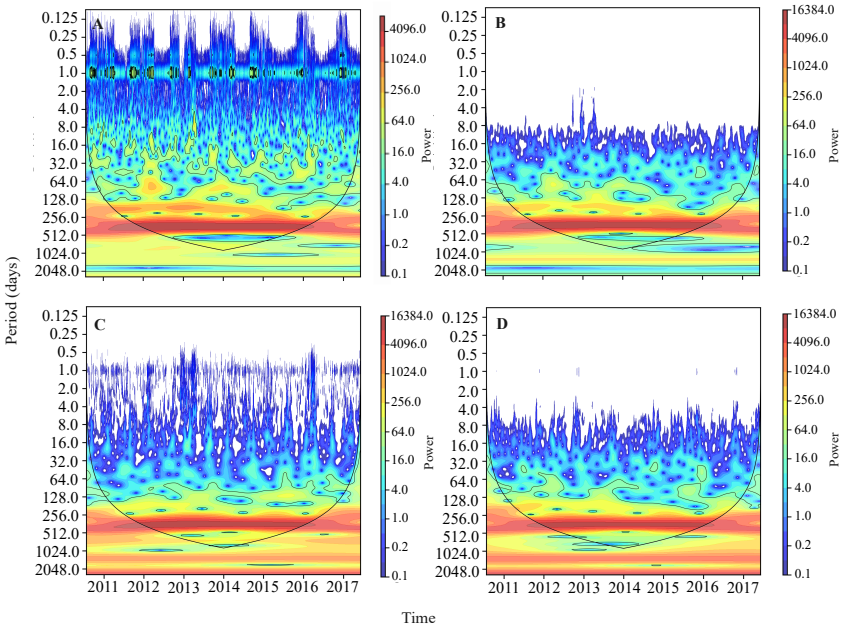

Figure 29: Continuous Wavelet Transform for Roque-Gageac data. A is T_a, B is temperature in distometer 1 at 2m ($D1\delta_{2m}$), C is displacement in distometer 1 at 6m ($D1\delta_{6m}$) and D is displacement in distometer 1 at 2m ($D1$ δ_{2m}).

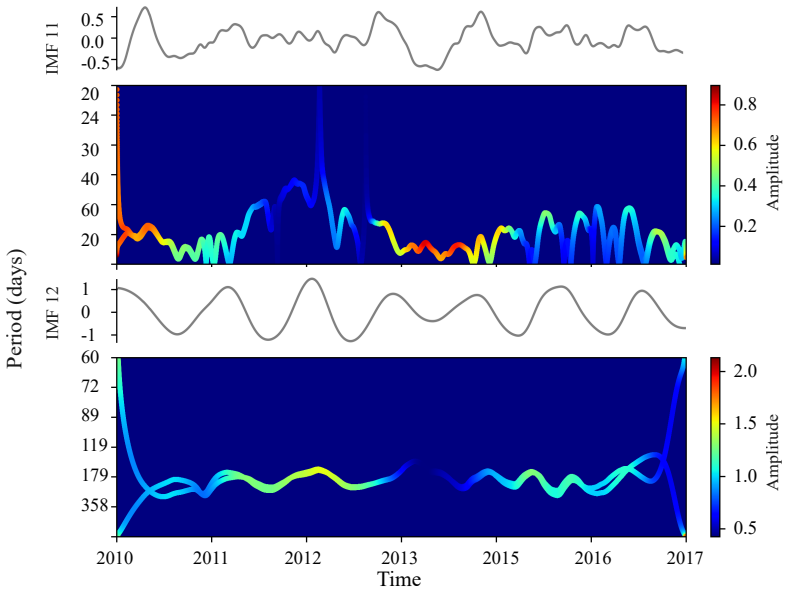

Figure 30: Hilbert-Huang Spectrum for $D1\delta_{6m}$. IMFs 11 and 12 are displayed, being the two with the most power.

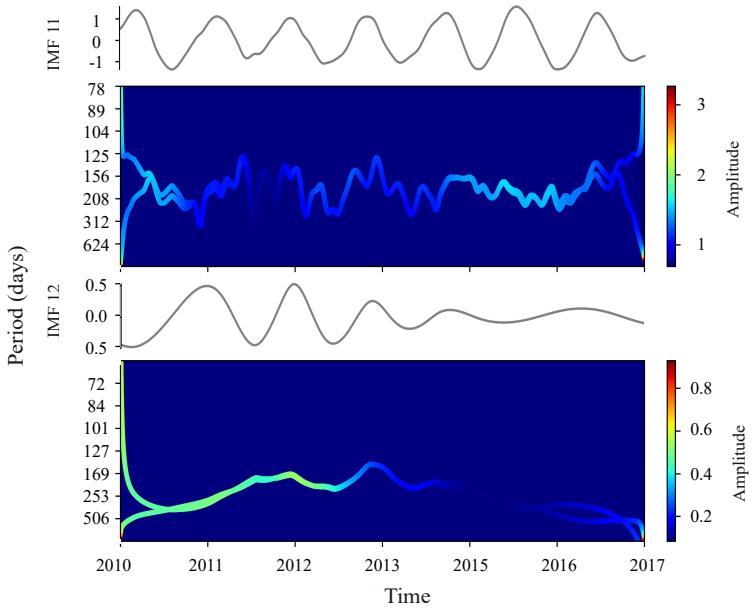

Figure 31: Hilbert-Huang Spectrum for $D1T_{6m}$. IMFs 11 and 12 are displayed, being the two with the most power.

Here the couplings were Thermal (T) (comparing T_a and T_r), Mechanical (M) (comparing δ) and Thermo-Mechanical (TM) (comparing T_r and δ). In Figures 25, 26, and 27 are shown the average phase difference and coherence for each coupling.

T coupling analysis (Figure 32A) shows that $D1$ and $D2$ behave similarly at 2m and 6m depths. At daily scale, all locations and depths showed lags less than 2.5 hours. Monthly scale showed opposite phase behavior, positive at 2m and negative at 6m, in both cases less than 7 days. At the six-month scale, $D1$ and $D2$ showed positive lagging, larger at 6m with 50–45 days and 20–19 days for 2m. At yearly scale, the lagging was about 80–70 days for 6m and 30–20 days for 2m, revealing a delay of almost 40 days.

At the 6m depth, coherence (Figure 32B) remains stable around 0.5 on a daily scale. Up to 1 month, coherence stays between 0.43 and 0.55. Between 1 and 6 months, coherence oscillates between 0.38 and 0.65, where at 2m the coherence was lower. During this period, $D2$ responds faster than $D1$. For longer timescales over 1 year, peaked at 0.8 for $D1$ while decreasing to 0.4 for $D2$ at 6m. At 2m, the coherence was above 0.45.

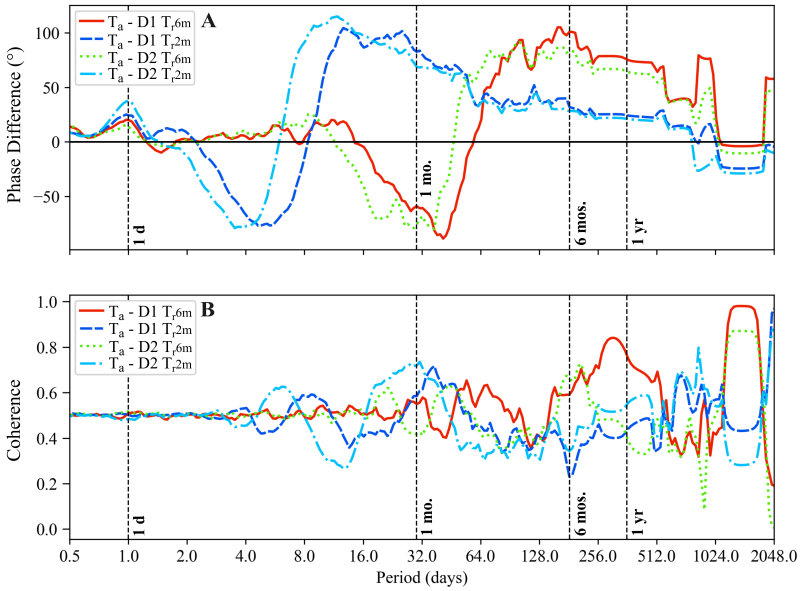

Figure 32: Average phase difference (A) and coherence (B) for La Roque-Gageac thermal coupling.

M coupling analysis (Figure 33A) shows that $D1$ and $D2$ behave in segmented blocks. At daily scale, particularly $D1$ had completed opposite phases. In this 6-4m interface at daily scale, the lag was about 3 hours, monthly 6 days, six-month 50 days and annually 60 days. At this same interface, $D2$ showed relative similarities until monthly scale, where the lag was about less than one day. At six months and annual scale lagging was about 20–40 days. At 4-2m interface the lag for $D1$ and $D2$ were similar, with variation under 9–10 days even at annual scale. Only on daily scale, a little shifted peak showed a delay of less than 2.5 hours for both cases.

Coherence, at $D1$ 4–2 m, starts at 0.57 and increases steadily to 1 at scales beyond six months. $D2$ follows a similar trend but with lower coherence at daily, monthly, six-month, and yearly scales (0.56, 0.6, 0.65, and 0.9, respectively). At 6-4m interface $D1$, maintained a value above 0.4 until annual scale, where peaked at 0.7. For $D2$ the pattern was similar, until annual scale where the coherence drops to 0.

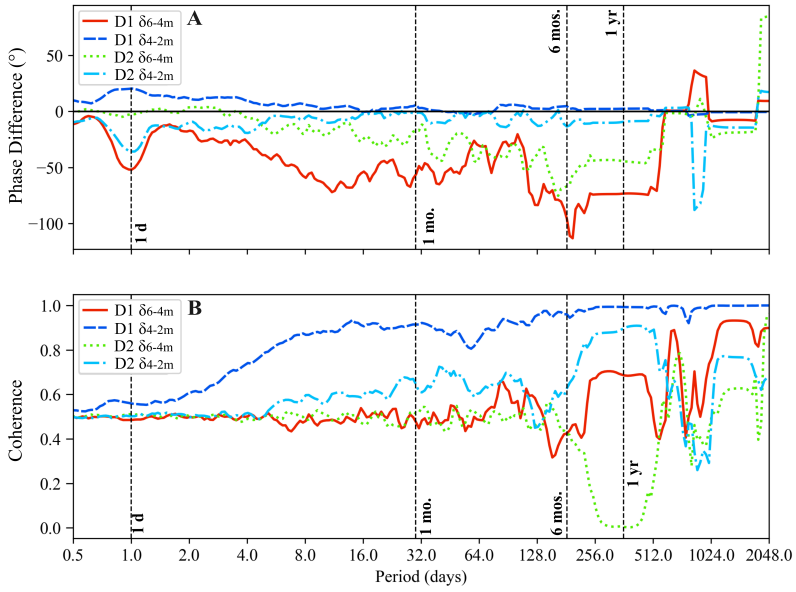

Figure 33: Average phase difference (A) and coherence (B) for La Roque-Gageac mechanical coupling.

TM coupling analysis (Figure 34A) shows that $D1$ and $D2$ behave similar in the same depths. Over 2m, at daily scale, a lag of less than 2 hours is seen. Over monthly scale, $D2$ showed good synchrony, reaching almost 0 in phase degree as well as 6 month scale. Annually, the lag for 6m meters is about 30–35 days. For 6m, a similar pattern is observed but at annual scales, it is a little bit lagged with almost 40–50 days.

Coherence, at 2m, starts at 0.55 and increases beyond monthly scale, where the highest value for both distometer are at six months (0.8) and annually (0.8 -0.58). At 6m, a relative constant value of 0.55 just before six months scale, after that the coherence depleted up to 0.2-0.28 at annually scale. Beyond annual scale, the coherence followed a similar trend for all locations until 1024 days, where a high value of 0.87 is reported for 2m interface.

In Figure 35, the Spearman correlation of IMFs is shown for each distometer. For T coupling, $D1$ and $D2$ at 2m depth exhibited negative correlations at IMFs 7-8 (corresponding to the 4-15 day scale). From IMFs 11 to 14, the correlations became positive, especially for timescales above 100 days. A similar pattern is observed at the 6m depth, with the highest positive correlations occurring at IMF 11 and beyond.

In Figure 36, the Spearman correlation of IMFs is shown for each distometer. For M coupling, $D1$ and $D2$ at 2-4m exhibited similar positive correlations

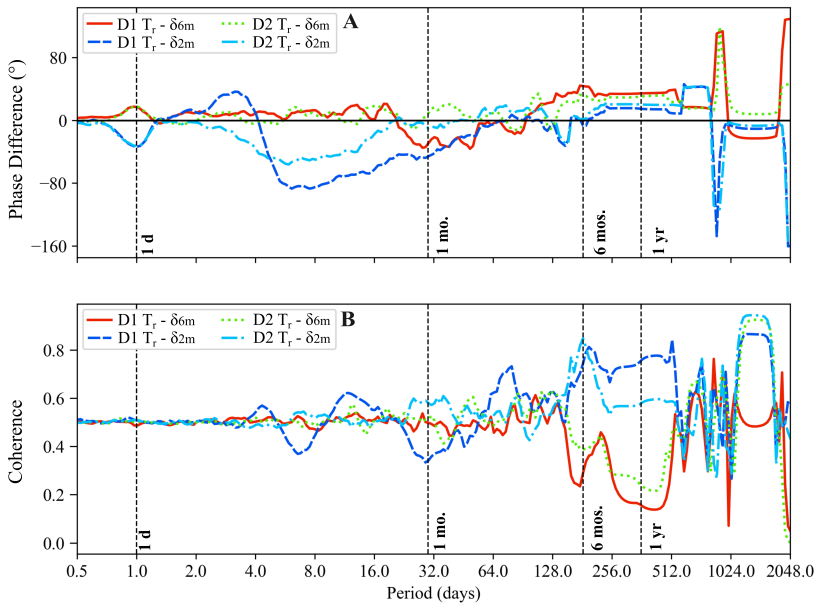

Figure 34: Average phase difference (A) and coherence (B) for La Roque-Gageac thermo-mechanical coupling.

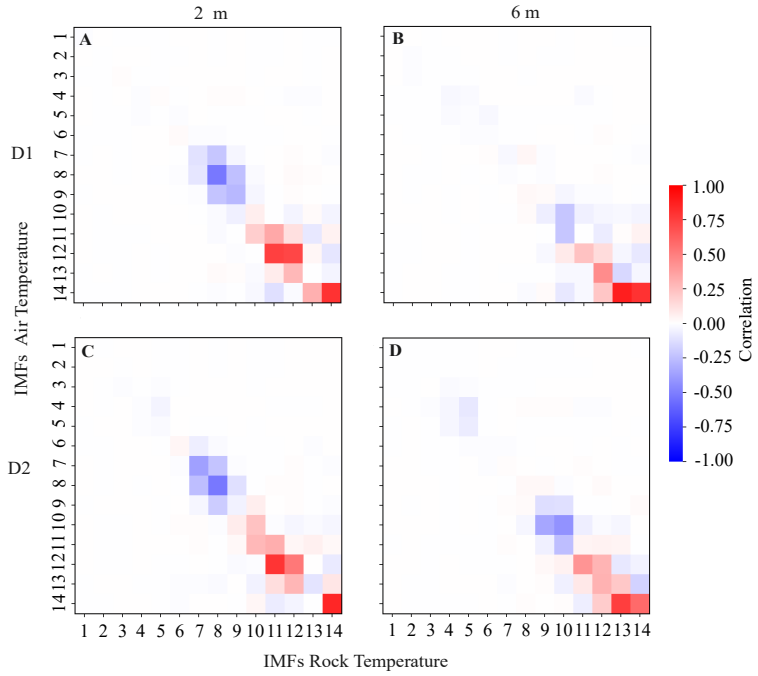

Figure 35: Spearman correlation matrix for T couplings. A is a comparison between $D1T_{2m}$ and T_a, B compares $D1T_{6m}$ and T_a, C compares $D2T_{2m}$ and T_a, and D compares $D2T_{6m}$ and T_a.

starting from IMF 4 (above 0.25), with the highest correlation observed at the yearly scale (0.7) and beyond 2 years. At 4-6m, $D1$ displayed negative correlations (below 0.15) at all timescales up to 1 year. Beyond 1 year, the correlation became positive (above 0.25). In $D2$, only positive correlations were observed, but only at timescales beyond 1 year.

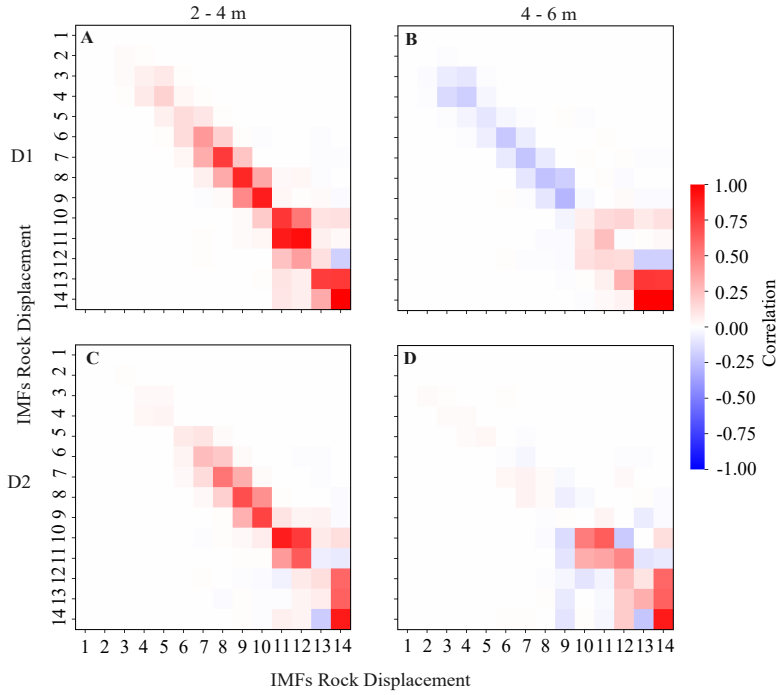

Figure 36: Spearman correlation matrix for M couplings. A is a comparison between $D1\delta_{2m}$ and $D1\delta_{4m}$, B compares $D1\delta_{4m}$ and $D1\delta_{6m}$, C compares $D2\delta_{2m}$ and $D2\delta_{4m}$, and D compares $D2\delta_{4m}$ and $D2\delta_{6m}$.

Figure 37, the Spearman correlation of IMFs is shown for each distometer. For TM coupling, $D1$ and $D2$ at 2m depth exhibited positive correlations at IMFs 9-10 and 10-12, corresponding to timescales of around 100 days and the yearly scale. Beyond the yearly scale, the correlations became negative (down to -0.4 or greater). At 6m, correlations remained positive, particularly for timescales above 100 days, but turned negative beyond the yearly scale.

Discussion

Heat conduction in rock massif is primarily controlled by the rock thermal conductivity and heat capacity, which influence how heat is transmitted and stored. At 2m, cycles with frequencies of 1 to 3 months are present as well the yearly influence, while at 6 meters, temperature behavior is primarily influenced mainly by annual frequencies, with less influence of inter annual cycles.

At 2m, the temperature of the rock lags the air temperature by ~7 days on a monthly scale, whereas at 6 meters, indicates a 6-day lead leading by the rock compared to air temperature, likely due to stored heat release. In annual scales,

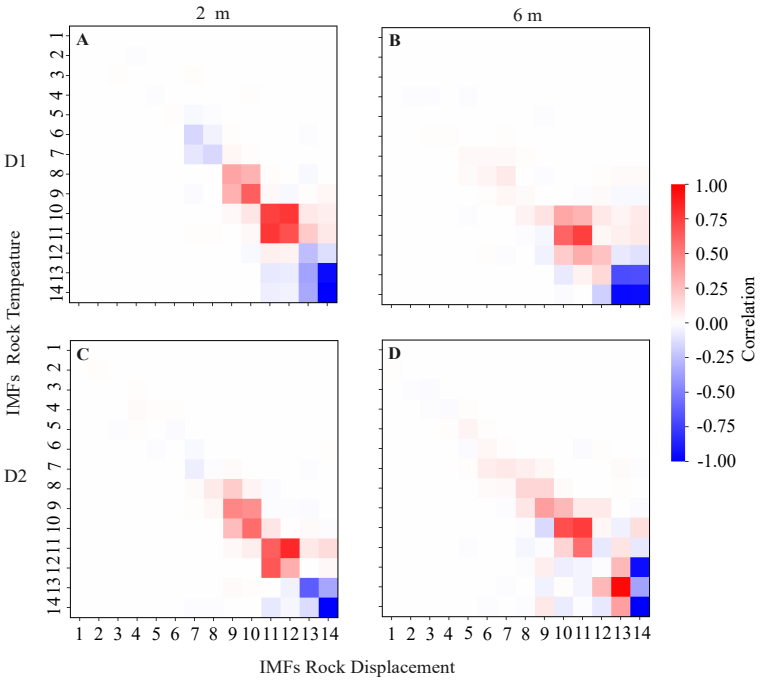

Figure 37: Spearman correlation matrix for TM couplings. A is a comparison between $D1\delta_{2m}$ and $D1T_{2m}$, B compares $D1\delta_{6m}$ and $D1T_{6m}$, C compares $D2\delta_{2m}$ and $D2T_{2m}$, and D compares $D2\delta_{6m}$ and $D2T_{6m}$.

both depths exhibit positive phases, with 6 meters lagging more significantly behind surface temperature, 6m depth is around 70 days, while at 2m is 30 days. This difference reveals 40 days lag of heat conduction between 6m a 2m positions.

Beyond 1 year, the phase for both depths approaches zero, indicating increased synchronization with air temperature, followed by a peak phase increase at 1024 days before gradually returning to near-zero, reflecting long-term stabilization of thermal responses. This contrast highlights differing thermal dynamics, where deeper layers are influenced by long-term heat storage, while shallower layers respond more directly to surface conditions.

Similarly, IMFs correlation showed increasing values over 0.3 at scales equal and above one year, showing the thermal stabilization and synchronization of the rock to atmospheric thermal cycles. By other, at daily scale, coherence was around 0.5 for all locations. On monthly scales, coherence remains in a range of 0.4-0.7. By the annual scale, coherence increases to 0.4-0.8, reflecting the influence of seasonal air temperature cycles. Since monthly scale, the influence of seasonal air temperature changes are the main influence on the rock massif heat behavior.

The displacement amplitude in the series is larger in the negative values, indicating stronger contractions. The primary frequencies were at intra-annual scale, with the yearly cycle being the most significant, followed by longer-term cycles such as 1.5 to 2.1 years. For $D1$ and $D2$ at 2m and 4m, the CWT also identified 3-month cycles.

In $D1$, displacement at 2m and 4m shows a correlation of 0.99, indicating single-block movement. Phase analysis oscillates near zero, suggesting synchronized motion despite minor static differences. Coherence supports this, with values exceeding 0.8 from the monthly scale onward. In $D2$, a similar pattern appears, with a shifted peak at daily and 2.8-year scales. This suggests rapid deformation transmission from 4m to 2m. Coherence is slightly lower, peaking at 0.9 annually before decreasing.

At the 4-6m interface, $D1$ showed larger phase differences, with delays of approximately 4.2 days (monthly), 50 days (six-month), and 60.8 days (yearly), reflecting slower deformation transmission at greater depths. Coherence for $D1$ increases steadily at the yearly scale (0.7), continuing this trend, also suggesting a lagged block movement. In contrast, for $D2$, coherence decreases nearly to zero at the yearly scale, indicating a weakening coupling at these depths over longer timescales, showing a different behavior.

The decreasing coherence in $D2$ at the yearly scale likely reflects complex deformation dynamics near the decompression zone, including fractures and localized stress changes. In contrast, $D1$, located in a more stable zone at the top of the cliff, shows consistent displacement and higher coherence. IMF correlation indicates synchronization at 2-4m for $D1$ across all scales (values >0.4) and highlights differences at the 4-6m interface for $D1$ and $D2$.

For the coupling between temperature and displacement, at 2m, the phase difference effectively suggests that temperature affects displacement. At six-month and yearly scale, a delay around 10 and 20 days, indicates a slight lag in response of displacement due to the temperature changes. In general, coherence consistently remained above 0.5. Correlation matrices also showed correlations above 0.3 at these scales, with inverse correlations at the largest showing up the lagged behavior.

By the other side, at 6m, the phase showed slightly great values of lagging of 30–40 days, at the six-month and yearly scales. Although coherence showed a descending trend, where the values gradually decreased to 0.2 at yearly scale, before increasing again beyond that scale. This indicates that the relation of temperature and displacement at this depth is not strong as in 2m, and the minor displacement pattern may have another influence. IMFs correlation also suggests this pattern due to the negative correlations (0.5) at scales greater than 6 months.

This confirms that, displacements are related to the change of temperature, at least in the first 2m. The coherence analysis led us to think that temperature variations play a role in crack propagation and possible failures. Also, the rock massif is behaving in blocks, particularly more differentiated at 4-6m interface. Gasc-Barbier et al. (2021) pointed out that the data collected at La Roque-Gageac are in possibility influenced by skin phenomena on the surface, leading to the propagation of cracks due to thermal fatigue, but the mechanism of failure of the large blocks certainly involves some sizable fractures as those due to paleo-karst.

Aburrá Valley

Figure 38 shows the CWT spectrum for variables R and θ. Additionally, in Figures 39 and 40 are the HHT spectra for station 608 as an example. θ in CWT shows cycles of 20–30, 50–70, and 200–300 days, while HHT ranges from 5–10, 20–30, 50–60, 100–150, and 300–450 days. R has CWT cycles of 0.16–37 days and ~ 170 days, with HHT concentrated in 0.09–0.99 days In Table 7 are the main frequencies identified in each station for rainfall and soil moisture data with CWT and HHT.

Station	**CWT** R	**CWT** θ	**HHT** R	**HHT** θ
396	NA	258, 681, 64, 148, 24, 13, 7.79	0.29, 0.33, 0.39, 0.49, 0.63	6.70, 12, 25, 56, 147, 374, 761
532	0.18	170, 54, 30, 340, 4.96	0.41, 0.47, 0.53, 0.62, 0.79	2.90, 6, 9, 22, 51, 119, 374
541	NA	224, 340, 108, 56, 79, 27, 8.95	0.09, 0.12, 0.19, 0.30, 0.47	23, 47, 108, 217, 446
608	37, 0.16	217, 340, 82, 41, 23	0.09, 0.12, 0.19, 0.31, 0.52	19, 28, 61, 144, 446
613	170	176, 340, 54, 24	0.51, 0.56, 0.64, 0.75, 0.99	120, 181, 372, 180, 370

Table 7: Aburrá Valley main frequencies for rainfall and soil moisture.

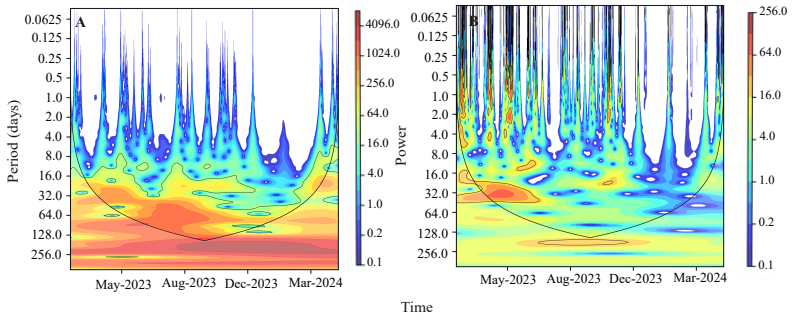

Figure 38: Continuous Wavelet Transform for Aburrá Valley data in sensor 638. A is θ_{50cm} and B is R.

The H coupling analysis (Figure 41A) reveals rainfall as a main driver in soil moisture dynamic. On daily scale the lags are similar for all station, with 1.6 to 2.5 hours except 396 where is almost 3.3 hours. Over monthly scale all station clustered in similar lagging over 3–4 days and at six months stations 396 and

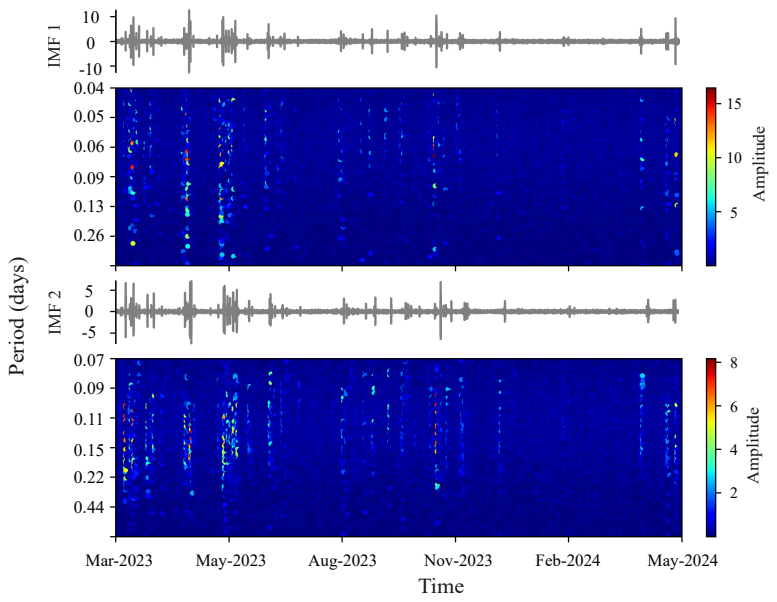

Figure 39: Hilbert-Huang Spectrum for 608 R. IMFs 1 and 2 are displayed, being the two with the most power.

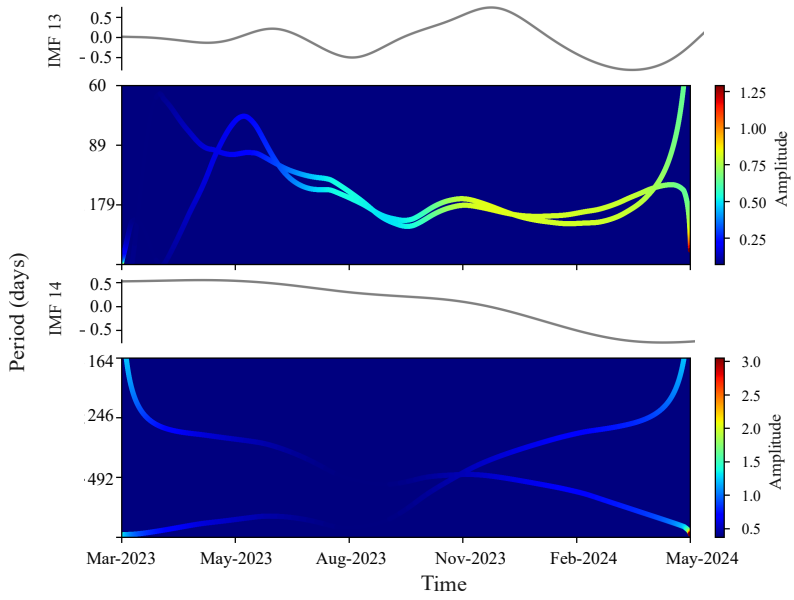

Figure 40: Hilbert-Huang Spectrum for 608 θ_{50cm}. IMFs 13 and 14 are displayed, being the two with the most power.

608 showed high synchrony reaching up to 5 days, meanwhile all others were up to 20–25 days.

From monthly to six-month scale, the coherence pattern became more diffuse, depleting just before 6 months to values below 0.2. At 6-month scale, coherence was above 0.4 for stations 396, 608 and 613, while 532 and 541 exhibited the lowest values at this point, almost 0. The phase showed a decrease from 64 to 128 days.

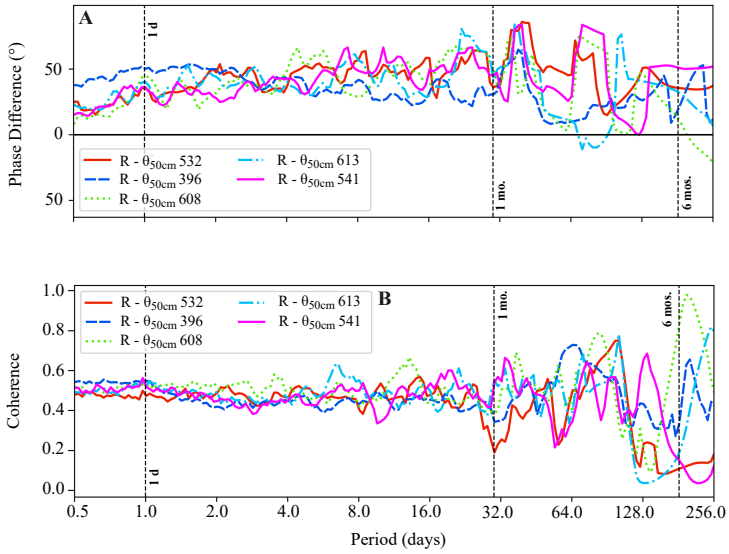

Figure 41: Average phase difference (A) and coherence (B) for Aburrá Valley hydraulic coupling.

From correlation analysis, the results showed a pattern similar to coherence (Figure 42B). The main relation emerged above IMF 9 (3 months), with patterns below this being weaker (values below 0.25). Station 608 exhibited the strongest correlation at six-month and larger scales. In contrast, stations 532, 541, and 613 showed weaker relations and negative correlations. Station 396 showed a more consistent pattern with slightly higher values at larger scales.

Discussion

Temporal variability in soil moisture arises primarily from seasonality, with certain factors like rainfall playing a dominant role. Spatial variability, on the other hand, is linked to the site-specific characteristics of the atmosphere-soil interface. The topsoil layer, being more responsive to atmospheric fluctuations and vegetation water uptake, shows a pronounced reaction to wet-dry cycles after rainfall events.

HHT outperformed CWT in extracting more detailed information with the limited data, particularly in identifying lower-frequency trends in soil moisture and rainfall data. Despite their strengths, both methods exhibited limitations in

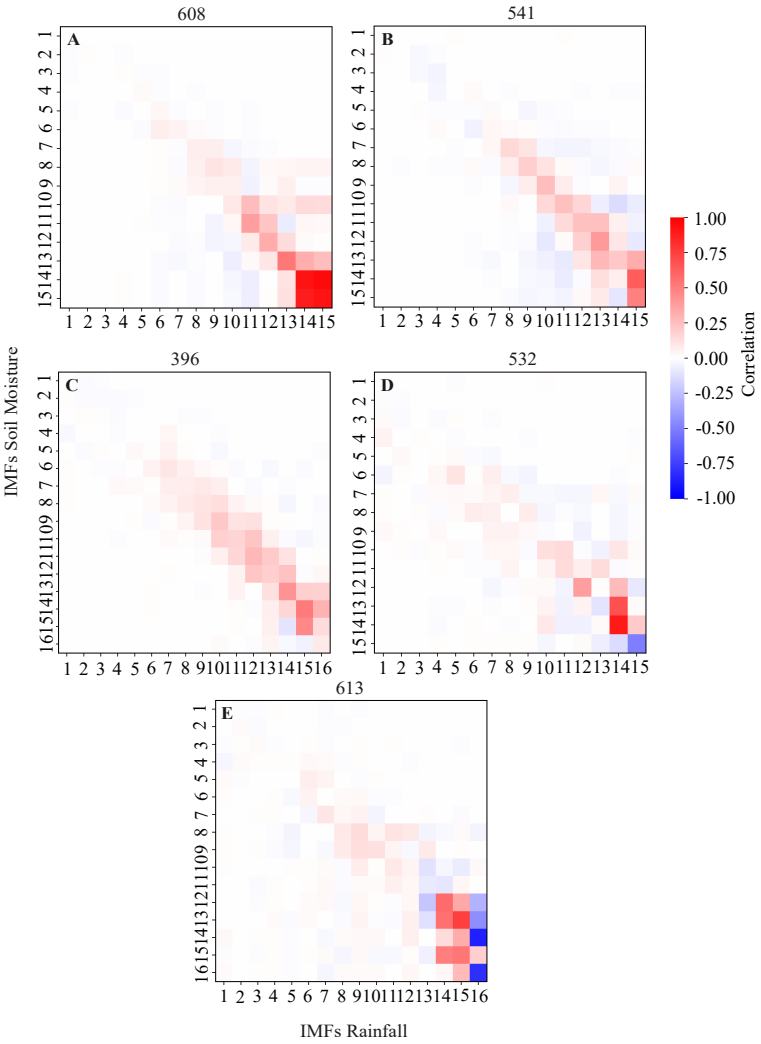

Figure 42: Spearman correlation matrix for H couplings. A is a comparison in station 608 between P and θ_{50cm}, B compares in station 541 P and θ_{50cm}, C compares in station 396 P and θ_{50cm}, and D compares in station 532 P and θ_{50cm} and E compares in station 613 P and θ_{50cm}.

capturing long-term patterns, particularly in rainfall constrained by the temporal extent of available soil moisture data.

Soil moisture displayed a strong six-month cycle, strongly correlated with rainfall patterns and the larger climatic drivers, such as the Intertropical Convergence Zone (ITCZ). Coherence analysis between rainfall and soil moisture revealed that on daily and monthly scales, soil moisture exhibited an average coherence of 0.5, indicating a moderate lagged response to rainfall with values of 1.5 to 4 hours. At the daily scale, Station 396 displayed the longest lag, attributed to local infiltration conditions. At monthly scale, all stations showed values above 0.2, with the lowest value reported at station 532.

At a six-month scale, stations 608, 396, and 613 showed positive coherence trend with values above 0.25, while stations 532 and 541 exhibited a decline in coherence reaching zero, suggesting that other hydrological factors besides rainfall may play a significant role in governing soil moisture dynamics at these sites. Despite these complexities, a bimodal behavior in soil moisture was observed, driven largely by rainfall at larger time scales.

A key limitation of the study is the short soil moisture time series, which restricted rainfall analysis and was affected by edge effects, particularly at six-month scales. These effects, highlighted by the Cone of Influence (COI), distort wavelet power in non-cyclic data, reducing reliability. In cyclic data, the COI does not apply as data wraps naturally, avoiding edge distortions. The current dataset limits deeper insights into rainfall-soil moisture interactions. Similarly, HHT identifies larger scales but with low power, except for station 396, where a clearer six-month pattern emerged with nearly two years of data. Also, a single sensor per soil column captured only part of the infiltration dynamics; additional sensors, including at greater depths, would enhance the understanding of vertical moisture redistribution.

Conclusions

The soil moisture and temperature at Le Fauga are interconnected and vary by depth. Shallow layers respond quickly to rainfall and air temperature until 50cm, while deeper layers over 50 cm act as long-term reservoirs, gradually releasing moisture and heat. This creates delayed responses in deeper layers, driven by accumulated resources. There is an inverse relationship between moisture and temperature was clear, with moisture decreasing as temperatures rise, all depths showed that water during colder-hot seasons was lagging for almost three months and release o accumulated it before temperature rises or drops. Together, these dynamics stabilize the soil system against seasonal and short-term changes.

Thermal and displacement behavior at La Roque-Gageac shows a strong interaction between temperature cycles and rock massif dynamics as contrac-

tions and extensions. Heat conduction varies by depth, with only shallow layers responding to intra-annual air temperature changes, while deeper layers exhibit delayed heat release due to long-term storage and more related to inter-annual scales. Coherence and phase analyses confirm that temperature-induced displacement are significant at least for the first 2m, particularly at monthly and annual scales, where deeper layers might have another influences. Thermal cycles play a key role in crack propagation, suggesting a link to potential block failure mechanisms in the rock mass.

Soil moisture dynamics in the Aburrá Valley highlights the complex interaction between rainfall and environmental factors, showing both temporal and spatial variability. Temporally, soil moisture is strongly influenced by seasonal rainfall patterns, with quick responses to precipitation occurring within days. Spatially, the heterogeneity across the valley, due to factors like soil properties, vegetation, and topography causes variability in moisture retention and response. Signal analysis using CWT and HHT revealed a six-month inter-annual cycle linked to larger climatic drivers, but limitations in data length restricted the capture of long-term trends, particularly in rainfall. Despite these challenges, the study identified the critical role of local infiltration and hydrological factors in shaping soil moisture behavior in this tropical region.

Bibliography

Addou, R., Hanchane, M., Krakauer, N. Y., Kessabi, R., Obda, K., Souab, M., and Achir, I. E. (2023). Wavelet Analysis for Studying Rainfall Variability and Regionalizing Data: An Applied Study of the Moulouya Watershed in Morocco. *Applied Sciences*, 13(6):3841.

Ahmadi, S. H., Sepaskhah, A. R., Andersen, M. N., Plauborg, F., Jensen, C. R., and Hansen, S. (2014). Modeling root length density of field grown potatoes under different irrigation strategies and soil textures using artificial neural networks. *Field Crops Research*, 162:99–107.

Allen, D. P. (2009). A frequency domain Hampel filter for blind rejection of sinusoidal interference from electromyograms. *Journal of Neuroscience Methods*, 177(2):303–310.

Allen, R., Smith, M., Perrier, A., and Pereira, L. (1994). An update for the definition of reference evapotranspiration. *ICID bulletin*, 43(2):1–34.

An, N., Hemmati, S., Cui, Y. J., and Tang, A.-M. (2018). Numerical investigation of soil-atmosphere interaction in an experimental embankment. In *International Society for Soil Mechanics and Geotechnical Engineering*.

Badakhshan, E., Vaunat, J., and Veylon, G. (2024). Meteorological and vegetation effects on the thermal analysis of slopes. *Renewable and Sustainable Energy Reviews*, 196:114352.

Bicalho, K. V., Boussafir, Y., and Cui, Y.-J. (2018). Performance of an instrumented embankment constructed with lime-treated silty clay during four-years in the northeast of france. *Transportation Geotechnics*.

Biswas, A. and Si, B. C. (2011). Application of Continuous Wavelet Transform in Examining Soil Spatial Variation: A Review. *Mathematical Geosciences*, 43(3):379–396.

Blackledget, J. M. (2006). The Fourier Transform. In *Digital Signal Processing*, pages 75–113. Elsevier.

Blight, G. E. (1997). The Rankine Lecture. *Géotechnique*, 47(4):713–767.

Blight, G. E. (2013). *Unsaturated Soil Mechanics in Geotechnical Practice*. CRC Press, 0 edition.

Carmona, A. M. and Poveda, G. (2014). Detection of long-term trends in monthly hydro-climatic series of Colombia through Empirical Mode Decomposition. *Climatic Change*, 123(2):301–313.

Carri, A., Savi, R., and Segalini, A. (2017). Role of geotechnical monitoring: State of the art and new perspectives. In *GEO-EXPO 2017, Sarajevo, October 26-27, 2017*.

Corona, R., Katul, G., and Montaldo, N. (2022). The root-zone soil moisture spectrum in a mediterranean ecosystem. *Journal of Hydrology*, 609:127757.

Denmead, O. T. and Shaw, R. H. (1962). Availability of soil water to plants as affected by soil moisture content and meteorological conditions1. *Agronomy Journal*, 54:385–390.

Dickinson, R. (1984). Modelling evapotranspiration for three-dimensional global climate models. In *Climate Processes and Climate Sensitivity*, volume 5, pages 58–72. American Geophysical Union, Geophysical Monograph 29.

Elia, G., Cotecchia, F., Pedone, G., Vaunat, J., Vardon, P. J., Pereira, C., Springman, S. M., Rouainia, M., Van Esch, J., Koda, E., Josifovski, J., Nocilla, A., Askarinejad, A., Stirling, R., Helm, P., Lollino, P., and Osinski, P. (2017). Numerical modelling of slope–vegetation–atmosphere interaction: an overview. *Quarterly Journal of Engineering Geology and Hydrogeology*, 50(3):249–270.

Feddes, R. A. (1982). Simulation of field water use and crop yield. In de Vries, F. W. T. P. and van Laar, H. H., editors, *Simulation of plant growth and crop production*, Simulation monographs, pages 194–209. Pudoc, Wageningen.

Fraccica, A., Romero, E., and Fourcaud, T. (2022). Tensile strength of a compacted vegetated soil: Laboratory results and reinforcement interpretation. *Geomechanics for Energy and the Environment*, 30:100303.

Gaci, S. (2016). A New Ensemble Empirical Mode Decomposition (EEMD) Denoising Method for Seismic Signals. *Energy Procedia*, 97:84–91.

Garces, H. and Sbarbaro, D. (2009). Outliers Detection in Environmental Monitoring Data. *IFAC Proceedings Volumes*, 42(23):330–335.

Gasc-Barbier, M., Merrien-Soukatchoff, V., and Virely, D. (2021). The role of natural thermal cycles on a limestone cliff mechanical behaviour. *Engineering Geology*, 293:106293.

Gascoin, S., Ducharne, A., Ribstein, P., Lejeune, Y., and Wagnon, P. (2009). Dependence of bare soil albedo on soil moisture on the moraine of the Zongo glacier (Bolivia): Implications for land surface modeling. *Journal of Geophysical Research: Atmospheres*, 114(D19):2009JD011709.

Gauthier, T. D. (2001). Detecting trends using spearman's rank correlation coefficient. *Environmental Forensic Investigations*. Received 23 August 2001, Revised manuscript accepted 1 October 2001.

Gens, A. (2010). Soil–environment interactions in geotechnical engineering. *Géotechnique*, 60(1):3–74.

Gens, A. and Olivella, S. (2001). THM phenomena in saturated and unsaturated porous media: Fundamentals and formulation. *Revue Française de Génie Civil*, 5(6):693–717.

Ghestem, M., Veylon, G., Bernard, A., Vanel, Q., and Stokes, A. (2014). Influence of plant root system morphology and architectural traits on soil shear resistance. *Plant and Soil*, 377(1-2):43–61.

Gong, L., Du, X., Lin, C., Zhu, K., Liu, C., and Liang, W. (2021). Automated High-Resolution Structure Analysis of Plant Root with a Morphological Image Filtering Algorithm. *Mathematical Problems in Engineering*, 2021:1–14.

Graps, A. (1995). An introduction to wavelets. *IEEE Computational Science and Engineering*, 2(2):50–61.

Grinsted, A., Moore, J. C., and Jevrejeva, S. (2004). Application of the cross wavelet transform and wavelet coherence to geophysical time series. *Nonlinear Processes in Geophysics*, 11(5/6):561–566.

Guachizaca, V. F. (2018). Análisis de las interacciones suelo-vegetación-atmósfera en un talud experimental. Master's thesis, Universitat Politècnica de Catalunya. Accepted: 2018-07-20T12:31:44Z.

Hemmati, S., Gatmiri, B., Cui, Y.-J., and Vincent, M. (2012). Thermo-hydro-mechanical modelling of soil settlements induced by soil-vegetation-atmosphere interactions. *Engineering Geology*, 139-140:1–16.

Henao Casas, J. D. and Monsalve, G. (2018). Geological inferences about the upper crustal configuration of the Medellin – Aburra Valley (Colombia) using strong motion seismic records. *Geodesy and Geodynamics*, 9(1):67–76.

Hou, L. H., Gao, W., Der Bom, F., Weng, Z. H., Doolette, C. L., Maksimenko, A., Hausermann, D., Zheng, Y., Tang, C., Lombi, E., and Kopittke, P. M. (2022). Use of X-ray tomography for examining root architecture in soils. *Geoderma*, 405:115405.

Jarvis, P. (1976). The interpretation of the variations in leaf water potential and stomatal conductance found in canopies in the field. *Philosophical Transactions of the Royal Society of London. B, Biological Sciences*, 273(927):593–610.

Laszuk, D. (2017). Python implementation of empirical mode decomposition algorithm. `https://github.com/laszukdawid/PyEMD`.

Le, T.-P. (2017). Use of the Morlet mother wavelet in the frequency-scale domain decomposition technique for the modal identification of ambient vibration responses. *Mechanical Systems and Signal Processing*, 95:488–505.

Lee, E. and Kim, S. (2019). Wavelet analysis of soil moisture measurements for hillslope hydrological processes. *Journal of Hydrology*, 575:82–93.

Leung, A., Garg, A., Coo, J., Ng, C., and Hau, B. (2015). Effects of the roots of cynodon dactylon and schefflera heptaphylla on water infiltration rate and soil hydraulic conductivity. *Hydrological Processes*, 29(15):3342–3354.

Li, Y., Wang, Y., Wang, Y., and Ma, C. (2017). Effects of root spatial distribution on the elastic-plastic properties of soil-root blocks. *Scientific Reports*, 7:800.

Liu, H., Shah, S., and Jiang, W. (2004). On-line outlier detection and data cleaning. *Computers & Chemical Engineering*, 28(9):1635–1647.

Liu, J., Kumar, S., and Palomar, D. P. (2019). Parameter Estimation of Heavy-Tailed AR Model With Missing Data Via Stochastic EM. *IEEE Transactions on Signal Processing*, 67(8):2159–2172.

Liu, Q., Hao, Y., Stebler, E., Tanaka, N., and Zou, C. B. (2017). Impact of Plant Functional Types on Coherence Between Precipitation and Soil Moisture: A Wavelet Analysis. *Geophysical Research Letters*, 44(24).

Liu, W., Lin, X., Luo, J., Yao, M., Gu, Y., Xie, M., Liu, J., and Ma, Q. (2021). Seedling Production from Seeds of a Wild Ecotype of Vetiver Grass (<i>Vetiveria zizanioides</i> L.) in Southern China. *American Journal of Plant Sciences*, 12(03):394–405.

Lynch, J. P. (1995). Root architecture and plant productivity. *Plant Physiology*, 109:7–13.

Masi, E. B., Segoni, S., and Tofani, V. (2021). Root reinforcement in slope stability models: A review. *Geosciences*, 11(5):212.

McPherson, R. A. (2007). A review of vegetation–atmosphere interactions and their influences on mesoscale phenomena. *Progress in Physical Geography*, 31(3):261–285.

Moene, A. F. and Dam, J. C. v. (2014). *Transport in the atmosphere-vegetation-soil continuum*. Cambridge University Press, New York, NY.

Monteith, J. (1965). Evaporation and the environment. In *The state and movement of water in living organisms. Proceedings of the 19th symposium soc exp biol Swansea*, pages 205–234. Cambridge University Press.

Ng, C., Liu, H., and Song, F. (2015). Analytical solutions for calculating pore water pressure in an infinite unsaturated slope with different root architectures. *Canadian Geotechnical Journal*, 52(12):2086–2097.

Ng, C. and Zhan, L. (2007). Comparative Study of Rainfall Infiltration into a Bare and a Grassed Unsaturated Expansive Soil Slope. *Soils and Foundations*, 47(2):207–217.

Ng, C. W., Zhang, Q., Ni, J., and Li, Z. (2020). A new three-dimensional theoretical model for analysing the stability of vegetated slopes with different root architectures and planting patterns. *Computers and Geotechnics*. Research Paper.

Ng, C. W. W., Leung, A. K., and Ni, J. (2019). *Plant–Soil Slope Interaction*. CRC Press, Boca Raton : Taylor & Francis, a CRC title, part of the Taylor & Francis imprint, a member of the Taylor & Francis Group, the academic division of T&F Informa, plc, [2019], 1 edition.

Noilhan, J. and Mahfouf, J. (1996). The isba land surface parameterization scheme. *Global Planet Change*, 13:145–159.

Noilhan, J. and Planton, S. (1989). A Simple Parameterization of Land Surface Processes for Meteorological Models. *Monthly Weather Review*, 117(3):536–549.

Nyambayo, V. and Potts, D. (2009). Numerical simulation of evapotranspiration using a root water uptake model. *Computers and Geotechnics*, 36(4):676–685.

Olivella, S., Carrera, J., Gens, A., and Alonso, E. (1994). Non-isothermal multiphase flow of brine and gas through saline media. *Transport in Porous Media*, 15:271–293.

Olivella, S., Vaunat, J., and Rodriguez, A. (2023). CODE_bright 2023 User's Guide.

Oorthuis, R., Vaunat, J., Hürlimann, M., Lloret, A., Moya, J., Puig-Polo, C., and Fraccica, A. (2020). Slope Orientation and Vegetation Effects on Soil Thermo-Hydraulic Behavior. An Experimental Study. *Sustainability*, 13(1):14.

Oorthuis Gómez, R. (2022). *Monitoring and analysis of soil-vegetation-atmosphere interactions at slope and catchment scale : Implications for mass-wasting in natural and man-made slopes*. Ph.D. Thesis, Universitat Politècnica de Catalunya. Accepted: 2022-11-03T13:31:15Z Publication Title: TDX (Tesis Doctorals en Xarxa).

Pastorello, G., Agarwal, D., Papale, D., Samak, T., Trotta, C., Ribeca, A., Poindexter, C., Faybishenko, B., Gunter, D., Hollowgrass, R., and Canfora, E. (2014). Observational Data Patterns for Time Series Data Quality Assessment. In *2014 IEEE 10th International Conference on e-Science*, pages 271–278, Sao Paulo, Brazil. IEEE.

Pearson, R. (2002). Outliers in process modeling and identification. *IEEE Transactions on Control Systems Technology*, 10(1):55–63.

Peters, A., Durner, W., and Iden, S. C. (2017). Modified feddes type stress reduction function for modeling root water uptake: Accounting for limited aeration and low water potential. *Agricultural Water Management*, 185:126–136.

Phan, T. N. and Likitlersuang, S. (2024). Root system architecture of two vetiver species for root reinforcement modelling. *Modeling Earth Systems and Environment*, 10(1):233–241.

Rao, A. R. and Hsu, E.-C. (2008). *Hilbert-Huang transform analysis of hydrological and environmental time series*. Number 60 in Water science and technology library. Springer, Dordrecht.

Reubens, B., Poesen, J., Danjon, F., Geudens, G., and Muys, B. (2007). The role of fine and coarse roots in shallow slope stability and soil erosion control with a focus on root system architecture: a review. *Trees*, 21(4):385–402.

Reynolds, C., Escobedo, F., Clerici, N., and Zea-Camaño, J. (2017). Does "Greening" of Neotropical Cities Considerably Mitigate Carbon Dioxide Emissions? The Case of Medellin, Colombia. *Sustainability*, 9(5):785.

Rogers, E. D. and Benfey, P. N. (2015). Regulation of plant root system architecture: implications for crop advancement. *Current Opinion in Biotechnology*, 32:93–98.

Ruiz, D. (2013). Thermo-mechanical analysis of the stability of a rock-cliff under climatic actions. Master's thesis, Universitat Politècnica de Catalunya, Barcelona.

Sachan, R., Gautam, M. K., Tiwari, A., and Kumar, M. (2023). Evapotranspiration in the soil-plant-atmosphere system (spas). In *Current Research and Review in Soil Science, Volume 3*, pages 69–89. Bright Sky Publications.

Samat, S. (2016). *Thermomechanical modelling of ground response under environmental actions.* Ph.D. Thesis, Universitat Politècnica de Catalunya. Accepted: 2017-01-19T11:35:43Z Publication Title: TDX (Tesis Doctorals en Xarxa).

Sanchez, J. M., French, A. N., Mira, M., Hunsaker, D. J., Thorp, K. R., Valor, E., and Caselles, V. (2011). Thermal Infrared Emissivity Dependence on Soil Moisture in Field Conditions. *IEEE Transactions on Geoscience and Remote Sensing*, 49(11):4652–4659.

Schulte, J. A., Najjar, R. G., and Lee, S. (2017). Salinity and streamflow variability in the Mid-Atlantic region of the United States and its relationship with large-scale atmospheric circulation patterns. *Journal of Hydrology*, 550:65–79.

Scott, R. L., Goodrich, D. C., Williams, D. G., and Moran, M. S. (2021). Seasonal and interannual variability of evapotranspiration partitioning in semiarid ecosystems: Field studies in riparian woodlands and grasslands. *Agricultural and Forest Meteorology*, 297:108251.

Sedighi, M., Hepburn, B. D. P., Thomas, H. R., and Vardon, P. J. (2018). Energy balance at the soil atmospheric interface. *Environmental Geotechnics*, 5(3):146–157.

Seethepalli, A., Dhakal, K., Griffiths, M., Guo, H., Freschet, G. T., and York, L. M. (2021). RhizoVision Explorer: open-source software for root image analysis and measurement standardization. *AoB PLANTS*, 13(6):plab056.

Sellers, P. J., Mintz, Y., Sud, Y. C., and Dalcher, A. (1986). A Simple Biosphere Model (SIB) for Use within General Circulation Models. *Journal of the Atmospheric Sciences*, 43(6):505–531.

Shamim, Z., Razzaq, H., Shahid, M. N., and Awan, M. T. (2021). Generation of New Landraces of Forage Species: Red Fescue and Clover. In *Wild Germplasm for Genetic Improvement in Crop Plants*, pages 259–268. Elsevier.

Song, Y. M., Wang, Z. F., Qi, L. L., and Huang, A. N. (2019). Soil Moisture Memory and Its Effect on the Surface Water and Heat Fluxes on Seasonal and Interannual Time Scales. *Journal of Geophysical Research: Atmospheres*, 124(20):10730–10741.

Sánchez, M. (2004). *Thermo-hydro-mechanical coupled analysis in low permeability media*. Ph.D. Thesis, Universitat Politècnica de Catalunya. Accepted: 2017-09-12T09:40:27Z Publication Title: TDX (Tesis Doctorals en Xarxa).

Tang, A. M., Hughes, P. N., Dijkstra, T. A., Askarinejad, A., Brenčič, M., Cui, Y. J., Diez, J. J., Firgi, T., Gajewska, B., Gentile, F., Grossi, G., Jommi, C.,

Kehagia, F., Koda, E., Ter Maat, H. W., Lenart, S., Lourenco, S., Oliveira, M., Osinski, P., Springman, S. M., Stirling, R., Toll, D. G., and Van Beek, V. (2018). Atmosphere–vegetation–soil interactions in a climate change context; impact of changing conditions on engineered transport infrastructure slopes in Europe. *Quarterly Journal of Engineering Geology and Hydrogeology*, 51(2):156–168.

Tarantino, A. and Roberts-Self, E. (2023). Transpiration in the water-limited regime: soil-plant-atmosphere interactions. *E3S Web of Conferences*, 382:13001.

Torrence, C. and Compo, G. P. (1998). A Practical Guide to Wavelet Analysis. *Bulletin of the American Meteorological Society*, 79(1):61–78.

Torrence, C. and Webster, P. J. (1999). Interdecadal changes in the enso–monsoon system. *Journal of Climate*, 12(8):2679–2690.

Tracy, S. R., Roberts, J. A., Black, C. R., McNeill, A., Davidson, R., and Mooney, S. J. (2010). The X-factor: visualizing undisturbed root architecture in soils using X-ray computed tomography. *Journal of Experimental Botany*, 61(2):311–313.

Vilà-Guerau De Arellano, J., Van Heerwaarden, C. C., Van Stratum, B. J. H., and Van Den Dries, K. (2015). *Atmospheric Boundary Layer: Integrating Air Chemistry and Land Interactions*. Cambridge University Press, 1 edition.

Virely, D., Gasc-Barbier, M., and Merrien-Soukatchoff, V. (2021). More than eleven years of temperature and displacements recorded on and in a limestone cliff: Dataset. *Data in Brief*, 39:107568.

Virtanen, P., Gommers, R., Oliphant, T. E., Haberland, M., Reddy, T., Cournapeau, D., Burovski, E., Peterson, P., Weckesser, W., Bright, J., and et al. (2020). SciPy 1.0: fundamental algorithms for scientific computing in Python. *Nature Methods*, 17(3):261–272.

Wang, X., Ma, C., Wang, Y., Wang, Y., Li, T., Dai, Z., and Li, M. (2020). Effect of root architecture on rainfall threshold for slope stability: variabilities in saturated hydraulic conductivity and strength of root-soil composite. *Landslides*, 17(8):1965–1977.

Wu, D., Di, C., Wang, T., Wang, L., and Chen, X. (2021). Characterization of the Coherence Between Soil Moisture and Precipitation at Regional Scales. *Journal of Geophysical Research: Atmospheres*, 126(8):e2020JD034340.

Wu, J., Jin, X., Mi, S., and Tang, J. (2020). An effective method to compute the box-counting dimension based on the mathematical definition and intervals. *Results in Engineering*, 8:100106. Under a Creative Commons license.

Wu, Z. and Huang, N. E. (2009). Ensemble empirical mode decomposition: a noise-assisted data analysis method. *Advances in Adaptive Data Analysis*, 1(1):1–41.

Xiang, Y., Wang, X., He, L., Wang, W., and Moran, W. (2016). Spatial-Temporal Analysis of Environmental Data of North Beijing District Using Hilbert-Huang Transform. *PLOS ONE*, 11(12):e0167662.

Yen, C. P. (1987). Tree root patterns and erosion control. In Jantawat, S., editor, *Proceedings of the International Workshop on Soil Erosion and Its Countermeasures*, pages 92–111, Bangkok. Soil and Water Conservation Society of Thailand.

Yin, W., Pan, Y., Yang, M., and Li, Z. (2024). The root reinforcement on the slope under the condition of colonization of various herbaceous plants. *Heliyon*, 10(17):e37108. Under a Creative Commons license, open access.

Appendix 1

Basic features of the formulation

The formulation incorporates the basic thermal, hydraulic, and mechanical phenomena. All the mathematical description below was taken from Sánchez (2004) and Gens and Olivella (2001).

Balance equations

Mass balance equations

The formulation employs a compositional mass balance, focusing on species rather than phases. By aggregating species equations, it derives total species conservation equations, eliminating phase transfer terms, which is particularly advantageous under equilibrium conditions. The macroscopic balance of a thermodynamic property, S, is expressed within a continuum framework as,

$$\frac{\partial}{\partial t}(\rho\pi) + \nabla \cdot (\mathbf{j}_\pi) - f^\pi = 0 \tag{1.1}$$

In this context, ρ represents the mass density of a given species that includes π, while $\mathbf{j}_\pi$ denotes the total flux relative to a fixed reference frame. The term f^π describes the volumetric rate of production or consumption for the species. The flux $\mathbf{j}_\pi$ is measured in a stationary frame of reference to accommodate the motion of the solid phase. This total flux consists of two components: an advective part, associated with the motion of the phase itself, and a non-advective part, which corresponds to the movement of the species within the phase.

$$\mathbf{j}_\pi = \rho\pi v_\pi + i_\pi \tag{1.2}$$

where v_π is the mass-weighted mean velocity and i_π is the non-advective flux.

Mineral mass balance equation

The mass conservation equation governing the mineral (solid phase) within the medium is expressed as follows,

$$\frac{\partial}{\partial t}\left(\theta_s(1-\phi)\right) + \nabla \cdot (j_s) = 0 \tag{1.3}$$

Here, θ_s represents the mass of the solid phase per unit volume of the solid, while j_s denotes the total flux of the solid relative to a fixed reference frame.

Water mass balance equation

Water is present within the system as both a constituent of the liquid phase and as a gaseous vapor component. The total volumetric water mass is expressed as,

$$\theta_l^w S_l \phi + \theta_g^w S_g \phi \tag{1.4}$$

where the terms represent liquid and vapor water components respectively. Note that:

$$S_l + S_g = 1 \tag{1.5}$$

This constitutes a constraint derived from fluid phase saturation definition. Water fluxes per phase are expressed as,

$$j_l^w = i_l^w + \theta_l^w q_l + \theta_l^w S_l \phi \dot{u} = j_l^w + \theta_l^w S_l \phi \dot{u} \tag{1.6}$$

$$j_g^w = i_g^w + \theta_g^w q_g + \theta_g^w S_g \phi \dot{u} = j_g^w + \theta_g^w S_g \phi \dot{u} \tag{1.7}$$

In this context, i_l^w and i_g^w represent the non-advective fluxes of water within the liquid and gas phases, respectively. The advective terms account for the movement of the phases themselves. The latter expression distinguishes between the relative motion of water species with respect to the solid phase and the absolute motion (j_w) relative to a fixed reference frame. Consequently, the total water mass balance can be formulated as,

$$\frac{\partial}{\partial t}\left(\theta_l^w S_l \phi + \theta_g^w S_g \phi\right) + \nabla \cdot \left(j_l^w + j_g^w\right) = f^w \tag{1.8}$$

where f^w is an external supply of water. It should be pointed out that, in this form, the dependence of the storage term on porosity variations does not appear explicitly.

Air mass balance equation

Dry air, treated as a single species, exists as a component of both gas phase (mixed with water vapor) and dissolved in liquid phase. Total air content in the porous medium is expressed as,

$$\theta_l^a S_l \phi + \theta_g^a S_g \phi \tag{1.9}$$

The mass fluxes of air in each fluid phase are

$$j_l^a = i_l^a + \theta_l^a q_l + \theta_l^a S_l \phi \dot{u} = j_l^a + \theta_l^a S_l \phi \dot{u} \tag{1.10}$$

$$j_g^a = i_g^a + \theta_g^a q_g + \theta_g^a S_g \phi \dot{u} = j_g^a + \theta_g^a S_g \phi \dot{u} \tag{1.11}$$

where i_l^a and i_g^a are the non-advective fluxes of air in the liquid and gas phases. The air mass balance equation is:

$$\frac{\partial}{\partial t}\left(\theta_l^a S_l \phi + \theta_g^a S_g \phi\right) + \nabla \cdot \left(j_l^a + j_g^a\right) = f^a \tag{1.12}$$

Energy balance equation

The energy balance in porous media is often simplified to an enthalpy balance, although an internal energy formulation remains applicable. When thermal equilibrium is assumed, the temperature is uniform across all phases, allowing a single total energy equation to be used. The total internal energy per unit volume of the porous medium is determined by summing the contributions from each phase as follows,

$$E_s \rho_s (1 - \phi) + E_l \rho_l S_l \phi + E_g \rho_g S_g \phi \tag{1.13}$$

Here, E_s, E_l, and E_g denote the specific internal energies of the solid, liquid, and gas phases, respectively, each defined as the internal energy per unit mass of the corresponding phase.

The main mechanisms driving energy transfer in a porous medium include conduction, advection, and phase changes. By utilizing specific internal energies and species mass fluxes, the energy fluxes associated with phase motion are expressed as,

$$j_{E_s} = E_s \rho_s (1 - \phi) \dot{u} \tag{1.14}$$

$$j_{E_l} = j_l^w E_l^w + j_l^a E_l^a + E_l \rho_l S_l \phi \dot{u} = j_{E_l} + E_l \rho_l S_l \phi \dot{u} \tag{1.15}$$

$$j_{E_g} = j_g^w E_g^w + j_g^a E_g^a + E_g \rho_g S_g \phi \dot{u} = j_{E_g} + E_g \rho_g S_g \phi \dot{u} \tag{1.16}$$

where j_{E_l} and j_{E_g} are advective energy fluxes with respect to the solid phase.

Using those definitions, the energy balance equation is expressed as:

$$\frac{\partial}{\partial t}\left(E_s \rho_s (1 - \phi) + E_l \rho_l S_l \phi + E_g \rho_g S_g \phi\right) + \nabla \cdot \left(i_c + j_{E_s} + j_{E_l} + j_{E_g}\right) = f^E \tag{1.17}$$

where i_c is the heat conduction flux and f^E is an internal/external energy supply. The internal production could include, for instance, energy dissipation due to medium deformation, but this is generally negligible.

Momentum balance equation

When inertial terms are neglected, the momentum balance for a porous medium simplifies to the equilibrium equation for macroscopic total stresses, expressed as,

$$\nabla \cdot \sigma + b = 0 \tag{1.18}$$

where σ represents the total stresses and b is the vector of body forces.

Constitutive Equations

Constitutive equations establish relationships between unknown variables and dependent parameters, with the latter categorized based on the complexity of their correlations. Fundamental constitutive laws are typically divided into three main categories: thermal, hydraulic, and mechanical. Although classified separately, these equations intrinsically couple multiple phenomena within their formulations. By integrating constitutive equations into the balance equations, the governing equations are expressed in terms of the unknowns.

Thermal Constitutive Equations

Heat conduction is governed by law of Fourier, as,

$$\mathbf{i_c} = -\lambda \nabla T \tag{1.19}$$

where λ is the thermal conductivity of the whole porous medium.

Hydraulic Constitutive Equations

In the case of two overlapping flow domains, advective fluxes of the fluid phase in each medium are computed using the generalized law of Darcy, which is expressed as,

$$q_{\alpha j} = -K_{\alpha j} \left(\nabla P_{\alpha j} - \rho_{\alpha j} \mathbf{g} \right), \quad \alpha = l, g; \quad j = 1, 2 \tag{1.20}$$

where $P_{\alpha j}$ is the pressure of the α phase in the j medium, and $K_{\alpha j}$ is the permeability tensor of the α phase in the j medium, evaluated as:

$$K_{\alpha j} = \frac{k_j}{\mu_{\alpha j}}, \quad \alpha = l, g; \quad j = 1, 2 \tag{1.21}$$

Here, k_j represents the intrinsic permeability tensor of a medium j, which is determined by its pore structure and is typically modeled as a function of the porosity of j. Various models are available to describe this dependence, providing flexibility to adapt to different scenarios. The term $\mu_{\alpha j}$ denotes the dynamic viscosity of phase α within the medium j, while $k_{\alpha j}$ refers to the relative permeability of phase α in j. Several models can be employed to define $k_{\alpha j}$, which is generally expressed as a function of the degree of saturation of the respective phase within each medium as,

$$k_{\alpha j} = f\left(S_{\alpha j}\right), \quad \alpha = l, g; \quad j = 1, 2 \tag{1.22}$$

The non-advective fluxes of species within the fluid phases of each porous medium are computed using law of Fick, which expresses them in terms of gradients of the mass fraction of species through a hydrodynamic dispersion tensor:

$$i^w_{\alpha j} = -D^w_{\alpha j} \nabla \omega^w_{\alpha j}, \quad i = w, a; \quad \alpha = l, g; \quad j = 1, 2 \tag{1.23}$$

where $D^w_{\alpha j}$ is the dispersion tensor of the medium, and $\omega^w_{\alpha j}$ is the mass fraction of i species in α phase.

Finally, the retention curve establishes the link between the saturation degree of the medium and the water potential.

Mechanical Constitutive Equation

A general expression for this law is presented here. A THM constitutive equation, explicitly showing the contributions of strains, temperature, and fluid pressures, can be expressed as:

$$\dot{\sigma_j} = D_j \dot{\epsilon_j} + f_j \dot{s} + t_j T_j, \quad j = 1, 2 \tag{1.24}$$

Here, σ_j represents the constitutive stress (net or effective stress), ϵ_j is the strain vector, s_j is a variable associated with fluid pressures, D_j is the constitutive stiffness matrix, f_j is the generic constitutive vector relating changes in fluid pressures and stresses, and t_j is the constitutive vector linking stresses to temperature.

While the total stress is typically the same for media 1 and 2, the constitutive stress may vary due to differences in fluid pressures. As a result, the two equations governing the two media are reduced to a single equation when the strains are summed, and this equation is then solved for the total stress.

Phase Physical Properties

The properties of the fluid phases appear in both the balance equations and the constitutive law. In general, they depend on the composition of the phases and on the state variables (temperature and fluid pressures).

Equilibrium Restrictions

It is assumed that phase changes occur rapidly relative to the typical timescales of the problem. Consequently, phase changes are treated as being in local equilibrium, resulting in a set of equilibrium constraints that must be satisfied at all times. The compositional approach offers the advantage of excluding explicit phase change terms, thereby reducing the number of equations. The equilibrium constraints apply to the concentration of water vapor in the gas phase, which is calculated using the psychometric law, and to the concentration of dissolved air in the liquid phase, which is determined through the law of Henry.

Mass Transfer Between Media

In the following equations, the term $\Gamma^i (i = w, a)$ controls mass transfer between media. A simple model for this term is expressed as:

$$\Gamma^i = \gamma \left(\Psi_1^i - \Psi_2^i \right) \tag{1.25}$$

where γ is the leakage parameter, and $\Psi_j^i (j = 1, 2)$ represents the thermodynamic force involved in the mass transfer. For water mass transfer, the total water potential (or chemical water potential in more general cases) is the variable involved. In some cases, fluid pressures are adopted as the primary variables controlling mass transfer.

For liquid transfer between media, the process typically occurs under a smooth change of pressure, allowing the assumption of quasi-steady conditions.

Appendix 2

Soil characterization

The Figure 43 shows the characterization of Hispania Soil. This is the conditions where *C. zizanioides* grow for almost 1 month.

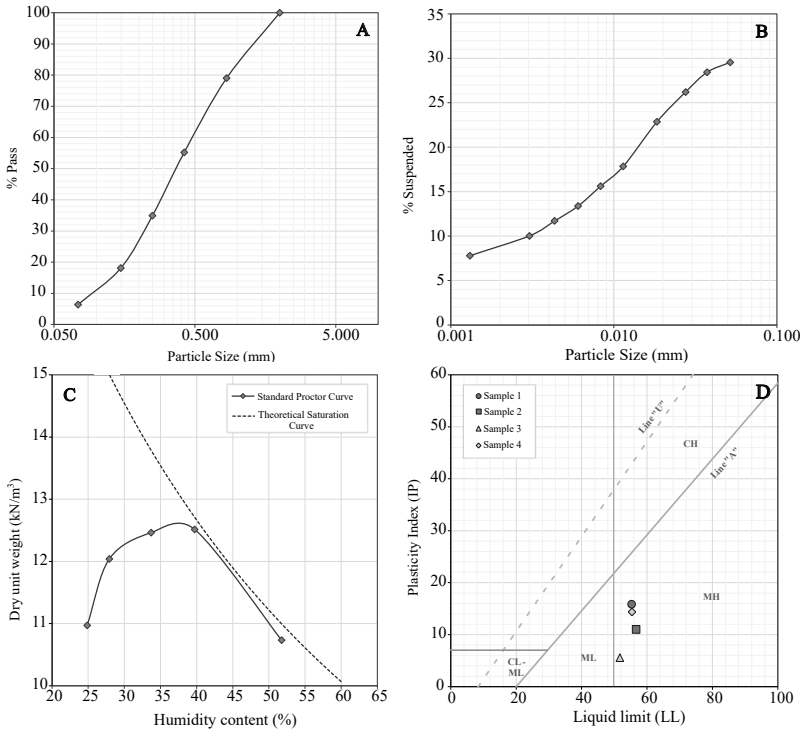

Figure 43: Soil characterization of Hispania. A is sieving characterization, B is hydrometer for fine particles, C is a standard proctor test and D is Casagrande plasticity chart.

Appendix 3

Supplementary Time Series

For all other locations of Aburrá Valley, the time series are shown below in Figures 44, 45, 46 and 47.

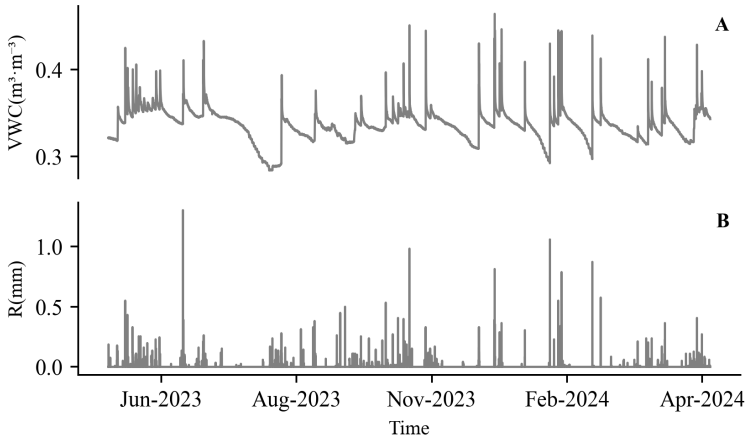

Figure 44: Station 532 Time Series, A is θ and B is R.

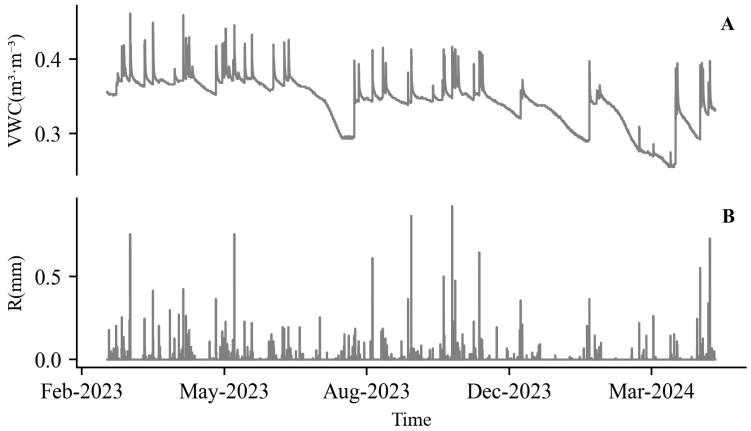

Figure 45: Station 541 Time Series, A is θ and B is R.

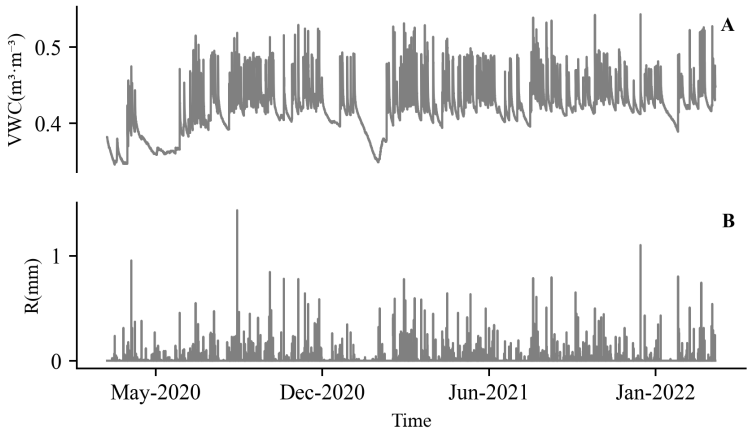

Figure 46: Station 396 Time Series, A is θ and B is R.

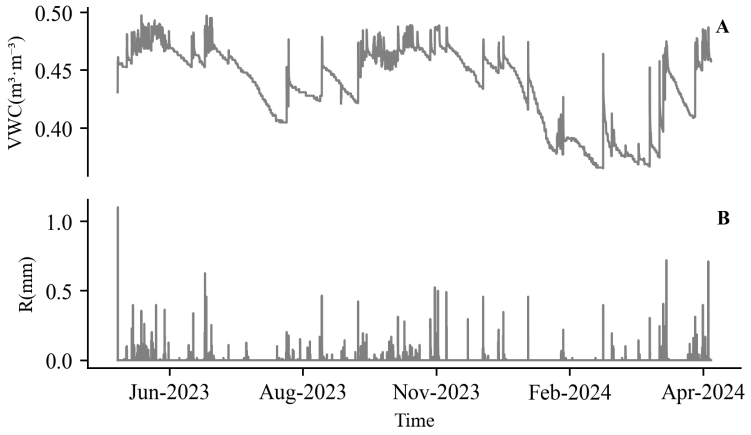

Figure 47: Station 613 Time Series, A is θ and B is R.

Global Wavelet Spectrum

Le Fauga

Figure 48 shows the global wavelet spectrum for other variables in Le Fauga study site.

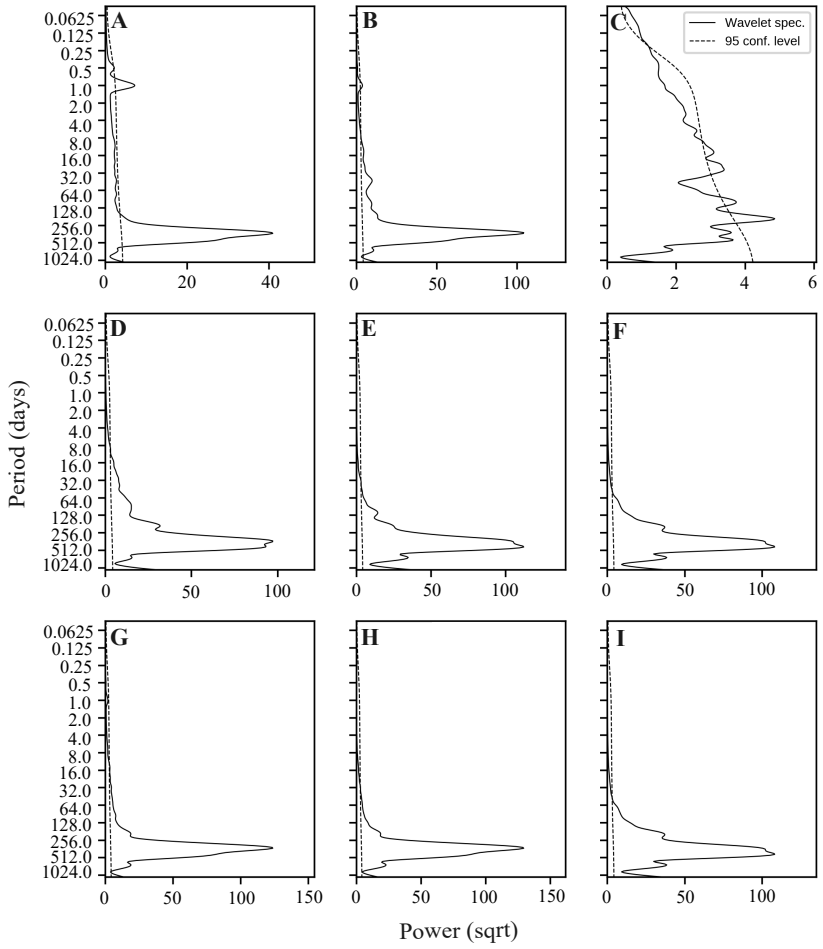

Figure 48: Global Walevet Spectrum for Le Fauga Time Series. A is R_n, B is T_a, C is P, D is $\theta_{surface}$, E is θ_{50cm}, F is θ_{90cm}, G is $Ts_{surface}$, H is Ts_{50cm}, and I is Ts_{90cm}.

La Roque-Gageac

Figure 48 shows the global wavelet spectrum for other variables in La Roque study site.

Aburrá Valley

Figure 48 shows the global wavelet spectrum for other variables in Aburrá Valley study site.

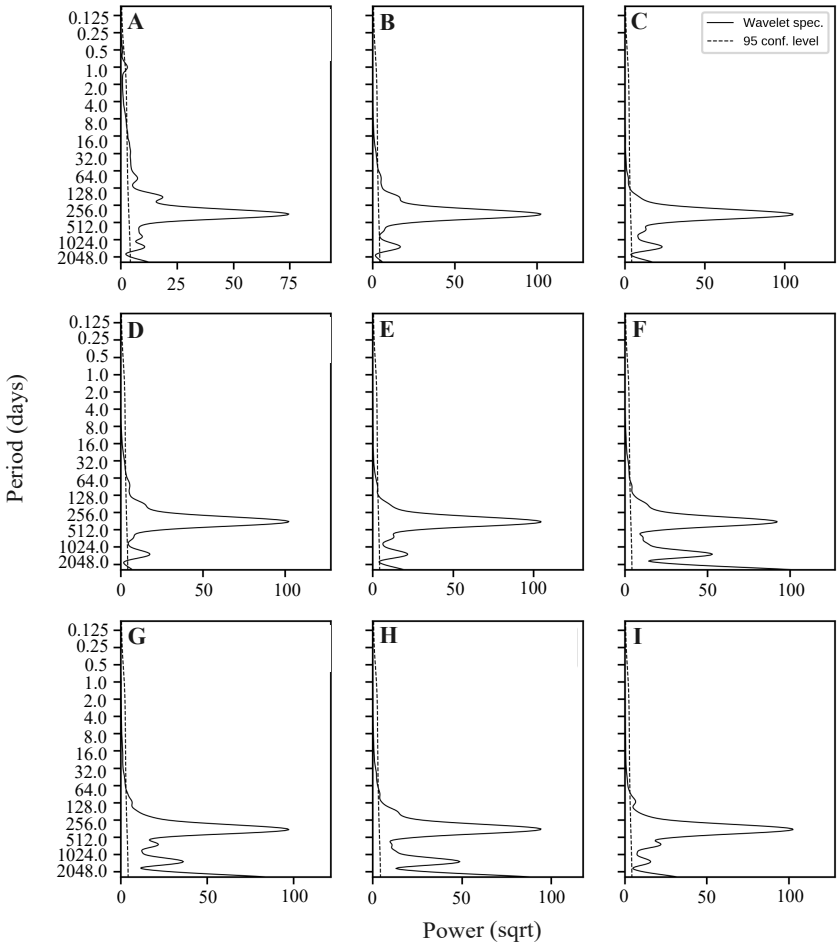

Figure 49: Global Walevet Spectrum for La Roque-Gageac Time Series. A is T_a, B is $D1T_{2m}$, C is $D1T_{6m}$, D is $D2T_{2m}$, E is $D2T_{6m}$, F is $D1\delta_{2m}$, G is $D1\delta_{6m}$, H is $D2\delta_{2m}$, and I is $D2\delta_{6m}$.

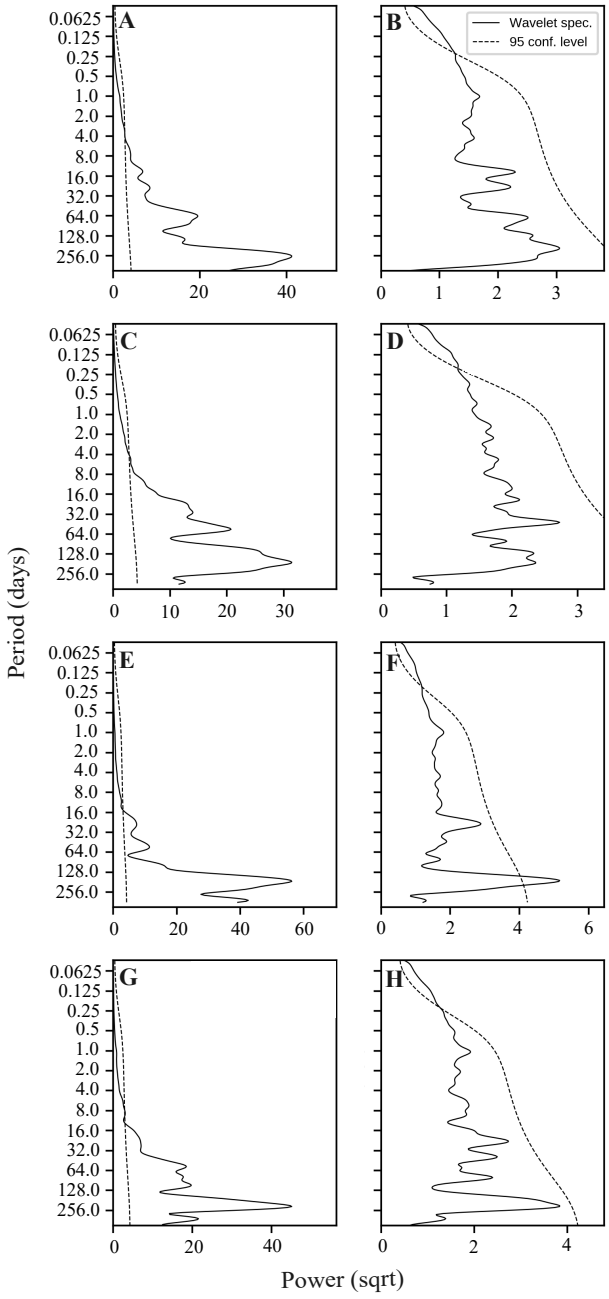

Figure 50: Global Walevet Spectrum for Aburrá Time Series. A is θ_{50cm} at station 613, B is R at station 613, C is θ_{50cm} at station 541, D is R at station 541, E is θ_{50cm} at station 396, F is R at station 396, G is θ_{50cm} at station 532 and H is R at station 532.

Hilbert-Huang Spectrum

Le Fauga

Figure 51 shows the Hilbert-Huang for other variables in Le Fauga study site.

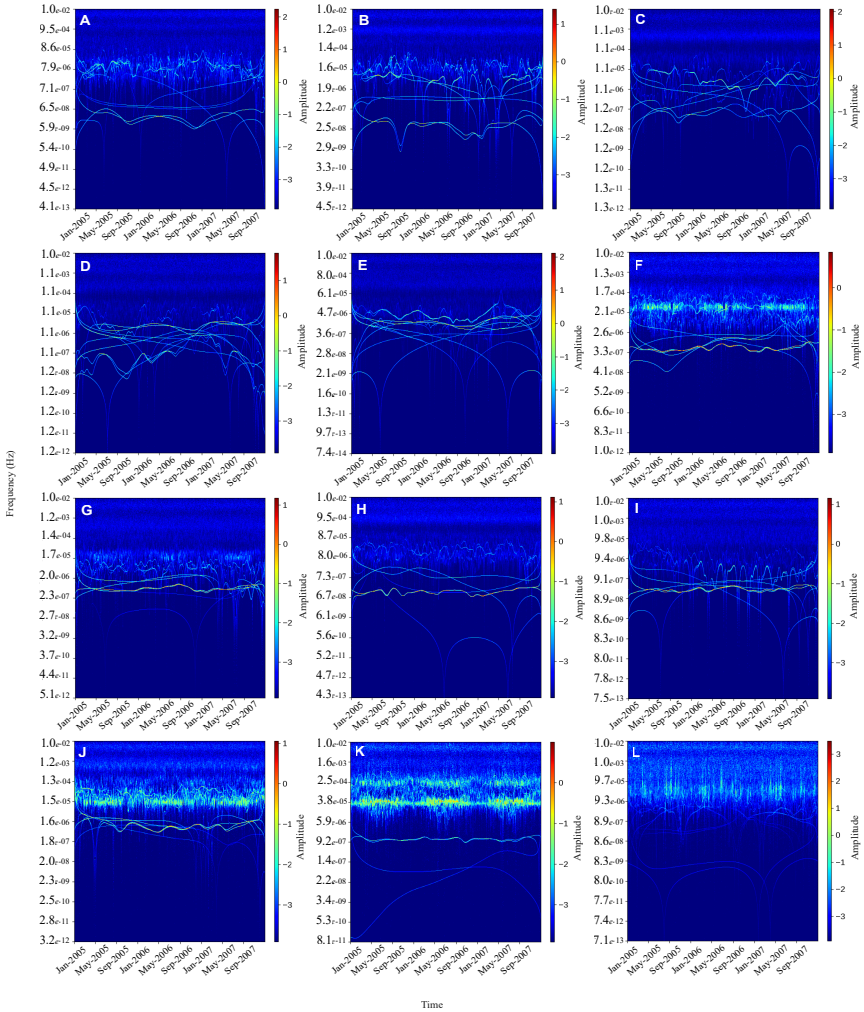

Figure 51: Hilbert-Huang Spectrum for Le Fauga Time Series. A is θ_{surface}, B is $\theta_{20\text{cm}}$, C is $\theta_{50\text{cm}}$, D is $\theta_{70\text{cm}}$, E is $\theta_{90\text{cm}}$, F is $T_{s,\text{surface}}$, G is $T_{s,20\text{cm}}$, H is $T_{s,50\text{cm}}$, I is $T_{s,90\text{cm}}$, J is T_a, K is R_n, and L is P.

La Roque-Gageac

Figure 53 and Figure **??** shows the Hilbert-Huang for other variables in La Roque study site.

Aburrá Valley

Figure 54 shows the Hilbert-Huang for other variables in Aburrá Valley study site.

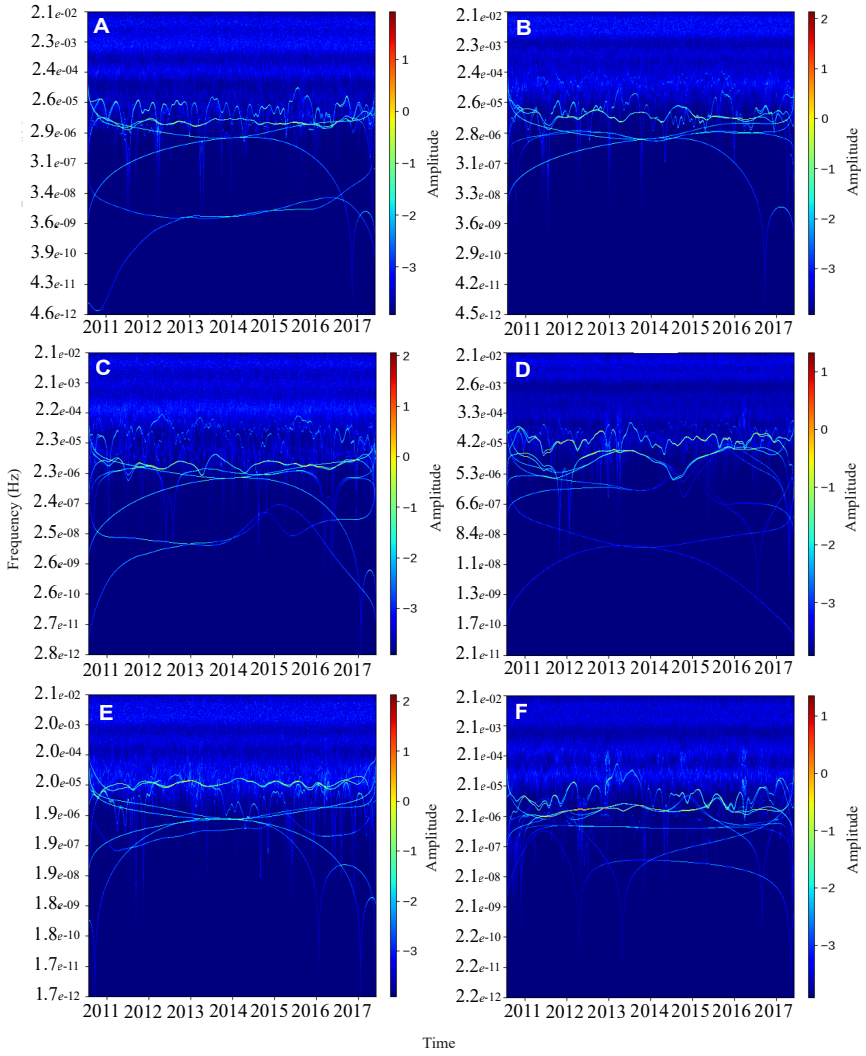

Figure 52: Hilbert-Huang Spectrum for La Roque-Gageac Time Series. A is $D1\delta_{6m}$, B is $D2\delta_{6m}$, C is $D1\delta_{4m}$, D is $D2\delta_{4m}$, E is $D1\delta_{2m}$ and F $D2\delta_{2m}$.

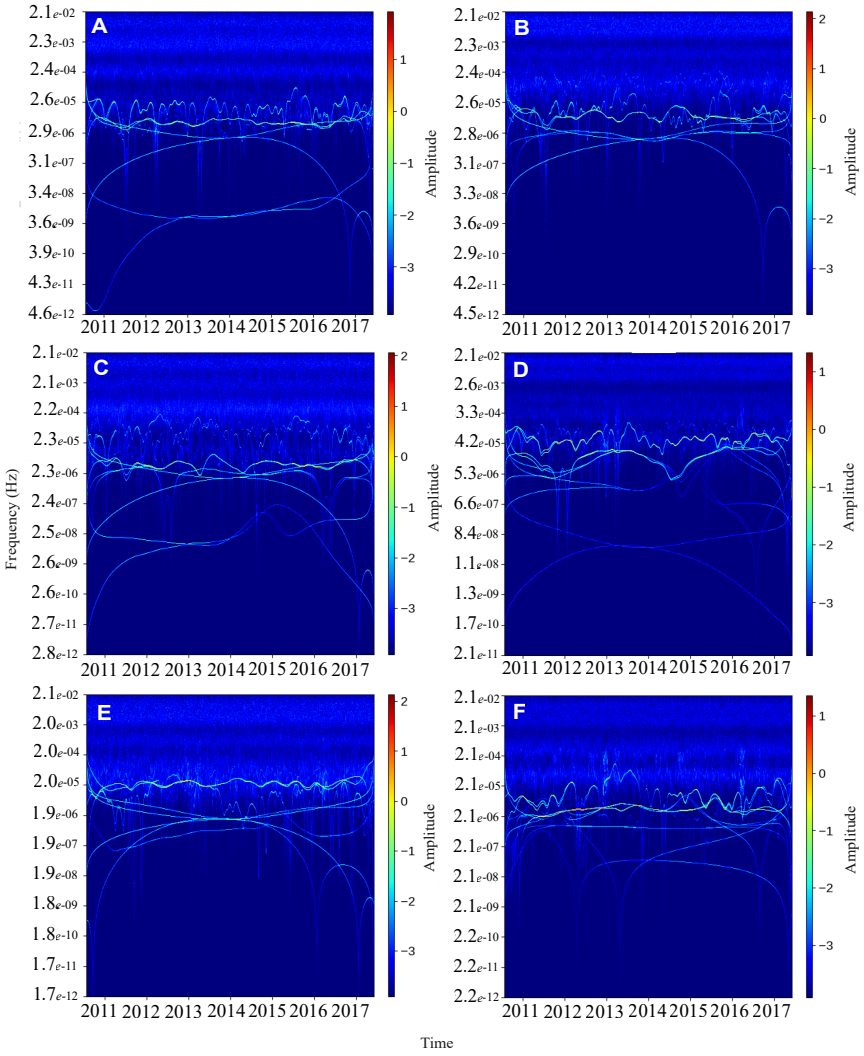

Figure 53: Hilbert-Huang Spectrum for La Roque-Gageac Time Series. A is T_a, B is $D1T_{2m}$, C is $D1T_{6m}$, D is $D2T_{2m}$, E is $D2T_{6m}$ and F.

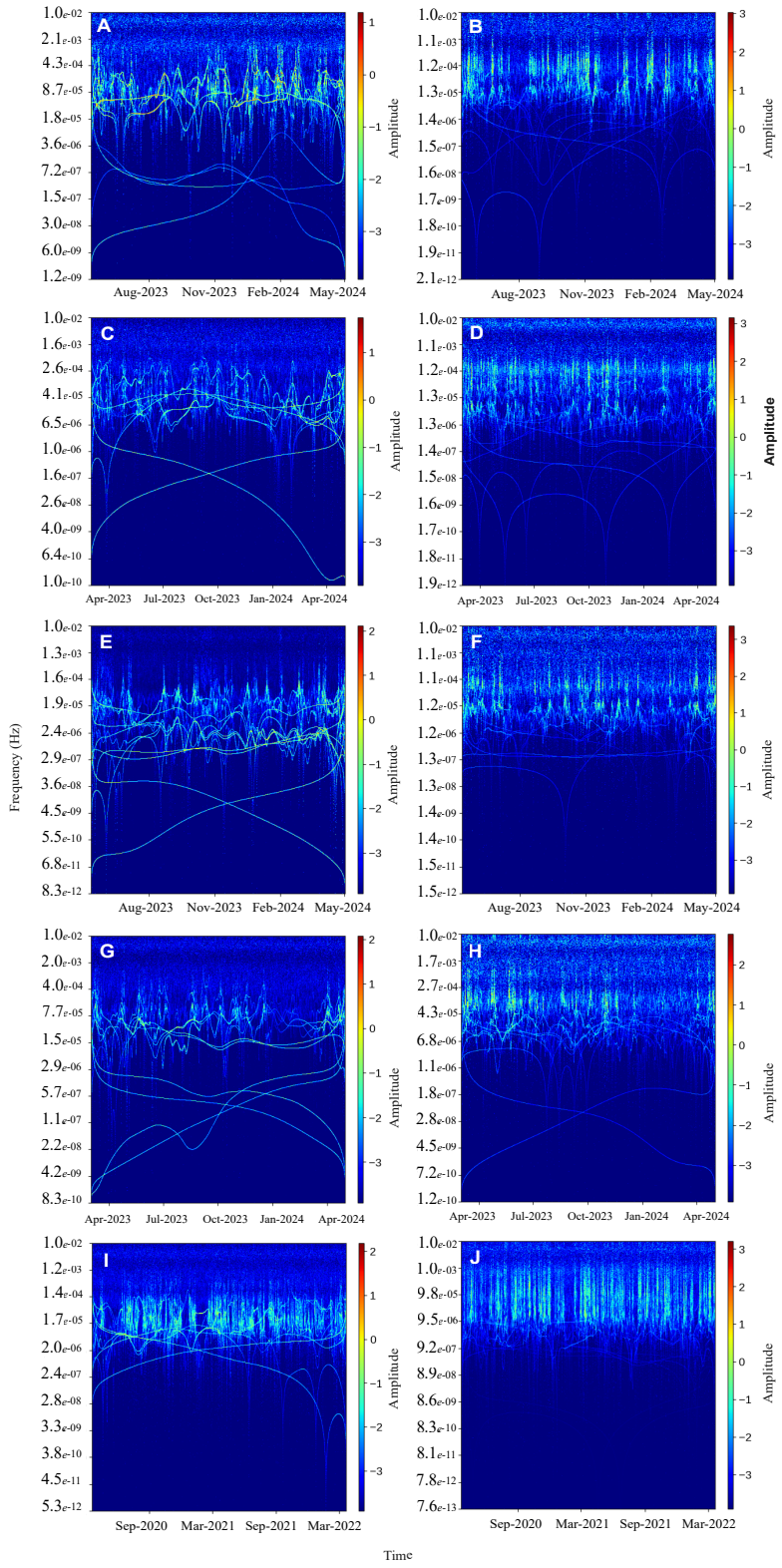

Figure 54: Hilbert-Huang Spectrum for Aburrá Valley Time Series. A is θ_{50cm} at station 608, B is R at station 608, C is θ_{50cm} at station 532, D is R at station 532, E is θ_{50cm} at station 613, F is R at station 613, G is θ_{50cm} at station 541, H is R at station 541, I is θ_{50cm} at station 396 and J is R at station 396.